

A Faceted Chamber for Magnetic Field Microwave Breast Imaging

by

Kyle Nemez

A Thesis submitted to the Faculty of Graduate Studies of
The University of Manitoba
in partial fulfillment of the requirements for the degree of

Master of Science

Department of Electrical and Computer Engineering
University of Manitoba
Winnipeg, Manitoba, Canada

Copyright © 2017 Kyle Nemez

Abstract

This thesis details the development and testing of a novel microwave breast imaging system based on a faceted metallic chamber using magnetic field data in an air background. Microwave imaging (MWI) is an imaging modality that uses electromagnetic fields to determine the electrical properties of an object of interest. Due to its use of non-ionizing microwave radiation and relatively low cost, MWI has emerged as a promising modality for a variety of biomedical applications, including breast cancer detection. Most experimental MWI systems currently collect electric scattered field data and employ a matching fluid to couple the microwave energy into the tissue. Recent developments in MWI research in the imaging group at the University of Manitoba have shown that magnetic field data can provide better reconstructions (particularly in metallic chambers), and with the incorporation of prior information, synthetic breast tissue targets can be accurately reconstructed in an air background without a coupling medium. This thesis details the design and implementation of a novel MWI system that experimentally verifies these findings.

A novel metallic faceted chamber geometry is conceived and simulated, and benefits over a conventional cylindrical imaging chamber are shown. Using synthetically generated data, the use of magnetic scattered-field data collected on the inner surface of the chamber is shown to provide better reconstruction results compared to electric field data for two different breast tissue phantoms. These synthetic results motivate the development of an experimental faceted chamber. Towards this end, shielded half-loop probes are selected for use in the new system. Several prototypes are designed, built, and tested, eventually leading to a refined design suitable for use in the faceted chamber. These probes are primarily sensitive to magnetic fields and reject electric fields, and are also reconfigurable by way of a controllable shorting diode.

An experimental faceted chamber is also constructed, and used with the half-loop probes to image both simple homogeneous targets as well as a simple breast phantom. Several possible measurement techniques and calibration methods for the new system are analyzed

and compared. The selected methods result in experimental reconstructions that compare very favourably to their synthetic equivalents. In particular, tumour detection in the simple breast phantom immersed in an air background is verified, validating the performance of the novel system.

Contributions

This work describes the development and testing of a novel microwave breast imaging system based on a faceted metallic chamber using magnetic field data. All the reconstructed images herein are generated using an FEM-CSI algorithm developed in the Electromagnetic Imaging Laboratory at the University of Manitoba, which is not the author's work. This algorithm was used in its current state and not modified. The specific contributions of this work include:

- A novel faceted chamber geometry for breast imaging is designed, and synthetically validated. It offers notable improvements over a typical cylindrical electric field based system.
- A magnetic field probe design for use in a breast imaging system. This probe has good magnetic field sensitivity and electric field rejection. It is also implemented on a printed circuit board, making it mass producible and physically robust.
- The novel faceted chamber design is constructed and tested with a variety of objects of interest, including a simple breast phantom. The results show that tumours can be detected in the breast phantom immersed in an air background, which to the author's knowledge, is a novel contribution.

Refereed Journal Papers

1. **Kyle Nemez**, Anastasia Baran, Mohammad Asefi, and Joe LoVetri. "Modeling error and calibration techniques for a faceted metallic chamber for magnetic field microwave imaging," to be submitted to *IEEE Transactions on Microwave Theory and Techniques* in January 2017 for review.

Refereed Conference Papers

1. Joe LoVetri, Mohammad Asefi, Anastasia Baran, and **Kyle Nemez**. “Effects of data collection schemes and systems on the imaging performance of electromagnetic inverse problems,” in *2016 Progress in Electromagnetic Research Symposium (PIERS)*, August 2016, pp. 937.
2. **Kyle Nemez**, Mohammad Asefi, Anastasia Baran, and Joe LoVetri. “A faceted magnetic field probe resonant chamber for 3D breast MWI: A synthetic study,” in *2016 17th International Symposium on Antenna Technology and Applied Electromagnetics (ANTEM)*, July 2016, pp. 1-3.
3. Majid OstadRahimi, Anastasia Baran, Mohammad Asefi, Cameron Kaye, **Kyle Nemez**, Joe LoVetri, and Stephen Pistorius. “On the development of a clinical full-vectorial 3d microwave breast imaging system,” in *Radio Science Meeting (Joint with AP-S Symposium), 2015 USNC-URSI*, July 2015, pp. 300.
4. Majid OstadRahimi, **Kyle Nemez**, Amer Zakaria, Joe LoVetri, Lotfollah Shafai, and Stephen Pistorius. “A novel microwave tomography system for breast imaging based on the modulated scattering technique,” in *Radio Science Meeting (Joint with AP-S Symposium), 2014 USNC-URSI*, July 2014, pp. 54.

Acknowledgements

I would first of all like to thank my academic advisor Dr. Joe LoVetri for his continued guidance, encouragement, and endless desire to further microwave imaging research. His passion for the subject is infectious, and desire to pursue the details has greatly improved this work.

I am also deeply grateful for the support and involvement of all the members of the Electromagnetic Imaging Laboratory. This work is one step towards improved microwave imaging that would not have been possible without the many years of progress made in the EIL, particularly by Dr. Mohammad Asefi and Dr. Anastasia Baran. I would also like to extend thanks to Anji Li and Rachel Peters for their work testing the MWI system. Thank you to everyone who has made the lab an enjoyable and collaborative place to work.

Thank you to Cory Smit in the Electrical and Computer Engineering machining shop at the University of Manitoba for his many hours of work fabricating components for the system developed herein.

I also thankful to my parents for always encouraging and supporting my pursuit of education, and my wife Lauren for her endless support over the many long hours that this research required.

Thank you also to my M.Sc. committee, Dr. Vladimir Okhmatovski and Dr. Jitendra Paliwal for evaluating and refining this work.

Lastly, I would like to thank the Natural Sciences and Engineering Research Council of Canada for their financial support.

To my parents and Lauren

Table of Contents

Abstract	i
Contributions	iii
Acknowledgements	v
List of Figures	ix
List of Tables	xiii
Symbols and Acronyms	xiv
1 Introduction	1
1.1 Microwave Imaging and Contrast Source Inversion	2
1.1.1 Mathematical Formulation of the Imaging Problem	3
1.1.2 Finite Element Method Contrast Source Inversion	6
1.1.3 Prior Information	9
1.1.4 MWI Systems	10
1.2 Motivation	11
1.3 Outline	12
1.3.1 Limitations to the Scope	13
2 Synthetic Development of a Faceted Chamber	14
2.1 A Faceted Hemi-Ellipsoid	16
2.1.1 Modeling Flat Geometry	19
2.1.2 Diversity of Data	20
2.2 E -Field and H -Field Inversion in a Faceted Chamber	25
2.2.1 A Simple Two-Tumour Breast Phantom	26
2.2.2 E -Field and H -Field Measurements	28
2.2.3 Inversion Results	29
2.2.4 A 5 Tissue Region Phantom	35

3	Probe Development	40
3.1	Probe Type Selection	42
3.2	Design of Four Prototype Printed Circuit <i>H</i> -Field Probes	45
3.2.1	Design Geometry Considerations	45
3.2.2	Microwave Transmission Line Parameters & Simulation	46
3.2.3	Testing of Prototypes in GTEM Cell	48
3.3	Refinement of a Grounded CPW <i>H</i> -Field Probe	51
4	Modeling Error and Calibration	56
4.1	Chamber Fabrication and Initial Testing	57
4.1.1	System Description	57
4.1.2	Co-Resident Probe Introduction	59
4.2	Modeling Error Analysis of Measured Data	64
4.2.1	Incident Field Modeling Error	66
4.2.2	Data Calibration Techniques	68
4.2.3	Targets Used for Calibration Assessment	70
4.2.4	Calibrated Scattered Field Modeling Error	70
4.3	Inversion of Simple Cylindrical Targets	74
5	Experimental Imaging of a Simple Breast Phantom	80
5.1	Simple Breast Phantom and Calibration Objects	80
5.2	Data Collection & Inversions	81
5.2.1	Discarding Data	83
5.2.2	Blind Inversions	84
5.2.3	Experimental Incorporation of Prior	85
5.2.4	Inversions Using Prior Information	87
5.2.5	Inversions Using Multiple Frequencies	90
6	Conclusions and Future Work	98
6.1	Future Work	99
	Appendix A Further Synthetic Analysis	101
A.1	Inversion Results for Two tumour Phantom with Imperfect Prior	101
A.2	Inversion Results for Two tumour Phantom with Dual Polarized H-Field Data	107
	References	110

List of Figures

1.1	Three dimensional model of the MWI problem. Image used with permission from Dr. Amer Zakaria.	2
1.2	Sample 3D mesh created with Gmsh.	7
1.3	MWI system architecture.	11
2.1	Facet centers, (a) top view and (b) side view.	17
2.2	Cross section of faceted chamber finite element mesh.	17
2.3	Transceiver positions, (a) top view and (b) side view.	18
2.4	Transceiver positions, (a) faceted chamber and (b) cylindrical equivalent.	19
2.5	Comparison of incident field error as a function of mesh discretization.	20
2.6	Cylindrical targets positioned in the (a) faceted chamber and (b) cylindrical equivalent.	21
2.7	Reconstructions at 1 GHz in (a) faceted and (b) cylindrical chambers.	22
2.8	Reconstructions at 1.5 GHz in (a) faceted and (b) cylindrical chambers.	23
2.9	Reconstructions at 2 GHz in (a) faceted and (b) cylindrical chambers.	23
2.10	Combined and normalized error metric for the faceted and cylindrical chambers, $\tau = 15\%$	26
2.11	Cross-section of 3D two-tumour breast phantom. $Re(\epsilon_r)$ is on the left, $-Im(\epsilon_r)$ on the right.	27
2.12	Two chamber top scenarios for the phantom (a) PEC and (b) plexiglass.	28
2.13	Electric and magnetic field polarizations.	29
2.14	Results at 0.9 GHz for a PEC chamber top.	30
2.15	Results at 0.9 GHz for a plexiglass chamber top.	31
2.16	Results at 1.3 GHz for a PEC chamber top.	31
2.17	Results at 1.3 GHz for a plexiglass chamber top.	32

2.18	Masks for the reconstruction using H_z with the plexiglass top at 1.05 GHz (a) ref_mask and (b) rec_mask	33
2.19	Metrics for $Re(\epsilon_r)$, PEC chamber top.	34
2.20	Metrics for $Im(\epsilon_r)$, PEC chamber top.	34
2.21	Metrics for $Re(\epsilon_r)$, plexiglass chamber top.	34
2.22	Metrics for $Im(\epsilon_r)$, plexiglass chamber top.	35
2.23	Five tissue region phantom.	36
2.24	Prior information for five tissue region phantom.	36
2.25	Results at 1.3 GHz for E_n	37
2.26	Results at 1.3 GHz for H_ϕ	38
2.27	Results at 1.3 GHz for H_z	39
3.1	Simple loop antenna in the presence of a magnetic field.	42
3.2	Two antennas, (a) a full loop radiating in free space and (b) a half loop radiating above the PEC plane. The blue dot indicates magnetic field coming out of the page.	43
3.3	Shielded half-loop with a top gap.	44
3.4	Prototype shielded half-loop with a top gap constructed from semi-rigid coax- ial cable.	45
3.5	Microwave transmission line topologies.	47
3.6	Half-loop transmission lines in HFSS.	47
3.7	Performance of half-loop transmission lines in HFSS.	48
3.8	Prototype probes.	50
3.9	GTEM cell.	51
3.10	Probe performance in GTEM cell. Measurements were taken in both orien- tations and with OC and SC load conditions.	52
3.11	Diode biasing circuit.	53
3.12	Final probe design with vias and diode circuitry.	53
3.13	Probe performance in GTEM cell.	54
3.14	Two adjacent probes under test.	55
3.15	Impact on S_{21} between GTEM apex and probe of adjacent probe.	55
4.1	Fabricated faceted chamber.	58
4.2	Fabricated faceted chamber with probes.	58
4.3	EIL MWI system block diagram.	59
4.4	Probe locations and corresponding numbers for co-residence testing.	60

4.5	Comparison of measured S_{21} with 2 probes and with all probes in the chamber for 4 different probe pairs.	62
4.6	Variable capacitor attached to second port of a probe.	65
4.7	S_{11} for antenna under different loading conditions.	65
4.8	Comparison of synthetic incident field and raw measured data for a single transmitter at (a) 0.8 GHz and (b) 1.2 GHz. Measurements taken under different loading conditions and with direct and delta methods. All data normalized but not calibrated.	67
4.9	Magnitude and phase for manually calibrated probe pairs compared to synthetic equivalent. Data shown is collected at 0.9 GHz using the direct measurement technique and an OC load condition.	68
4.10	Targets suspended in chamber, (a) oil filled cylinder #2, (b) metal sphere.	71
4.11	Cutaway view of numerical model for simple oil filled cylinder.	71
4.12	RMSE for all calibration types and measurement scenarios.	73
4.13	\mathcal{L}_2 norm of error between experimental inversions for all calibration types and measurement scenarios and the numerical reference.	75
4.14	Real inversion results at 1.0GHz. The left column is from the numerical data and the right column is from the OC loaded, c_2 scattered field calibrated experimental data. The black circle and rectangle indicate the true position of the OI.	76
4.15	Imaginary inversion results at 1.0GHz. The left column is from the numerical data and the right column is from the OC loaded, c_2 scattered field calibrated experimental data. The black circle and rectangle indicate the true position of the OI.	77
4.16	Real inversion results at 1.4GHz. The left column is from the numerical data and the right column is from the OC loaded, c_2 scattered field calibrated experimental data. The black circle and rectangle indicate the true position of the OI.	78
4.17	Imaginary inversion results at 1.4GHz. The left column is from the numerical data and the right column is from the OC loaded, c_2 scattered field calibrated experimental data. The black circle and rectangle indicate the true position of the OI.	79
5.1	Simple breast targets and calibration object.	82

5.2	Electrical properties of canola oil and 10:90 water/glycerin tumour, (a) real part and (b) imaginary part.	82
5.3	Simple breast targets in chamber.	83
5.4	Blind inversion results for simple breast phantom at several frequencies. The 2 left columns show $Re(\varepsilon_r)$ and the right columns shows the algorithm's error convergence.	86
5.5	Prior information, (a) $Re(\varepsilon_r)$ and (b) $-Im(\varepsilon_r)$	87
5.6	Inversion results for simple breast phantom at 0.95 GHz. The 2 left columns show $Re(\varepsilon_r)$ and the 2 right columns show $-Im(\varepsilon_r)$	91
5.7	Inversion results for simple breast phantom at 1.15 GHz. The 2 left columns show $Re(\varepsilon_r)$ and the 2 right columns show $-Im(\varepsilon_r)$	92
5.8	Inversion results for simple breast phantom at 1.30 GHz. The 2 left columns show $Re(\varepsilon_r)$ and the 2 right columns show $-Im(\varepsilon_r)$	93
5.9	Inversion results for simple breast phantom at 1.45 GHz. The 2 left columns show $Re(\varepsilon_r)$ and the 2 right columns show $-Im(\varepsilon_r)$	94
5.10	Inversion results for simple breast phantom at 1.50 GHz. The 2 left columns show $Re(\varepsilon_r)$ and the 2 right columns show $-Im(\varepsilon_r)$	95
5.11	Inversion results for breast phantom with tumour in position two at 1.45 GHz. The 2 left columns show $Re(\varepsilon_r)$ and the 2 right columns show $-Im(\varepsilon_r)$	96
5.12	Simultaneous frequency inversion results for simple breast phantom at 1 GHz and 1.4 GHz. (a) and (b) show $Re(\varepsilon_r)$ and (c) and (d) show $-Im(\varepsilon_r)$	97
5.13	Simultaneous frequency inversion results for simple breast phantom at 1.3 GHz and 1.4 GHz. (a) and (b) show $Re(\varepsilon_r)$ and (c) and (d) show $-Im(\varepsilon_r)$	97
A.1	Reconstructed ε_r at 0.9 GHz for a PEC chamber top.	102
A.2	Reconstructed ε_r at 1.2 GHz for a PEC chamber top.	103
A.3	Reconstructed ε_r at 1.5 GHz for a PEC chamber top.	103
A.4	Reconstructed χ at 0.9 GHz for a PEC chamber top.	104
A.5	Reconstructed χ at 1.2 GHz for a PEC chamber top.	105
A.6	Reconstructed χ at 1.5 GHz for a PEC chamber top.	105
A.7	Metrics for $Re(\varepsilon_r)$, PEC chamber top.	106
A.8	Metrics for $Im(\varepsilon_r)$, PEC chamber top.	106
A.9	Reconstructed ε_r for mixed H_ϕ and H_z and a PEC chamber top.	108
A.10	Metrics for $Re(\varepsilon_r)$, PEC chamber top.	109
A.11	Metrics for $Im(\varepsilon_r)$, PEC chamber top.	109

List of Tables

2.1 Cylinder sizes and separations at selected frequencies. 22

2.2 Tissue properties of five region phantom. 36

3.1 Transmission line parameters. 46

Symbols and Acronyms

Symbol	Description
$\hat{x}, \hat{y}, \hat{z}$	Rectangular unit vectors
$\hat{r}, \hat{\phi}, \hat{z}$	Cylindrical unit vectors
\mathbb{C}	Set of complex numbers
ϵ	Permittivity (F/m)
ϵ_r	Relative permittivity
χ	Contrast
λ	Wavelength (m)
ω	Angular Frequency (rad/s)
f	Frequency (Hz)
E^{inc}	Incident electric field (V/m)
E^{sct}	Scattered electric field (V/m)
E^{tot}	Total electric field (V/m)
H^{inc}	Incident magnetic field (A/m)
H^{sct}	Scattered magnetic field (A/m)
H^{tot}	Total magnetic field (A/m)

Acronym	Description
2D	Two Dimensional
3D	Three Dimensional
ABC	Absorbing Boundary Condition
CNC	Computer Numerical Control
CPW	Co-planar Waveguide
<i>E</i>-field	Electric field
EIL	Electromagnetic Imaging Laboratory
EMC	Electromagnetic Compatibility
GPIB	General Purpose Interface Bus
GTEM	Gigahertz Transverse Electromagnetic
<i>H</i>-field	Magnetic field
HFSS	High Frequency Structural Simulator
IF	Intermediate Frequency
LED	Light Emitting Diode
MWI	Microwave Imaging
OI	Object of Interest
OC	Open Circuit
PCB	Printed Circuit Board
PEC	Perfect Electric Conductor
PDC	Probe Driver Circuit
RAM	Radiation Absorbent Material
RF	Radio Frequency
SC	Short Circuit
SMA	Sub-miniature "A"
TC	Tuned Circuit
TEM	Transverse Electromagnetic
U of M	University of Manitoba
VNA	Vector Network Analyzer

Chapter 1

Introduction

Medical imaging is an essential tool for modern medicine. A variety of imaging modalities exist, including but not limited to magnetic resonance imaging (MRI), x-ray computed tomography (CT), positron emission tomography (PET), and ultrasound. Each of these technologies have important roles in different areas of health care, though they each have their own disadvantages. MRI provides excellent soft tissue resolution, but machines are very large and expensive. Any modality involving x-rays has inherent harmful side effects due to the ionizing nature of the radiation. For these reasons, medical imaging using electromagnetic radiation in the microwave portion of the spectrum has emerged as a topic of great interest with a variety of applications, including breast cancer monitoring and detection [1, 2, 3], head imaging [4, 5], and lung cancer detection [6]. Microwave radiation is non-ionizing, therefore making it a safe modality without the harmful side effects of ionizing radiation. Furthermore, microwave imaging (MWI) systems cost much less than other modalities, making it viable for medical imaging in developing countries where the costs associated with technologies such as MRI make access currently impossible. MWI does have its drawbacks though, including difficulties in resolving very fine targets, accurately recovering true tissue properties, and limited sensitivity to small changes in contrast [1, 7].

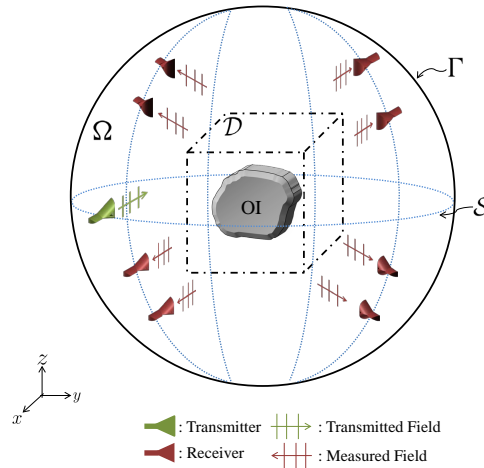


Figure 1.1: Three dimensional model of the MWI problem. Image used with permission from Dr. Amer Zakaria.

This work focuses on breast cancer imaging. Biological tissues have distinct and different dielectric properties, quantified by the complex permittivity which accounts for the dielectric constant and loss of the tissue, which allows for differentiation at microwave frequencies. Of particular importance, malignant tumour tissue exhibits different dielectric properties from other healthy tissues present in a human breast [8]. A further benefit of MWI is that it not only results in qualitative images, but quantitative images as well. The reconstructed dielectric properties relate to actual tissue properties. It is therefore important for diagnostic purposes that MWI results are accurate so that tissues are properly classified. This thesis focuses on the development of a novel MWI system for breast cancer detection that takes advantage of recent developments in the field.

1.1 Microwave Imaging and Contrast Source Inversion

This section details the mathematical foundation of the MWI problem and gives an overview of the Contrast Source Inversion technique used to solve it.

A diagram showing the general setup of the MWI problem is shown in Figure 1.1, where

the OI is the object of interest, Ω is the problem domain, \mathcal{D} is the imaging domain, Γ is the problem boundary, and \mathcal{S} is the surface on which the transmitters and receiver are located. Herein, we define the incident fields, \vec{E}_t^{inc} and \vec{H}_t^{inc} , produced by a given transmitter t as the fields in Ω with no OI present in \mathcal{D} . Similarly, the total fields, \vec{E}_t^{tot} and \vec{H}_t^{tot} , are defined as the fields in Ω when there is an OI present in \mathcal{D} . Note that the media in Ω need not be homogeneous. We then define the scattered fields \vec{E}_t^{sct} and \vec{H}_t^{sct} as

$$\vec{E}_t^{sct} \triangleq \vec{E}_t^{tot} - \vec{E}_t^{inc} \quad (1.1)$$

$$\vec{H}_t^{sct} \triangleq \vec{H}_t^{tot} - \vec{H}_t^{inc}. \quad (1.2)$$

One transmitter acts as a source of electromagnetic radiation at a given frequency (or set of discrete frequencies), and the receivers collect the fields. This process is usually repeated for a number of different transmitters, which results in a number of measured scattered field quantities on \mathcal{S} due to the presence of an OI in \mathcal{D} .

The goal of MWI is to obtain this scattered-field data and then invert it to reconstruct the dielectric properties of the OI in \mathcal{D} . This inversion step presents many challenges, as the problem is both non-linear and ill-posed. The solution is not unique; more than one OI could produce the same scattered field data at the receiver points. Furthermore, the solution is often unstable, making it sensitive to noise. The problem may be solved using an iterative algorithm, such as Gauss Newton Inversion (GNI) [9] or Contrast Source Inversion (CSI) [10]. Only CSI is used in this work, and more details on CSI and its implementation are contained in Section 1.1.2.

1.1.1 Mathematical Formulation of the Imaging Problem

The mathematical formulation of the microwave imaging problem [11] begins with Maxwell's equations. In this work, all electromagnetic field quantities are assumed to be

time harmonic, *i.e.* having a $e^{j\omega\tau}$ time dependency, where $j^2 = -1$, ω is angular frequency, and τ is time. Maxwell's equations in their differential time-harmonic form are given by:

$$\nabla \times \vec{E}(\vec{r}) = -j\omega\mu(\vec{r})\vec{H}(\vec{r}) \quad (1.3)$$

$$\nabla \times \vec{H}(\vec{r}) = j\omega\varepsilon(\vec{r})\vec{E}(\vec{r}) + \vec{J}_i(\vec{r}) \quad (1.4)$$

$$\nabla \cdot \varepsilon(\vec{r})\vec{E}(\vec{r}) = \rho(\vec{r}) \quad (1.5)$$

$$\nabla \cdot \mu(\vec{r})\vec{H}(\vec{r}) = 0 \quad (1.6)$$

where the vector quantities \vec{E} , \vec{H} , \vec{J}_i , are respectively the electric field intensity in [volts/meter], the magnetic field intensity in [amperes/meter], and the impressed electric current density in [amperes/meter²]. Additionally, \vec{r} is the spatial position vector. The conduction current density, \vec{J}_c ($\vec{J} = \vec{J}_c + \vec{J}_i$), is accounted for by a complex representation of the scalar permittivity ε in [Farads/meter], where:

$$\varepsilon(\vec{r}) = \varepsilon_r(\vec{r})\varepsilon_0 \quad (1.7)$$

$$\varepsilon_r(\vec{r}) = \varepsilon'_r(\vec{r}) - j\varepsilon''_r(\vec{r}) \quad (1.8)$$

$$\varepsilon_r(\vec{r}) = \varepsilon'_r(\vec{r}) - j\varepsilon_{pl}(\vec{r}) - j\frac{\sigma(\vec{r})}{\omega\varepsilon_0} \quad (1.9)$$

and the constitutive relation $\vec{J}(\vec{r}) = \sigma(\vec{r})\vec{E}(\vec{r})$ is invoked. σ is the conductivity in [Siemens/meter], $\varepsilon_{pl}(\vec{r})$ is due to polarization loss, and ε_0 is the permittivity of free space. The other scalar quantities μ and ρ are the permeability in [Henrys/meter] and the electric charge density in [coulombs/meter³]. In the following formulation of the MWI problem, we assume no magnetic materials ($\mu(\vec{r}) = \mu_0$, the permeability of free space) and isotropic linear media. Under these assumptions, we can rearrange Equation 1.3 and substitute it into Equation

1.4, and arrive at the inhomogeneous vector wave (or Helmholtz) equation:

$$\nabla \times \nabla \times \vec{E}(\vec{r}) - \omega^2 \mu_0 \varepsilon_0 \varepsilon_r(\vec{r}) \vec{E}(\vec{r}) = -j\omega \mu_0 \vec{J}_i(\vec{r}) \quad (1.10)$$

Conventionally, the incident field is defined as the field in Ω with a background medium of uniform relative permittivity ε_b . However, this formulation allows the incident field to be defined with respect to an arbitrary non-uniform numerical background medium of relative permittivity $\varepsilon_n(\vec{r})$. Therefore, with no OI present, the incident fields satisfy the equation:

$$\nabla \times \nabla \times \vec{E}_t^{inc}(\vec{r}) - k_n^2(\vec{r}) \vec{E}_t^{inc}(\vec{r}) = -j\omega \mu_0 \vec{J}_t(\vec{r}) \quad (1.11)$$

in Ω , where $\vec{J}_t(\vec{r})$ is the impressed current source from transmitter t , and $k_n(\vec{r})$ is the wavenumber of the numerical background (the medium in Ω with no OI), defined as:

$$k_n^2(\vec{r}) = \omega^2 \mu_0 \varepsilon_0 \varepsilon_n(\vec{r}) \quad (1.12)$$

Similarly, when an OI is present in \mathcal{D} , the total fields satisfy:

$$\nabla \times \nabla \times \vec{E}_t^{tot}(\vec{r}) - k^2(\vec{r}) \vec{E}_t^{tot}(\vec{r}) = -j\omega \mu_0 \vec{J}_t(\vec{r}) \quad (1.13)$$

where the wavenumber $k^2(\vec{r}) = \omega^2 \mu_0 \varepsilon_0 \varepsilon_r(\vec{r})$ and $\varepsilon_r(\vec{r})$ is the permittivity of the media in Ω with the OI present.

Now, using the relationship defined in Equation 1.1, substituting it for $\vec{E}_t^{tot}(\vec{r})$ in Equation 1.13, and also using Equation 1.12, we arrive at

$$\nabla \times \nabla \times \vec{E}_t^{sct}(\vec{r}) - k^2(\vec{r}) \vec{E}_t^{sct}(\vec{r}) = (k^2(\vec{r}) - k_n^2(\vec{r})) \vec{E}_t^{inc}(\vec{r}) \quad (1.14)$$

Next, we define the contrast $\chi(\vec{r})$ as

$$\chi(\vec{r}) \triangleq \frac{\varepsilon_r(\vec{r}) - \varepsilon_n(\vec{r})}{\varepsilon_n(\vec{r})} \quad (1.15)$$

Note that $\chi \equiv 0$ outside of \mathcal{D} .

Now, including the contrast in Equation 1.14, and moving all contrast terms to the right hand side, we obtain

$$\nabla \times \nabla \times \vec{E}_t^{sct}(\vec{r}) - k_n^2(\vec{r})\vec{E}_t^{sct}(\vec{r}) = k_n^2(\vec{r})\chi(\vec{r})\vec{E}_t^{tot}(\vec{r}) \quad (1.16)$$

We now define the contrast source $\vec{w}_t(\vec{r})$ as

$$\vec{w}_t(\vec{r}) \triangleq \chi(\vec{r})\vec{E}_t^{tot}(\vec{r}) \quad (1.17)$$

leading finally to:

$$\nabla \times \nabla \times \vec{E}_t^{sct}(\vec{r}) - k_n^2(\vec{r})\vec{E}_t^{sct}(\vec{r}) = k_n^2(\vec{r})\vec{w}_t(\vec{r}) \quad (1.18)$$

This equation relates the scattered fields in Ω to the contrast sources $\vec{w}_t(\vec{r})$ present only in \mathcal{D} . It can be written in operator notation as:

$$\vec{\mathcal{H}}_b \left\{ \vec{E}_t^{sct} \right\} = k_n^2(\vec{r})\vec{w}_t(\vec{r}) \quad (1.19)$$

In MWI, \vec{E}_t^{tot} and \vec{E}_t^{inc} (and therefore \vec{E}_t^{sct} indirectly) can only be measured outside of \mathcal{D} , and obtaining the contrast sources in \mathcal{D} is the challenging ill-posed problem to be solved.

1.1.2 Finite Element Method Contrast Source Inversion

The MWI problem is solved using an inversion algorithm. As previously mentioned, several different algorithms can be used, but this work utilizes the Finite Element Method (FEM) CSI algorithm. An FEM-CSI algorithm has been developed in the Electromagnetic

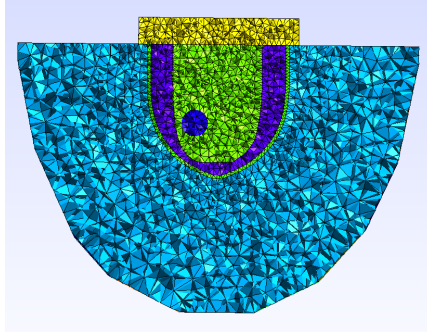


Figure 1.2: Sample 3D mesh created with Gmsh.

Imaging Laboratory (EIL) at the University of Manitoba (U of M) that can invert scattered field data in 2D and 3D problems [12, 13]. This FEM-CSI algorithm allows for an inhomogeneous background $\varepsilon_n(\vec{r})$, as well as the definition of Γ as a perfect electric conductor (PEC) or absorbing boundary, or a combination of the two.

The use of a FEM formulation allows for structures with complicated geometry (such as anatomical features) to be more easily represented. The problem domain, Ω , is discretized into a number of tetrahedrals with a user-definable edge length. This characteristic length need not be constant over Ω , allowing for precise modeling of small targets, smaller element size in high permittivity (and therefore short wavelength) targets, and more coarse discretization when appropriate. In this work, all FEM meshes are generated using Gmsh [14] for use with the FEM-CSI algorithm. A sample mesh is pictured in Figure 1.2. In this section, the underbar notation (*e.g.* $\underline{\chi}$) represents a discrete vector of values. Bolded capital letters such as \mathcal{M} indicate discrete matrix quantities.

CSI is an optimization algorithm that minimizes the following cost functional over the vectors $\underline{\chi}$ and \vec{w}_t

$$\mathcal{F}^{CSI}(\underline{\chi}, \vec{w}_t) = \mathcal{F}^{\mathcal{S}}(\vec{w}_t) + \mathcal{F}^{\mathcal{D}}(\underline{\chi}, \vec{w}_t) \quad (1.20)$$

The first term, $\mathcal{F}^{\mathcal{S}}$, is the normalized data-error and the second term, $\mathcal{F}^{\mathcal{D}}$, is the normalized

domain-error, each given by:

$$\mathcal{F}^{\mathcal{S}}(\vec{w}_t) = \frac{\sum_t \left\| \vec{E}_t^{\text{sct, meas}} - \vec{\mathcal{M}}_{\mathcal{S},t} \vec{\mathcal{L}}[\vec{w}_t] \right\|_{\mathcal{S}}^2}{\sum_t \left\| \vec{E}_t^{\text{sct, meas}} \right\|_{\mathcal{S}}^2} \quad (1.21)$$

$$\mathcal{F}^{\mathcal{D}}(\underline{\chi}, \vec{w}_t) = \frac{\sum_t \left\| \underline{\chi} \odot \vec{E}_t^{\text{inc}} - \vec{w}_t + \underline{\chi} \odot \vec{\mathcal{M}}_{\mathcal{D}} \vec{\mathcal{L}}[\vec{w}_t] \right\|_{\mathcal{D}}^2}{\sum_t \left\| \underline{\chi} \odot \vec{E}_t^{\text{inc}} \right\|_{\mathcal{D}}^2} \quad (1.22)$$

Each of these terms is sequentially updated as the functional is minimized [13]. Note that although the FEM-CSI algorithm has built-in multiplicative regularization [15], it is not used in this work. The dimensions and definitions of the variables and operators in the error terms are listed below, where R is the number of receivers per transmitter, I is the number of tetrahedral centroids in the imaging domain \mathcal{D} , and E is the number of mesh edges in \mathcal{D} .

- $\vec{w}_t \in \mathbb{C}^I$, the contrast source spatial-vector fields at the mesh centroids in \mathcal{D} .
- $\underline{\chi} \in \mathbb{C}^I$, the contrast values at the mesh centroids in \mathcal{D} .
- $\vec{E}_t^{\text{sct, meas}} \in \mathbb{C}^R$, the measured scattered field data at the receiver locations on \mathcal{S} .
- $\vec{\mathcal{L}} \in \mathbb{C}^{E \times I}$, the inverse FEM operator ($\vec{\mathcal{H}}_b$ in Equation 1.19). $\vec{\mathcal{L}}$ operates on a contrast source vector and produces the scattered field at the E mesh edges in \mathcal{D} .
- $\vec{\mathcal{M}}_{\mathcal{S},t} \in \mathbb{C}^{R \times E}$, a matrix operator that maps scattered field values calculated on the edges in \mathcal{D} to the receiver locations on \mathcal{S} .
- $\vec{\mathcal{M}}_{\mathcal{D}} \in \mathbb{C}^{I \times E}$, a matrix operator that maps scattered field values calculated on the edges in \mathcal{D} to the centroids in \mathcal{D} .

The electric field sources used in the FEM-CSI algorithm are modeled as infinitesimal Hertzian electric dipoles. These can have an arbitrary polarization (specified in cartesian

coordinates), and arbitrary location \vec{r}_t . They are assumed to be radiating in an infinite homogeneous medium with wavenumber k and dyadic Green's function given by

$$\bar{\bar{G}}(\vec{r}, \vec{r}_t) = \left(\bar{\bar{I}} + \frac{\nabla \nabla}{k^2} \right) \frac{e^{-jk|\vec{r}-\vec{r}_t|}}{4\pi|\vec{r}-\vec{r}_t|} \quad (1.23)$$

where \vec{r} is an arbitrary observation point. The field produced by a given transmitter in a homogeneous medium at an observation point is then

$$\vec{E}_t(\vec{r}) = -j\omega\mu_0 \vec{J}_t \cdot \bar{\bar{G}}(\vec{r}, \vec{r}_t) \quad (1.24)$$

where \vec{J}_t has unit magnitude and is located at \vec{r}_t and directed along the desired polarization. The magnetic source model in the algorithm is simply the magnetic dual of Equation 1.24 [16]. When Ω is finite and/or an inhomogeneous medium is present as a numerical background, $\vec{E}_t(\vec{r})$ is first computed and then the finite boundary and/or inhomogeneous medium is treated as a scatterer, and the incident field, $\vec{E}_t^{inc}(\vec{r})$, is calculated as the sum of this scattered field and $\vec{E}_t(\vec{r})$. More details on FEM-CSI and the optimization process can be found in [13, 17].

1.1.3 Prior Information

When the OI in a MWI problem is complicated (contains a variety of permittivity values and distributions), it can be difficult for the FEM-CSI algorithm to arrive at a good solution. Incorporating prior information about the OI into the algorithm has been shown to dramatically improve imaging results [18, 19]. If approximate dielectric properties and positioning information are known about the OI, they can be incorporated into $\varepsilon_n(\vec{r})$. Recall that $\chi(\vec{r})$ is defined in Equation 1.15.

The closer $\varepsilon_n(\vec{r})$ is to $\varepsilon_r(\vec{r})$, the lower $\chi(\vec{r})$ will be, and the easier the problem will be to solve. Note that in the EIL's FEM-CSI algorithm, this prior information is not the same

as an initial guess of the OI. As the algorithm iterates, the contrast is always defined with respect to the original $\varepsilon_n(\vec{r})$. The incident field with an inhomogeneous prior information background \vec{E}^{inc} is equivalent to the the total numerical field calculated with the $\varepsilon_n(\vec{r})$ acting as an OI in some homogeneous ε_b . Therefore, when calculating the scattered field of some OI when there is prior information, the scattered field is given by $\vec{E}^{sct} = \vec{E}^{tot} - \vec{E}^{inc}$, where the incident field is with respect to $\varepsilon_n(\vec{r})$.

In a clinical application, patient specific prior information must be obtained in some way. Researchers at the University of Calgary have developed a radar based method of experimentally determining “regions of interest” in a phantom [20]. These regions can then be incorporated into the MWI algorithm in order to improve imaging results [19]. These methods are not explored further in this work, but are noted as possible ways for experimentally obtaining prior information. More details of how prior information is used by the FEM-CSI algorithm can be found in [21].

1.1.4 MWI Systems

Beyond the algorithms used in MWI, designing and constructing experimental MWI can be challenging. In order to be useful, a numerical model of the system must be created, and be computationally manageable. Typically, an MWI system consists of an imaging chamber into which the OI is placed, wherein a number of co-resident antennas are located for transmitting and/or receiving electromagnetic radiation [3, 22, 23, 24]. These antennas are connected to a microwave source/receiver (often a Vector Network Analyzer (VNA)), usually through some microwave switching network to allow for many combinations of transmit/receive antennas. A simple system architecture is pictured in Figure 1.3. A host personal computer (PC) interacts with the measurement equipment to complete the data-acquisition system. More details on MWI systems and the required calibration methods are found in Chapter 4.

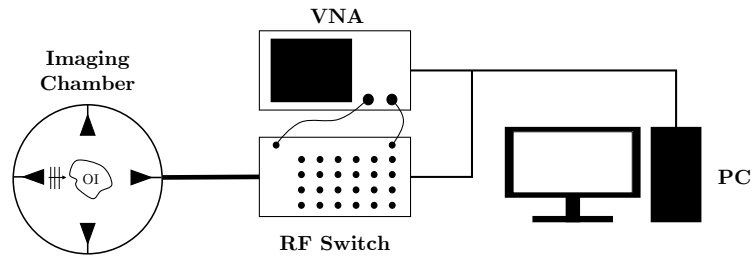


Figure 1.3: MWI system architecture.

1.2 Motivation

Currently, in a typical MWI system, the breast is immersed in a matching liquid with known dielectric properties close to the average properties of the breast [25, 26]. This selection of a liquid works by coupling as much microwave energy as possible from the source into the breast. However, there are some drawbacks to the use of a matching liquid. For one, all the electrical components inside the the chamber must be designed to operate in the fluid and must be protected from damage or short circuiting. Furthermore to ensure a safe and sterile environment, cleaning the system is important, and commonly used fluids such as glycerin/water mixes [25] and canola oil [26] can be difficult to clean thoroughly. Finally, due to the buoyancy of the breast in different mediums, it can be difficult to maintain the same positioning for a given patient in subsequent scans.

Recent developments in MWI research in the EIL have lead to an immersion medium independent inversion procedure which makes use of the FEM-CSI's ability to incorporate a numerical background. Numerical results show that with the appropriate incorporation of prior information, imaging of breast tissue in an air background is possible [21]. The primary goal of this work is to develop a system to experimentally validate these synthetic results.

Another recent development in the EIL that this work builds on is the measurement

and inversion of tangential magnetic field data near the inner surface of perfect electric conductor (PEC) enclosure walls. Using this magnetic field data (which is equivalent to the surface current), as opposed to electric field data has shown significant improvements in stored grain monitoring applications of MWI [16]. This thesis examines this development for breast imaging applications.

By developing an MWI system that does not require a matching medium and that uses magnetic field data, this work takes the next step towards a clinical microwave imaging system.

1.3 Outline

In Chapter 2 several synthetic studies are conducted in order to develop and validate a novel air based chamber design. Therein, a novel faceted hemi-ellipsoidal geometry is introduced and compared to a standard cylindrically shaped chamber. Upon validation, two different synthetic breast phantoms are imaged using electric and magnetic field data. The results show that the new faceted geometry offers advantages over a common cylindrical chamber, and using $\hat{\phi}$ -directed magnetic field data for inversion yields superior results. Furthermore, this section demonstrates that with the proper incorporation of prior information, breast targets can be imaged in the novel chamber in an air background.

Chapter 3 details the development of magnetic field probes for use in the novel experimental system. Several prototype half-loop probes are built and tested in a GTEM (Gigahertz Transverse Electromagnetic) cell. A grounded co-planar waveguide design is selected as the best performer from the prototypes, and the design is refined with the addition of an RF diode to make the probe reconfigurable. Several tests are done to assess the probe's performance in magnetic field detection and electric field rejection. The resultant design is suitable for the experimental imaging system.

The manufacturing, assembly, and testing of the faceted chamber design introduced in

Chapter 2 is detailed Chapter 4. The magnetic-field probes documented in Chapter 3 are tested in the chamber, and incident field modeling is compared between the experimental system and the numerical model with good results. Subsequently, simple cylindrical targets were imaged in the experimental system using a variety of different measurement and calibration techniques. The resultant data and reconstructed images are compared to synthetic equivalents and optimal techniques for the novel system are determined. This chapter verified that images of simple targets can be obtained with the novel system.

Chapter 5 documents imaging trials with a simple breast phantom with a tumour inclusion. The data collection techniques selected in Chapter 4 are used to invert the measured data first without, and then with, prior information. Two different techniques for incorporating prior information are explored. Experimental imaging results show that at certain frequencies, both prior information techniques result in reconstructions where the tumour inside the simple phantom is detectable.

The work is summarized and concluded in Chapter 6. Future areas of work that could improve imaging results are also listed.

1.3.1 Limitations to the Scope

Developing clinical MWI systems requires work in a variety of areas, such as algorithm development, hardware design, antenna/probe design, and data processing. As such, there are necessary limits on what options and alternatives can be explored in this work. Radar-based imaging techniques are not explored herein. The existing FEM-CSI code developed by other researchers from the EIL is used without modification. All imaging studies in this work are done in full 3D, and no 2D cases are considered. The breast phantoms used in the synthetic and experimental tests are simplified versions of their true anatomical counterparts. More complicated MRI derived breast phantoms have been examined in the EIL in 2D microwave tomography [19].

Chapter 2

Synthetic Development of a Faceted Chamber

This chapter details a series of synthetic studies conducted in order to arrive at a novel MWI chamber. The primary goals in developing a new chamber are to make a system that reduces modeling error, performs without the need of a matching medium (such as glycerin), and takes advantages of novel developments in using PEC imaging chambers.

To date, many MWI systems use canonical shapes for chambers and simple symmetrical arrangements of transceivers. Examples include a PEC walled rectangular chamber for breast imaging [24], a PEC walled cylinder for arm and animal tissue imaging [27], an open cylindrical chamber for low contrast targets [28], and an open cylindrical chamber for head imaging [29]. Lately, some systems have been developed that feature non-canonical shapes that often conform as closely as possible to the intended OI, such as a cup shape for breast imaging [30] or a helmet shape for head imaging [4]. Using a chamber shape that is similar to the OI offers several advantages such as reduction in chamber volume leading to smaller (and less computationally burdensome) numerical problems and direct coupling of microwave energy into the OI, without a background medium. However, they do require

Careful antenna design, since the antennas are usually in direct contact with the OI.

As already introduced, many MWI systems feature PEC walled chambers. Using a PEC wall provides many advantages. The most obvious advantage is that the chamber walls shield the system from outside noise. A second advantage is that the PEC walls form a well defined, easy to model boundary. In contrast, when implementing an open boundary chamber, it must be surrounded by radar absorbers [28], or accept the increase in modeling error due to the presence of un-modeled objects in the vicinity of the chamber. Another benefit is that the PEC walls trap electromagnetic energy inside the chamber, leading to greater field strengths which along with the shielding property, lead to an improved signal-to-noise ratio. This feature can present a potential drawback when all the chamber walls are metallic and there is minimal loss inside the chamber. In this instance, the MWI chamber is highly resonant, and therefore very sensitive to perturbations [31]. This makes accurate modeling very important, as unaccounted for perturbations can significantly affect the modes and field distributions inside a chamber.

A final advantage of PEC walled chambers arises when the fields are measured very near to the PEC boundary. Research has shown that obtaining multiple polarizations in MWI systems can improve imaging results [23]. This makes intuitive sense, as more information is obtained when fully characterizing the field at a measurement location, though measuring all three polarizations at a given point presents technical challenges. However, at a PEC surface, there exists only one electric field polarization (normal to the surface) and two magnetic field polarizations (tangential to the surface). Therefore, measuring at (or very near to) a surface reduces the field data that one is required to measure, making it simpler to fully characterize the field at that location. This intuition has been validated in the EIL both synthetically and experimentally [16, 32].

2.1 A Faceted Hemi-Ellipsoid

With the advantages of a PEC walled chamber similar in shape to the intended OI in mind, a novel chamber geometry was conceived. The shape is based on a hemi-ellipsoid with an xy plane semi-axis $a = b = 11$ cm and a $-z$ semi-axis $c = 15$ cm. These dimensions are very similar to the system in [33], which was used for clinical trials with human volunteers, so the dimensions were known to accommodate a variety of breast sizes. Furthermore, these dimensions were the largest that the machining shop at the U of M could accommodate on the milling machine needed to fabricate the prototype chamber.

A further modification to the chamber geometry was made to reduce modeling error. The FEM-CSI code uses tetrahedrals with straight edges, which introduces modeling error when approximating a curved surface. At very fine discretizations, this ceases to contribute significant error, but fine discretization increases computational burden. Therefore, the hemi-ellipsoidal geometry was modified to be comprised of a number of flat facets instead of a smooth curved surface in order to decrease modeling error. The impact of this error reduction is examined in detail in the following section. To form the faceted geometry, first an arc length of 4 cm was chosen to be the average distance between two neighbouring facet centres. The hemi-ellipsoidal geometry was populated with 44 points, the maximum number of points that could fit inside the chosen ellipsoid size, when separated by no less than 4 cm arcs. This was done to ensure that any antennas or probes mounted in an experimental chamber would have sufficient separation between neighbouring antennas or probes. These 44 points were systematically arrayed in 5 concentric rings, and are shown in Figure 2.1. Then, 44 planes were constructed whose normal vectors were equal to the inward normal of the original hemi-ellipsoid at each of the respective points. The intersection of all 44 planes defines the chamber boundary. Due to the fact that each ring has a different number of facets, there is no symmetry in the chamber. A cross section of the resultant faceted geometry is pictured in Figure 2.2.

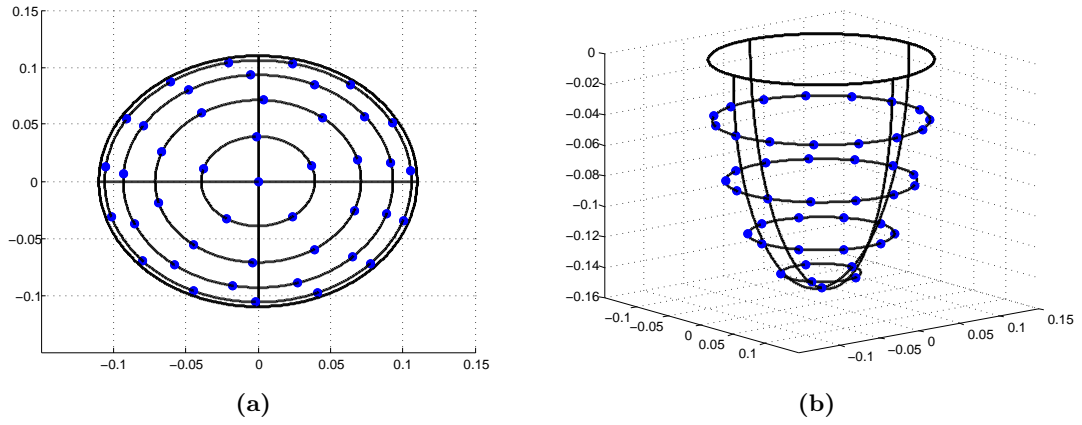


Figure 2.1: Facet centers, (a) top view and (b) side view.

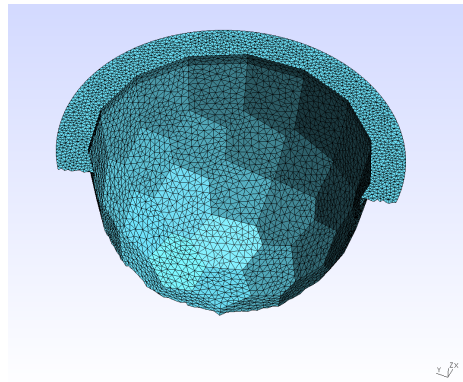


Figure 2.2: Cross section of faceted chamber finite element mesh.

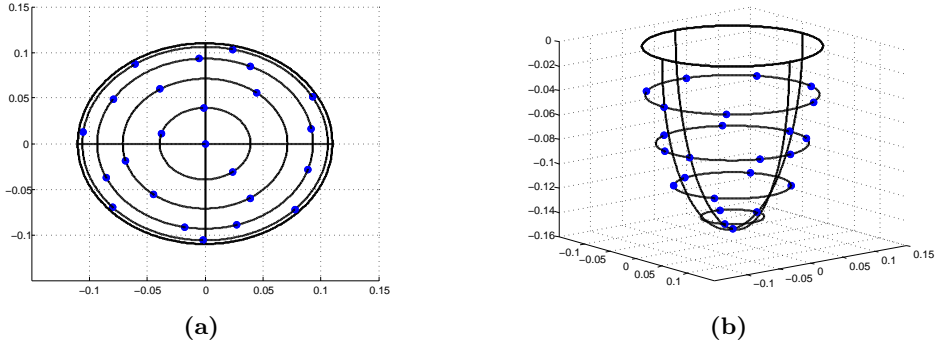


Figure 2.3: Transceiver positions, (a) top view and (b) side view.

Each of the 44 points also define the location for transceiver probes. However, since the EIL has a 2 to 24 RF switch to interface with transceivers, 24 points were selected from the 44 total so that all synthetic studies would reflect a replicable future experimental setup. These 24 positions were manually chosen to maintain as uniform a distribution as possible of transceiver locations over the chamber. The selected positions are shown in Figure 2.3. Decreasing the symmetry of the transceiver locations is advantageous, particularly in PEC chambers. If the positions were chosen in a standard symmetric columnar pattern, the modes excited in the chamber may not be sufficiently sampled to appropriately characterize the field distribution. This is why the transceiver positions are quasi-randomly arrayed in the chamber [32].

The next two subsections compare the performance of the novel faceted chamber to a similarly sized cylindrical chamber in order to assess the improvements in modeling error and imaging performance. This work was done in collaboration with Dr. Anastasia Baran. A $\hat{\phi}$ polarized magnetic field source/receiver was placed at each of the chosen 24 positions. The equivalent cylindrical chamber featured the same radius and height as the hemi-ellipsoid ($r = 11$ cm, $h = 15$ cm), and similar transceiver positions were used by shifting the faceted chamber positions outward towards the cylindrical chamber wall. The source positions and polarizations are shown in Figure 2.4.

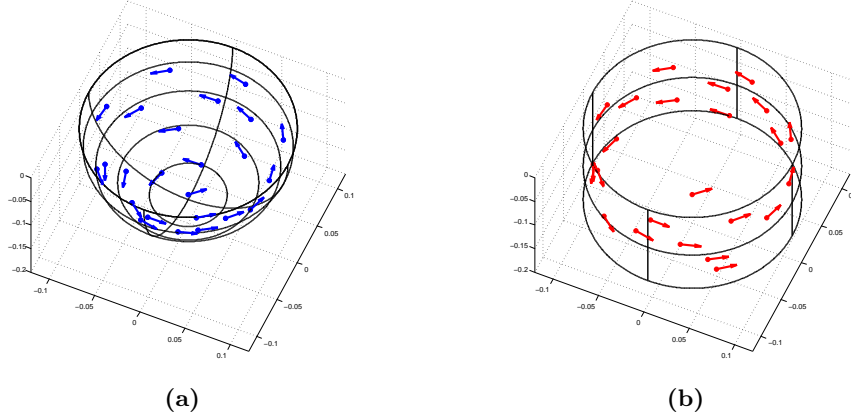


Figure 2.4: Transceiver positions, (a) faceted chamber and (b) cylindrical equivalent.

2.1.1 Modeling Flat Geometry

As previously stated, the curved surfaces of the cylindrical chamber are approximated by a number of tetrahedrals. The faceted chamber design features flat facets, which are exactly represented by the flat faceted tetrahedrals. A synthetic study was conducted in order to assess the numerical significance of this difference.

A “true” reference mesh, with $\lambda/50$ characteristic length at 1.5GHz, was created for both geometries. This mesh is considered sufficiently fine to represent the “true” incident field solution at the receiver points in the chamber. Meshes of each of the chamber geometries were created with characteristic lengths of $\lambda/10$, $\lambda/12$, $\lambda/14$, $\lambda/16$, $\lambda/18$, $\lambda/20$, $\lambda/25$, $\lambda/30$, $\lambda/40$. The incident magnetic fields were computed on each mesh and compared to the reference ($\lambda/50$) mesh. Additionally, due to random positioning of tetrahedrals each time a mesh is generated, producing some random variation in the computed incident field, a newly generated $\lambda/50$ mesh was also compared to the reference mesh, in order to establish a baseline error in our analysis. For the same reason, each mesh was generated five times, and the average L_2 error norm of the computed incident field was taken.

The results shown in Fig. 2.5 demonstrate that there is better modeling of the faceted

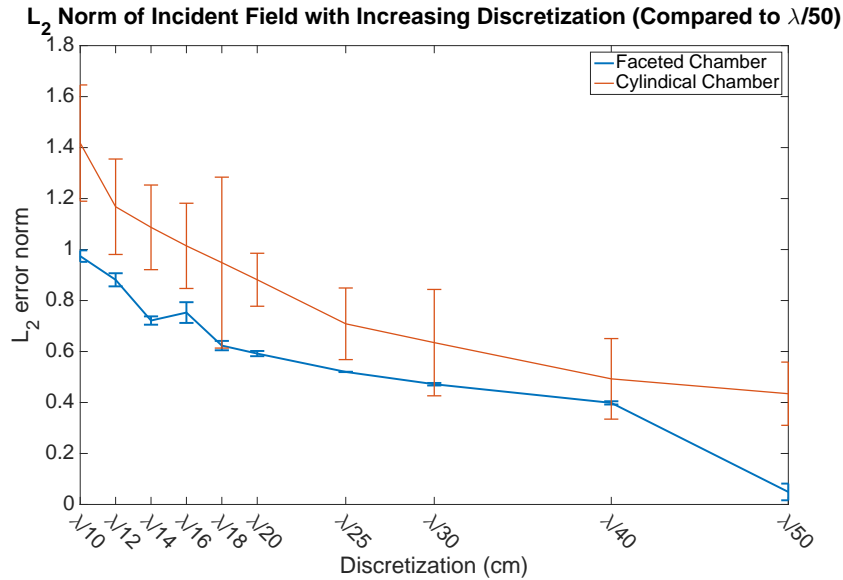


Figure 2.5: Comparison of incident field error as a function of mesh discretization.

chamber compared to the cylindrical chamber. The average L_2 error norm is consistently smaller for the faceted chamber, and the associated error bars follow the same trend. The comparison of incident fields collected on unique $\lambda/50$ meshes show that the faceted chamber is converging to solution near zero (which is ideal), while the cylindrical chamber is not. Furthermore, the larger error bars at every discretization for the cylindrical chamber indicate that this geometry is more dependent on the randomness in mesh generation than the faceted geometry.

2.1.2 Diversity of Data

Another advantage of the faceted chamber in comparison to a cylindrical chamber is the mixing of modes introduced by the asymmetrical shape. A cylindrical chamber has a number of well defined modes, and the work in [31] shows that inversion quality is dependent on how close the chosen frequency is to a dominant mode. In particular, near resonant frequencies inversion quality degrades. By using a chamber with a non-canonical shape which excites

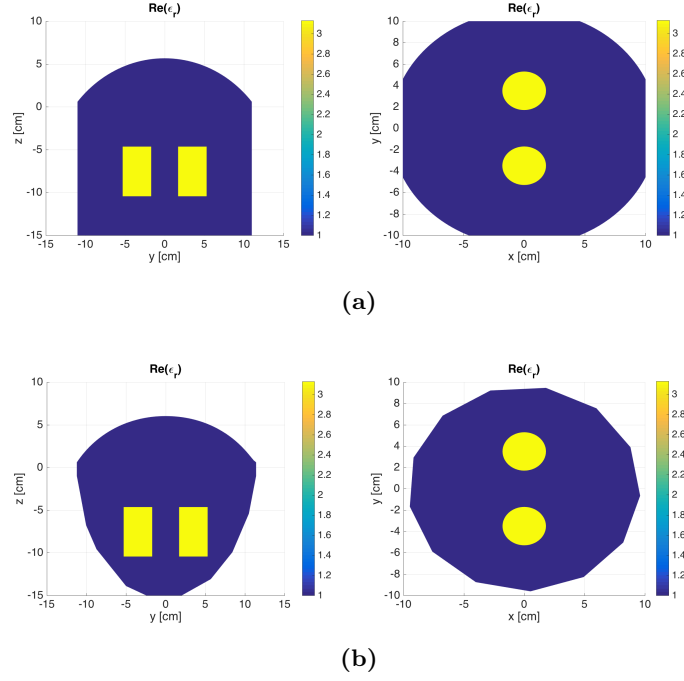


Figure 2.6: Cylindrical targets positioned in the (a) faceted chamber and (b) cylindrical equivalent.

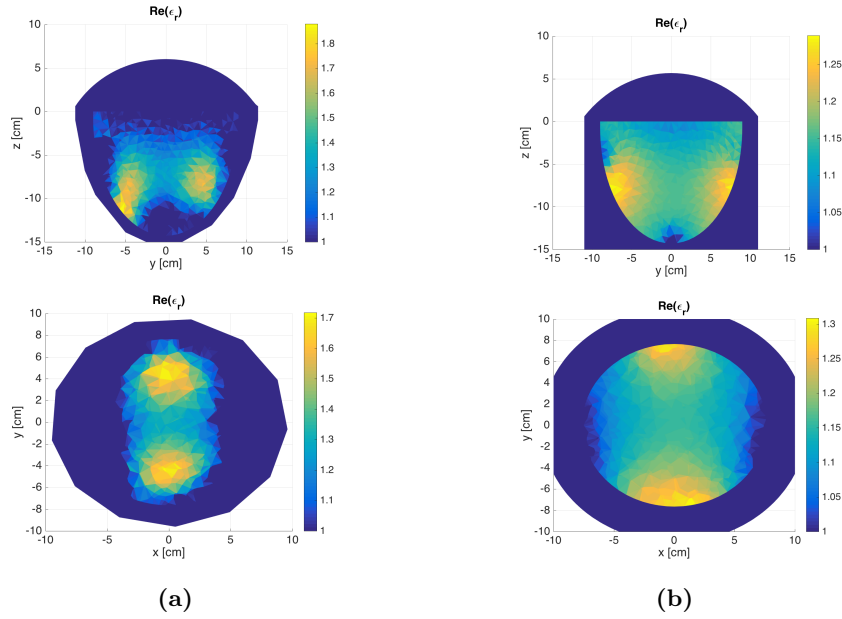
mixed modes, good inversion results should be obtainable at more frequencies compared to a cylindrical chamber.

This motivation was validated by imaging a simple OI at a variety of frequencies in both chambers and analyzing the reconstructions. The chosen OI is comprised of two cylindrical targets of the same size ($h = 5.6$ cm and $r = 1.8$ cm), separated by 3.5 cm, positioned partway down each chamber. Both chamber tops were left open with an absorbing boundary in the shape of a dome above the top opening. The targets in each chamber are pictured in Figure 2.6, and have a relative permittivity of $3.13 - j0.253$, embedded in an air background of $\epsilon_b = 1 - j0.001$.

Numerical forward data was generated using 24 H_ϕ polarized magnetic field sources at frequencies from 1 to 2 GHz in 50 MHz steps. The imaging domain was restricted to a hemi-ellipsoid that encompassed the target locations and remained a few centimeters from

Table 2.1: Cylinder sizes and separations at selected frequencies.

	Absolute	1 GHz	1.5 GHz	2 GHz
Height, h	5.6 cm	$\lambda/5.36$	$\lambda/3.57$	$\lambda/2.68$
Radius, r	1.8 cm	$\lambda/16.67$	$\lambda/11.11$	$\lambda/8.33$
Separation, d	3.5 cm	$\lambda/8.57$	$\lambda/5.71$	$\lambda/4.29$

**Figure 2.7:** Reconstructions at 1 GHz in (a) faceted and (b) cylindrical chambers.

the chamber walls. No noise was added in these inversions, and the FEM-CSI algorithm was terminated at 300 iterations. The results at 1 GHz, 1.5 GHz and 2 GHz are shown in Figures 2.7, 2.8, and 2.9 respectively. The respective object sizes and separations in terms of wavelength (in air) at these frequencies are given in Table 2.1.

In order to accurately assess the results, a simplified version of the error metric described in [34] is employed. First, for a given OI, the permittivity at each mesh tetrahedral is interpolated onto a cubic grid, and a “reference mask” **ref_mask** is constructed by creating a binary grid (corresponding to the permittivity grid), with a 1 where the OI is present

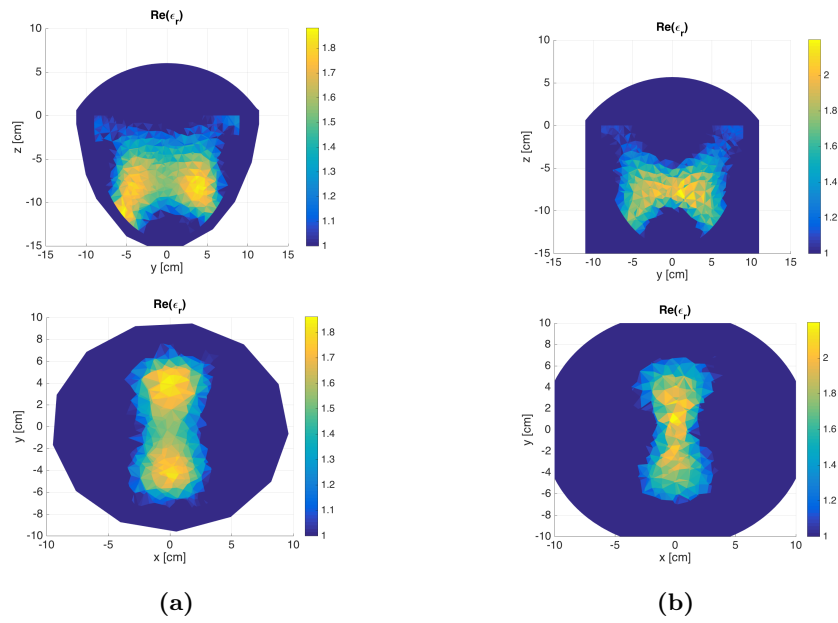


Figure 2.8: Reconstructions at 1.5 GHz in (a) faceted and (b) cylindrical chambers.

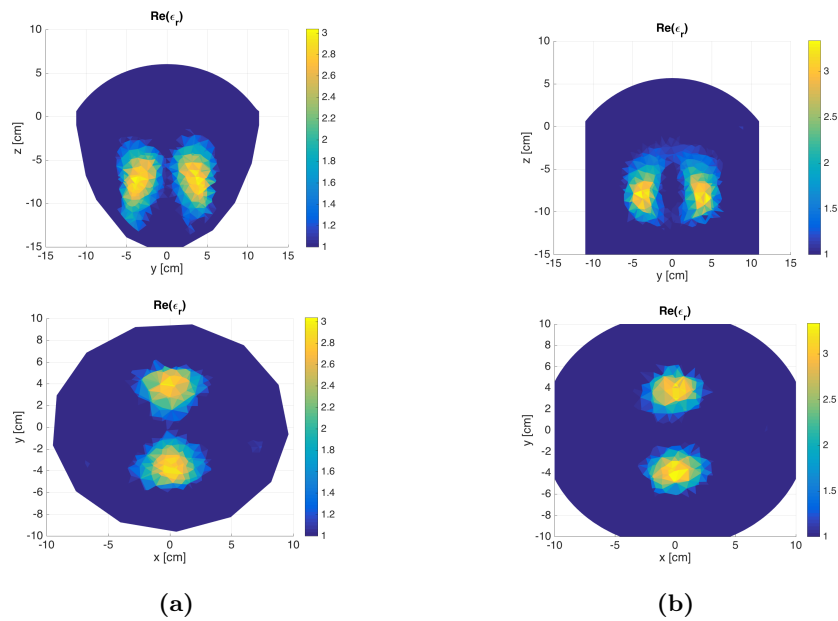


Figure 2.9: Reconstructions at 2 GHz in (a) faceted and (b) cylindrical chambers.

and a 0 where there is no OI present. Then, for each inversion result, a “reconstruction mask” **rec_mask** is created in a similar manner, where a binary grid is constructed from interpolated mesh data, where a 1 indicates that the reconstructed permittivity exceeds some threshold τ , and a 0 indicates that the reconstructed permittivity is below τ . For this study, τ is set to 15% of the maximum value of the reconstruction being evaluated.

With these two masks, three error metrics can be created. The Object Detection (OD) is given by

$$OD = \frac{\sum(\mathbf{ref_mask} \cap \mathbf{rec_mask})}{\sum \mathbf{ref_mask}} \quad (2.1)$$

where summation is over every element in the binary mask. OD must be between 0 and 1, where 1 indicates perfect detection of the OI, and 0 indicates no OI detection.

The second metric, artifact rejection (AR) is defined as:

$$AR = 1 - \frac{\sum \mathbf{rec_mask} - \sum(\mathbf{ref_mask} \cap \mathbf{rec_mask})}{\sum \mathbf{ref_mask}} \quad (2.2)$$

This metric gives a measure of what portion of the reconstruction outside the true OI region is identified as being part of the OI. An AR of 1 indicates perfect artifact rejection, and AR can be as small as $-\infty$ which corresponds to a very large number of artifacts. In this application, the sum of **ref_mask** is never zero, so the lower bound of AR is a large finite negative number.

We now define a final metric, termed the combined metric (CM) which is simply the sum of OD and AR , and can range from 2 (excellent reconstruction) to $-\infty$ which is a very poor reconstruction. Note that in this section, the metric is only calculated for the real part of the permittivity reconstruction.

One more modification was made to the metric presented in [34], because the initial results using the given metric were not useful in this application due to the large number

of low contrast artifacts that fall below τ but still visually degrade reconstruction quality. Two \mathcal{L}_2 error norms were computed and used to normalize *OD* and *AR*. The first error norm, ERR^{obj} is the \mathcal{L}_2 error norm between the phantom and reconstruction taken over coordinates inside the objects. The second norm, ERR^{bg} is the \mathcal{L}_2 error norm between the phantom and reconstruction taken over coordinates outside the objects. This results in a new combined metric:

$$CM2 = \frac{OD}{ERR^{obj}} + \frac{AR}{ERR^{bg}} \quad (2.3)$$

Due to the fact that the *AR* metric can range from 1 and $-\infty$, and since the values of the L_2 norms can vary significantly (from near zero to very large), there is no useful definition for the range of expected values from this combined metric, other than that larger values of *CM2* indicate a better result. However it is useful for directly comparable scenarios such as this one.

This metric was applied to all the reconstructions from the faceted and cylindrical chamber, and the results are pictured in Figure 2.10. These results verify the intuition that the data from a diverse modes in the faceted chamber leads to more broadband reconstruction quality. Though for some reconstructions the cylindrical chamber performs slightly better, overall the faceted chamber features improved reconstruction quality. The metric was also calculated for thresholds τ of 10%, 20%, and 25% with the same conclusion.

2.2 *E*-Field and *H*-Field Inversion in a Faceted Chamber

As previously discussed, imaging using data collected at a PEC boundary is a proven successful measurement technique [16, 32]. This section details synthetic imaging studies using different breast phantoms of varied complexity in the faceted chamber introduced in the previous section. For all the studies, 24 transceivers are used, located near the PEC

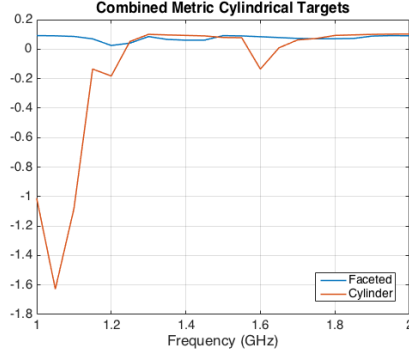


Figure 2.10: Combined and normalized error metric for the faceted and cylindrical chambers, $\tau = 15\%$.

boundary. Additionally, all breast targets reside in an air background and incorporate prior information.

The primary objective of this section is to determine the optimal electromagnetic field data to collect and use for inversion. Results from the use of different electric and magnetic field components are compared in otherwise identical measurement scenarios in order to inform the construction of an experimental system.

2.2.1 A Simple Two-Tumour Breast Phantom

The first phantom used is a simple two-tumour breast phantom, pictured in Figure 2.11. It features a single fat/fibroglandular region with two 1 cm radius spherical inclusions. The fat/fibroglandular region was assigned a permittivity of $\epsilon_{r-ft/fib} = 15.21 - j4.08$ which is between the permittivity of pure fat and pure fibroglandular tissue, and the tumours were assigned values of $\epsilon_{r-t1} = 42 - j14$ and $\epsilon_{r-t2} = 58 - j16$ [8]. This phantom is anatomically simplified which makes accurately assessing reconstructions easier.

Two different scenarios are used for the top boundary of the chamber above the phantom. The first is a PEC scenario, whose mesh is pictured in Figure 2.12a. The upper chamber boundary is a PEC surface, shown in black. Above the PEC surface is an air

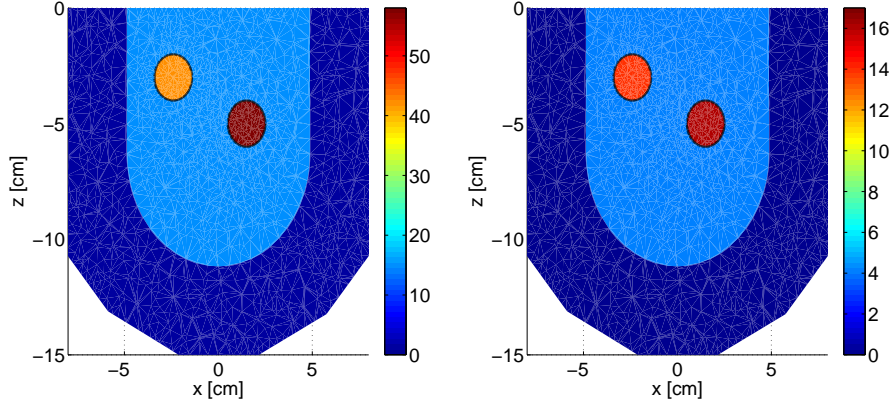


Figure 2.11: Cross-section of 3D two-tumour breast phantom. $Re(\epsilon_r)$ is on the left, $-Im(\epsilon_r)$ on the right.

region bounded by an ABC (shown in light blue), similar to the one described in Section 2.1.2. The second scenario, pictured in Figure 2.12b, features a plexiglass support structure surrounding the breast ($\epsilon_{r-plexi} = 3 - j0.001$) with an absorbing boundary condition (ABC) dome above it. These scenarios are chosen to mimic experimental phantom studies, where a breast phantom is suspended in the chamber either from a metal or plexiglass plate. They clearly are not representative of a scan of a patient, wherein a muscle wall and other tissues would be present above the breast. A more anatomically realistic scenario is examined later in Section 2.2.4.

For the two-tumour phantom, the exact properties (location and permittivity) of the fat/fibroglandular region and (when incorporated) the plexiglass plate were used as prior information. This is termed herein as “perfect prior,” indicating there is full knowledge of the phantom except for information pertaining to the tumours. In any experimental system, there will always be some degree of error in the measuring and incorporating prior information. The impact of errors in prior information has been examined in [34]. Similar studies are beyond the scope of this work, and therefore, “perfect prior” is assumed in the synthetic work of this Chapter. The purpose of these synthetic examples is solely to differ-

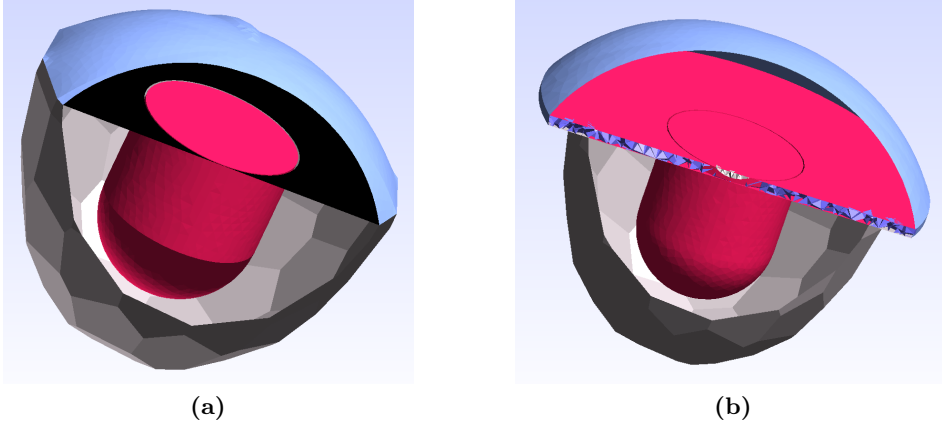


Figure 2.12: Two chamber top scenarios for the phantom (a) PEC and (b) plexiglass.

entiate the impact of different types of polarizations, not provide realistic prior information studies. Similar work is conducted in Appendix A with imperfect prior information.

2.2.2 E -Field and H -Field Measurements

As previously mentioned, assessing the impact of using different electromagnetic field components as data is of primary interest. At a PEC surface, there exists a normal electric field component and tangential magnetic field components. Therefore three different sets of field data are used, one electric field component and two orthogonal magnetic field components. The electric component directed along the inward normal, E_n , is calculated at the center of each facet of the chamber. One magnetic component is the $\hat{\phi}$ directed component H_ϕ , again with the direction vector calculated at the center of each facet. Finally, the second magnetic component was chosen to be the component orthogonal to both E_n and H_ϕ . This component is tangential to the facet, and termed herein H_z , though it is not a truly \hat{z} directed vector. The directions of the field components are pictured in Figure 2.13 at the centers of all 44 facets, though only 24 transceiver locations are used.

With these field components defined, numerical scattered field data was generated using

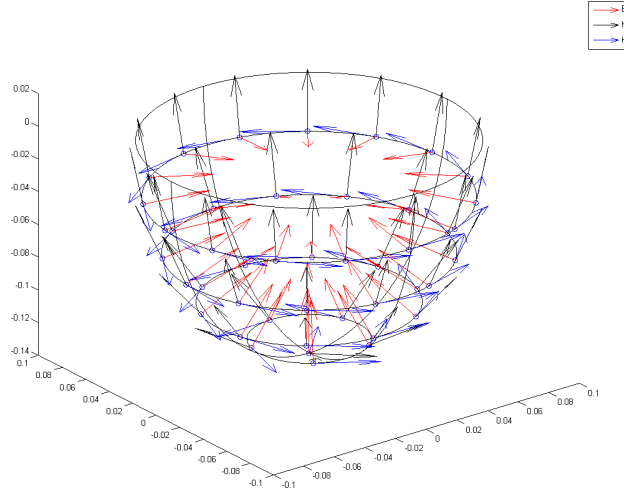


Figure 2.13: Electric and magnetic field polarizations.

the EIL's forward solver for the three field components for both the PEC and plexiglass top scenarios at frequencies from 0.9 to 1.5 GHz (steps of 50 MHz). The scattered field was computed with respect to the perfect prior background, as is standard practice in the EIL.

2.2.3 Inversion Results

The collected forward data was inverted on a different mesh with 5% noise added to the data in order to avoid inverse crime [35]. Each inversion was terminated at 250 iterations, and the imaging domain was restricted to a cylinder slightly larger than the breast region (radius 5.375 cm and height 12.475 cm). Due to the large number of inversion results (3 field components \times 2 chamber tops \times 13 frequencies), a small subset of the results are displayed here. Figures 2.14 and 2.15 show results at 0.9 GHz for the PEC and plexiglass scenarios respectively, while Figures 2.16 and 2.17 display the results for the same scenario at 1.3 GHz. As seen in these results, both tumours are detected, and the higher permittivity tumour has a high reconstructed permittivity than the lower permittivity tumour. The tumour

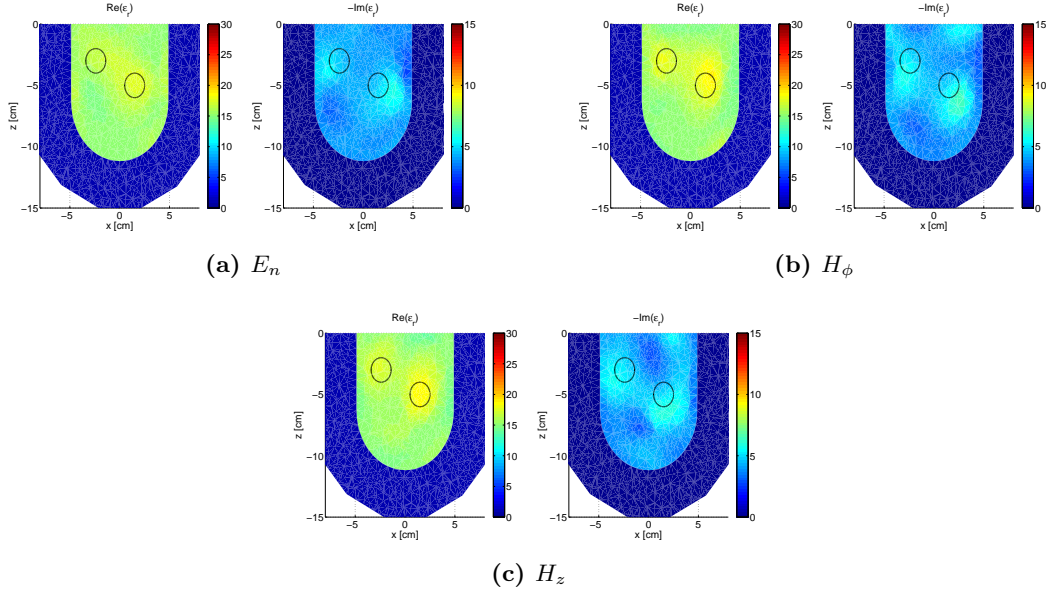


Figure 2.14: Results at 0.9 GHz for a PEC chamber top.

location is more accurate in the real part when compared to the imaginary reconstruction. In all cases, the reconstructed tumour permittivity is lower than the true permittivity. This is expected, and would improve (though likely not meet the true value) with more iterations of the CSI algorithm, but the reconstructions were terminated at 250 iterations due to computational time. Differences between the field components are clearly apparent, particularly at 1.3 GHz.

In order to accurately assess the results, the error metric described in [34] is again employed, this time without the \mathcal{L}_2 error normalization. To reiterate, after interpolating the mesh data onto a rectangular grid, reference and reconstruction masks are created, defined in the same way as in Section 2.1.2. Example binary masks are shown in Figure 2.18. Note that each metric here is calculated for the real and imaginary parts of ϵ_r separately.

With these two masks, the three error metrics can be created, just as before. The only difference is that here we term the Object Detection OD metric the tumour Detection (TD)

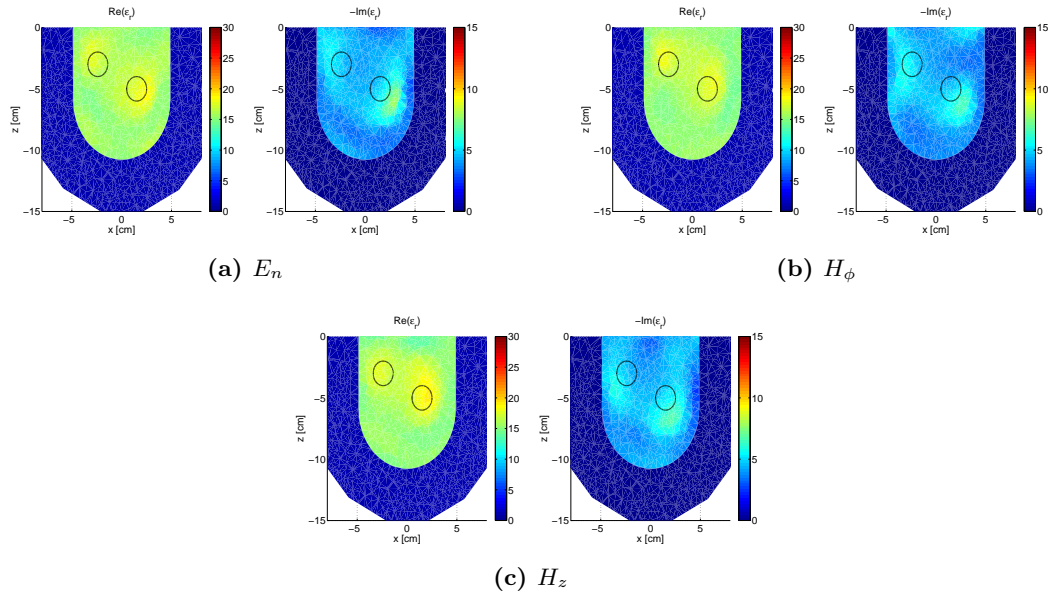


Figure 2.15: Results at 0.9 GHz for a plexiglass chamber top.

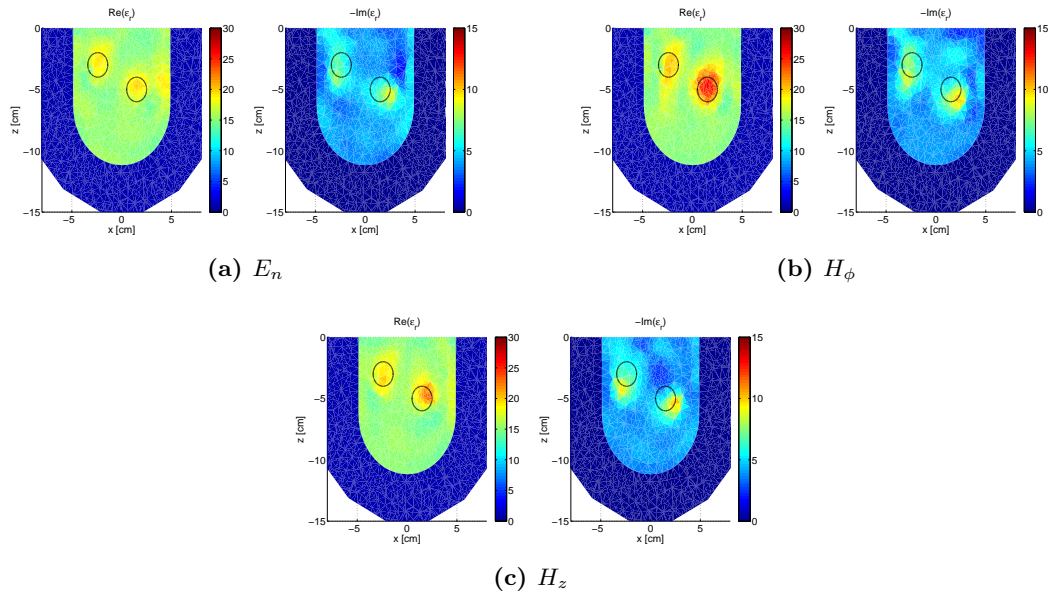


Figure 2.16: Results at 1.3 GHz for a PEC chamber top.

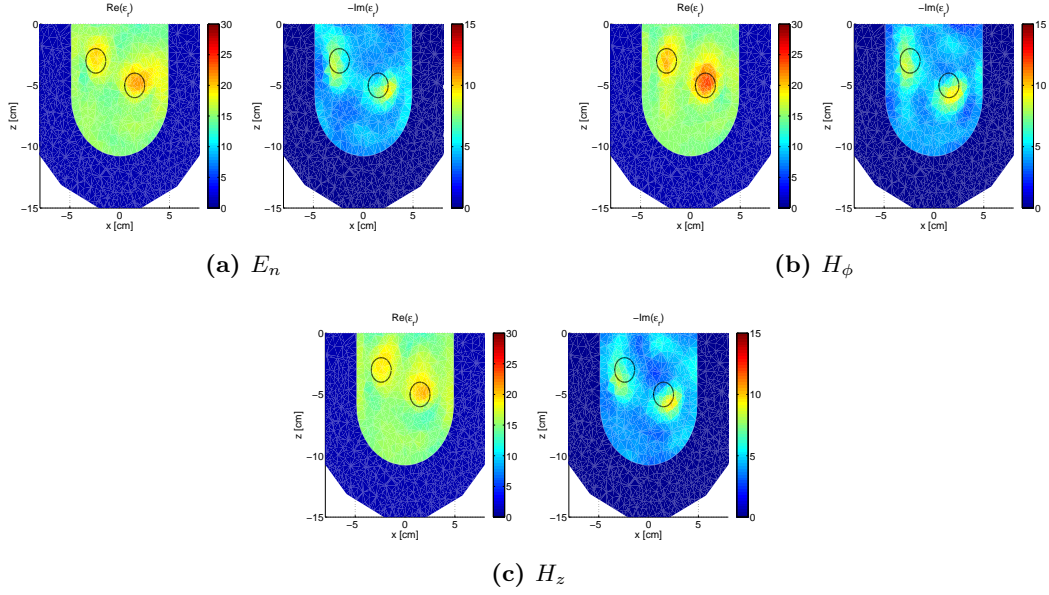


Figure 2.17: Results at 1.3 GHz for a plexiglass chamber top.

metric. Therefore the combined metric (CM) is again the sum of TD and AR .

The selection of τ (the threshold for the binary reconstruction mask) is slightly more involved in this case, as there is prior information involved. A small τ will result in very good tumour detection but a large number of artifacts, whereas as a large τ will reject artifacts very well but have very poor tumour detection. Since the combined metric CM accounts for both TD and AR , it is less sensitive to variation in τ . For these results, $\tau_{f,t}$ is calculated (for real and imaginary separately) as follows:

$$\tau_{f,t} = \frac{2}{3} \left(\max \left\{ \max \{ \varepsilon_{r-f,t, E_n} \}, \max \{ \varepsilon_{r-f,t, H_\phi} \}, \max \{ \varepsilon_{r-f,t, H_z} \} \right\} - \varepsilon_{r-ft/fib} \right) + \varepsilon_{r-ft/fib} \quad (2.4)$$

where $\max \{ \varepsilon_{r-f,t, \vec{U}} \}$ is the maximum (real or imaginary) reconstructed permittivity for a given frequency f , chamber top t , and field component \vec{U} . Essentially, for a given frequency and chamber top, the maximum (real or imaginary) reconstructed permittivity over all the

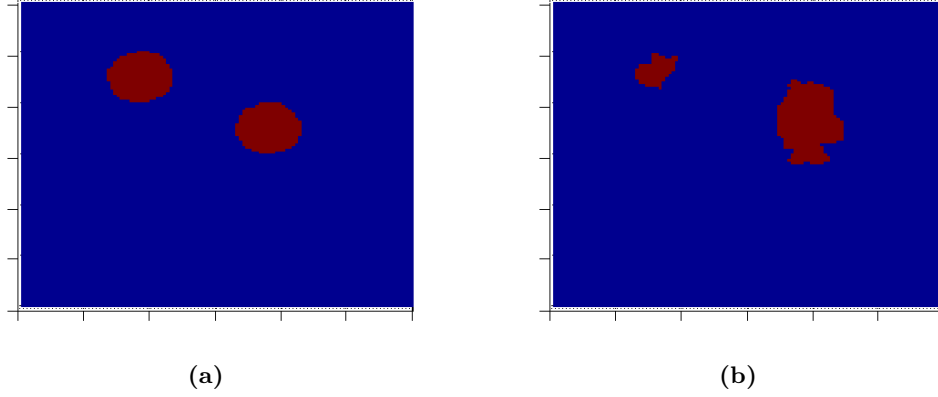


Figure 2.18: Masks for the reconstruction using H_z with the plexiglass top at 1.05 GHz (a) `ref_mask` and (b) `rec_mask`.

field components is found, and the permittivity of the fat/fibroglandular region is subtracted from this maximum. Two-thirds of this difference is taken, and then added back to the permittivity of the fat/fibroglandular region to form τ .

These metrics were calculated for all the reconstructions, and are displayed in Figures 2.19 to 2.22. Which field component is best has some variation across frequency, but overall, the results clearly show that for this chamber, the H_ϕ field component is superior to the other two. This is most readily apparent in the TD metric. The AR metric is often somewhat deceiving for both E_n and H_z (see Figure 2.21 for example), as it achieves a perfect 1 for AR , but has very poor TD . This indicates that effectively no values are detected above τ , leading to no artifacts, but no tumour either, which is a poor reconstruction. This result indicates that these metrics cannot be applied blindly, and some degree of interpretation is required.

From these results, it can be concluded that H_ϕ is the best choice of field component. This result is in agreement with [31]. There is not a dramatic difference between the PEC and plexiglass chamber top scenarios, as at certain frequencies, each top outperforms the other. This is unsurprising, as the closed and open top have different resonant frequencies.

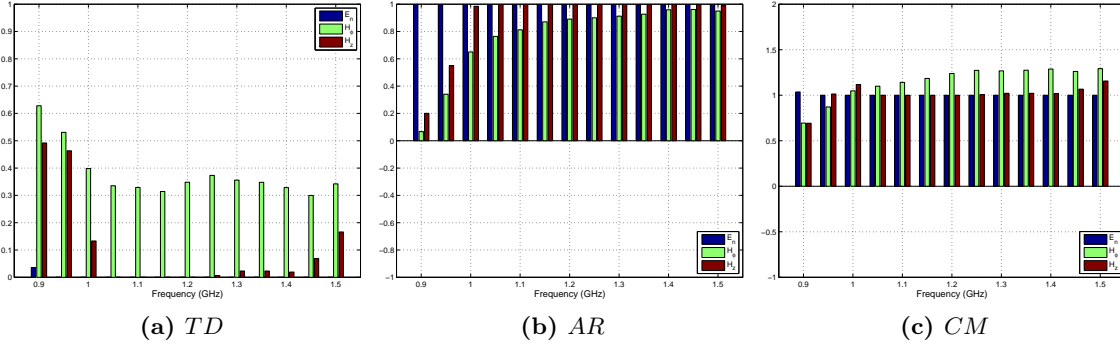


Figure 2.19: Metrics for $Re(\varepsilon_r)$, PEC chamber top.

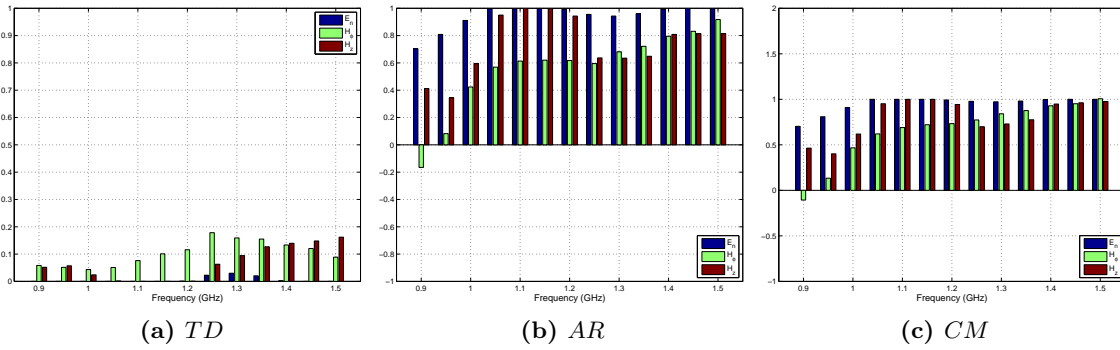


Figure 2.20: Metrics for $Im(\varepsilon_r)$, PEC chamber top.

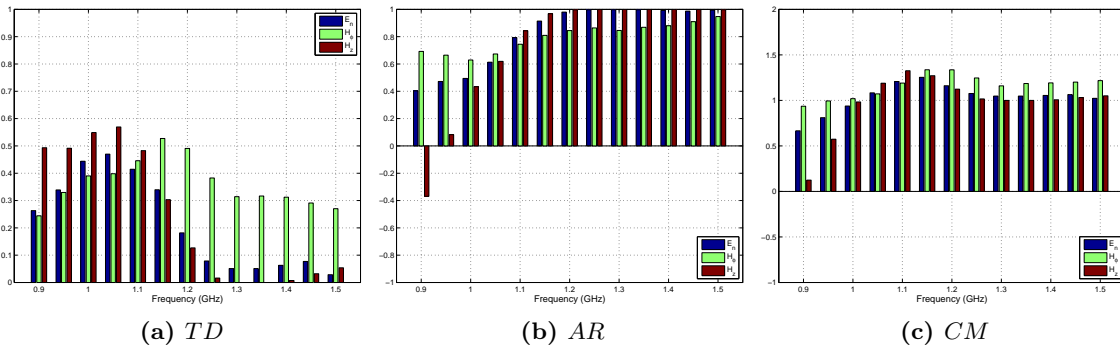


Figure 2.21: Metrics for $Re(\varepsilon_r)$, plexiglass chamber top.

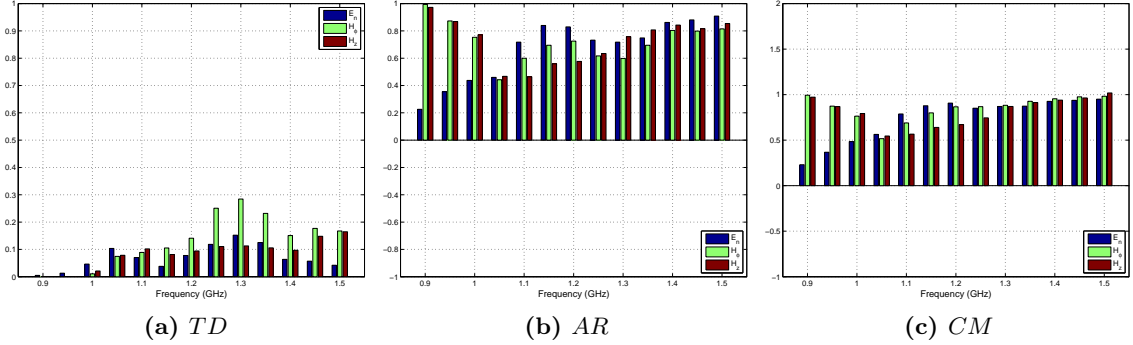


Figure 2.22: Metrics for $Im(\epsilon_r)$, plexiglass chamber top.

2.2.4 A 5 Tissue Region Phantom

A second phantom was used to assess the chamber performance and reconstruction quality differences with a more anatomically realistic phantom. This phantom has 5 tissue regions: skin, fat, fibroglandular, tumour, and muscle, and is pictured in Figure 2.23. Though this phantom is simpler than a human breast, it is much closer to a realistic breast than the two tumour phantom in Section 2.2.1. It was developed in conjunction with the University of Calgary, and is used in [34]. The tissue properties are tabulated in 2.2 [8]. The single spherical tumour has a radius of 0.75 cm. Again, “perfect prior” (pictured in Figure 2.24) was used, meaning that everything except the tumour location is assumed to be known and set as the background permittivity. The chamber top is assigned a PEC boundary condition in this scenario.

In this case, the forward data was inverted on a different mesh with 5% noise added to the data in order to avoid an inverse crime, and each inversion was terminated at 400 iterations. Results inverted at 1.3 GHz are presented here. Additionally, the imaging domain was restricted to the interior of the breast region, *i.e.* the skin, fat, and fibroglandular regions. The reconstructions are shown in Figures 2.25, 2.26, and 2.27. The results are in good agreement with those presented in the previous section. The tumour is visible in both

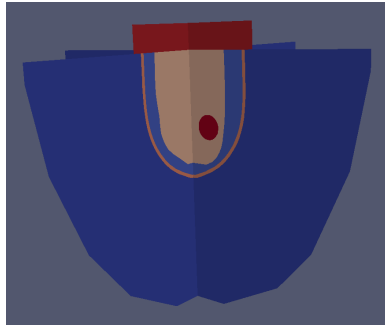


Figure 2.23: Five tissue region phantom.

Table 2.2: Tissue properties of five region phantom.

Material	$Re\{\epsilon_r\}$	$-Im\{\epsilon_r\}$
Background	1	0.001
Skin	43.81	16.11
Fat	4.73	0.78
Fibroglandular	36.41	10.13
Tumour	56.62	17.56
Muscle	55	16

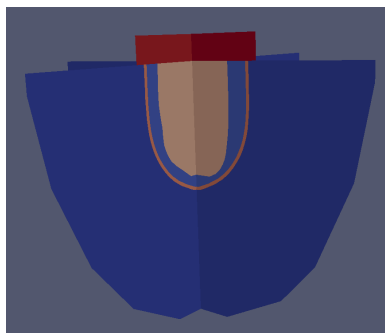


Figure 2.24: Prior information for five tissue region phantom.

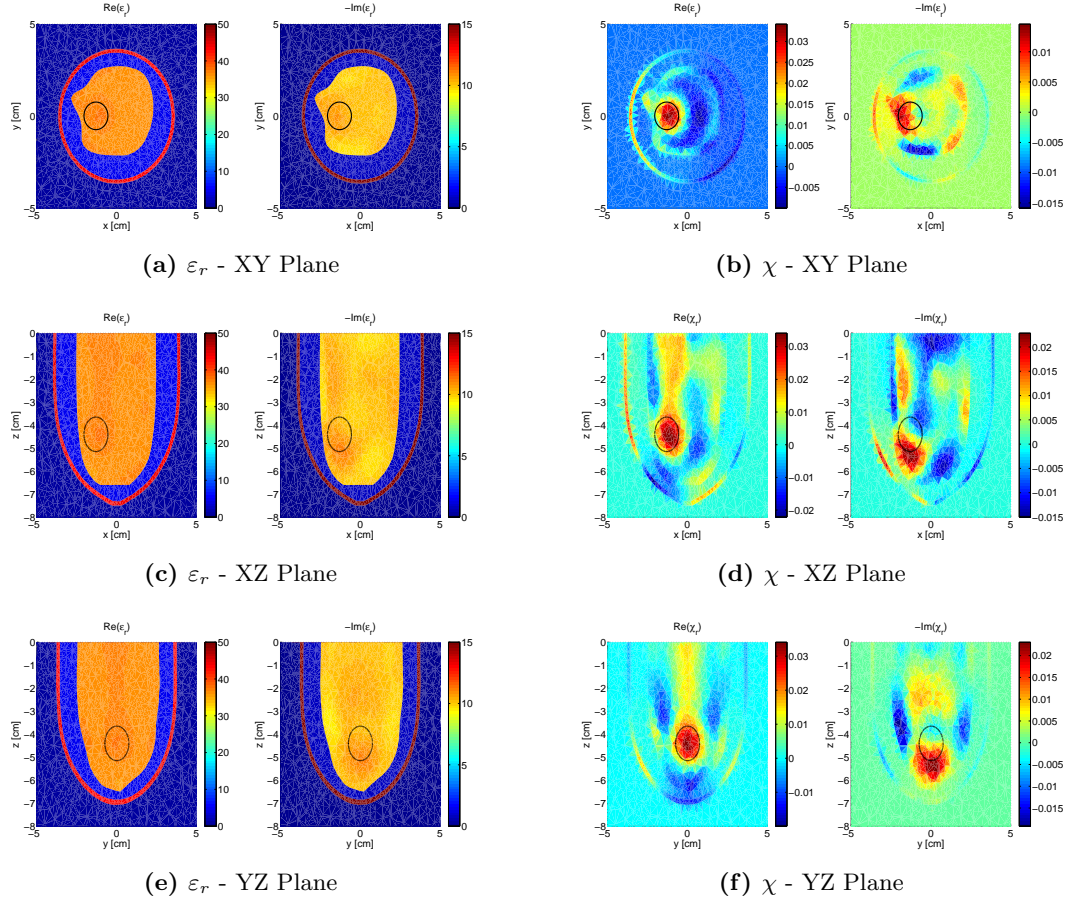


Figure 2.25: Results at 1.3 GHz for E_n .

the real and imaginary parts for all three polarizations, particularly clearly in the contrast (χ) images. Again, the H_ϕ polarization clearly yields the best result.

Based on these results, a decision was made to design the transceivers in the experimental system to be sensitive to H_ϕ polarized fields. These synthetic studies indicate that this choice offers the best results, though this is not an exhaustive investigation. Utilizing both magnetic field polarizations simultaneously can offer improved results, and preliminary work for a dual polarized scenario is documented in Appendix A. However, for the first prototype experimental chamber, pure H_ϕ polarized data was selected.

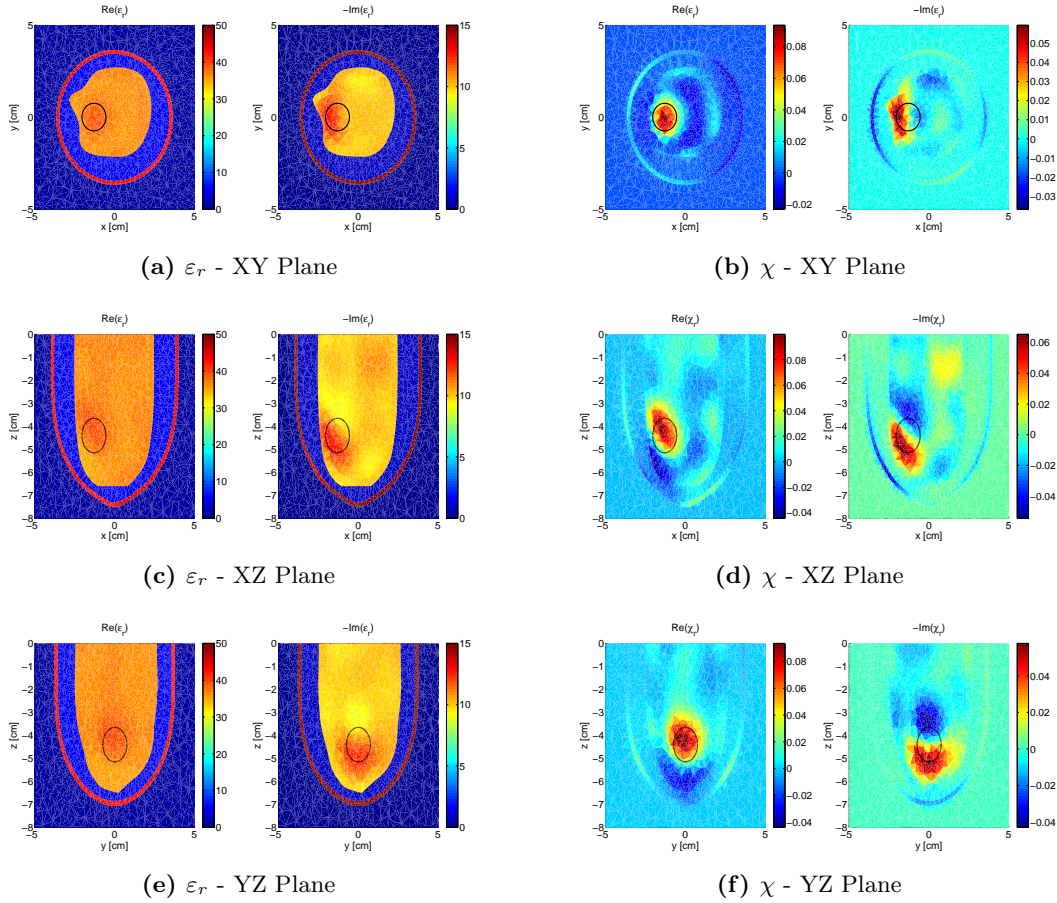


Figure 2.26: Results at 1.3 GHz for H_ϕ .

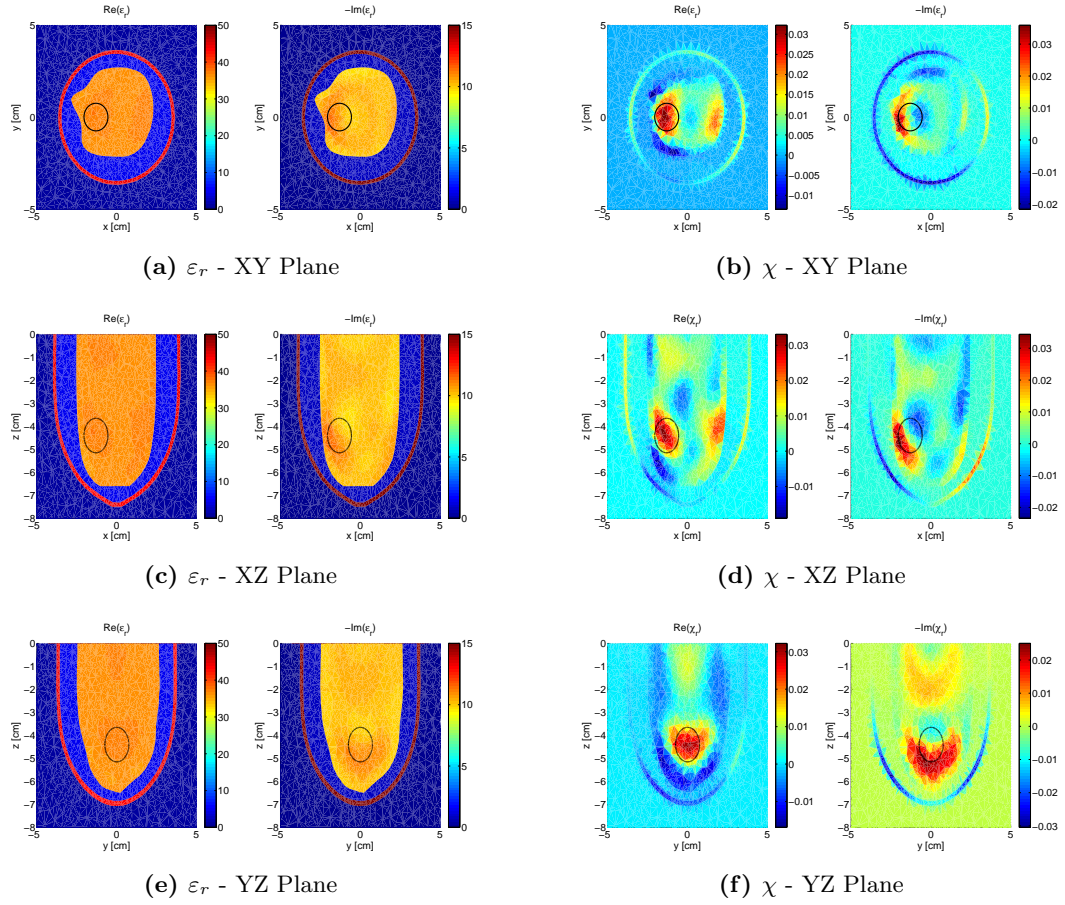


Figure 2.27: Results at 1.3 GHz for H_z .

Chapter 3

Probe Development and Testing

All MWI systems require some form of antenna that radiates and receives electromagnetic fields. Selection of an appropriate antenna is case specific, influenced by a host of factors such as the chamber design, matching medium, desired operating bandwidth, and modeling constraints. Many papers have been published on MWI antenna design that detail the far-field characteristics of the antennas [36, 37, 38]. Though these parameters are very important for many applications, MWI is typically quite different. Namely, in the majority of MWI systems, the OIs (and other antennas) are typically placed in the near-field region of the antenna [39]. In this region, the antenna behaves quite differently than in the far-field region, and therefore other design considerations must be made. Furthermore, when in a PEC-bounded chamber, the antenna acts more like a probe injecting energy into the chamber as opposed to an antenna with an associated radiation pattern.

The majority of MWI systems under development use antennas whose port measurements are directly related to a received electric field, such as monopoles [3], patch antennas [24, 40], and Vivaldi antennas [41]. Practical antenna design for MWI systems is also restricted by the modeling capabilities of forward solver used to compute the equivalent numerical problem. A given design may have very good performance, but if the computa-

tional burden to model the design is too great, the design is impractical. As discussed in Section 1.1.2, the FEM-CSI code used in this work models both electric and magnetic field sources as point sources. Therefore, it is desirable in this work to keep the antenna design simple and easy to approximate with a point source. In theory, a given antenna could be modeled as a sum of point sources [28], however such an investigation is beyond the scope of this work. It is an option for future modeling error reduction.

The following design goals and constraints exist for this novel system:

- Sensitive to H -fields, since synthetic studies indicate magnetic field inversion can yield better results
- Minimal performance change in the presence of other objects, especially mutual coupling with other antennas
- Useable across a bandwidth of 0.8 to 2.5 GHz
- Operate in air very near a PEC surface
- Simple to model

A category for antennas used for measuring fields that are minimally perturbing and simple exists, namely probes. Probe antennas are often used in electromagnetic compatibility (EMC) assessment, since they can accurately and reliably measure fields produced by a device or circuit while having minimal affect on the field of interest. Probes are typically electrically small and relatively inefficient, making them a poor choice in areas such as communications. However, their performance is usually constant over a wide frequency band, making them suitable for broadband measurements. Furthermore, due to the fact that the probes will be incorporated into a quasi-resonant chamber, the efficiency is not measured as a characteristic of a probe on its own, but rather a probe operating within the chamber.

This chapter details the simulation, testing, and selection of a magnetic field probe type

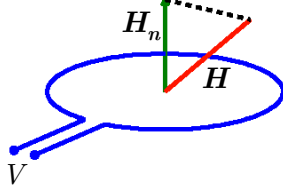


Figure 3.1: Simple loop antenna in the presence of a magnetic field.

antenna for use in the faceted chamber. Henceforth, the antennas developed and used in this work will be referred to as probes.

3.1 Probe Type Selection

The standard probe used for magnetic field measurements is a simple circular loop antenna. Given an electrically small loop antenna like that in Figure 3.1 in the presence of a magnetic field \vec{H} , the voltage V induced across the loop terminals is given by:

$$V = -j\omega\mu H_n A \quad (3.1)$$

where ω is the angular frequency, μ is the permeability of the material in the loop, H_n is the component of the magnetic field \vec{H} normal to the loop area, and A is the area of the loop [42].

The metallic boundary of the chamber under development allows for a simple design modification that reduces the physical loop size. Since the tangential component of the magnetic field at the chamber wall is of interest, by image theory [43], the full loop can be reduced to a half-loop mounted on the chamber wall. As shown in Figure 3.2, by image theory, both antennas produce the same field in the upper half space. The relationship

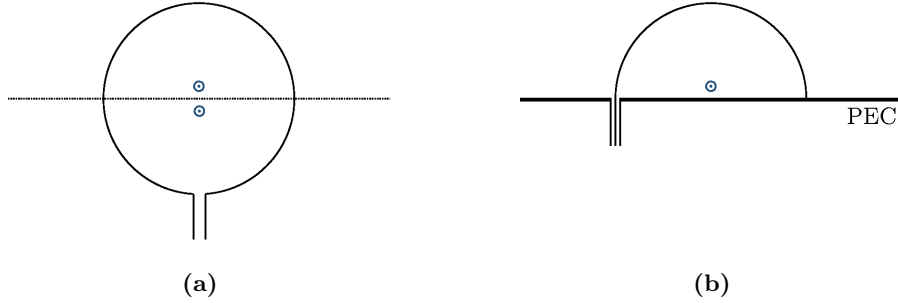


Figure 3.2: Two antennas, (a) a full loop radiating in free space and (b) a half loop radiating above the PEC plane. The blue dot indicates magnetic field coming out of the page.

between the magnetic field produced by a loop and half-loop is analogous to the relationship between a dipole's and monopole's electric field.

A simple loop antenna has drawbacks however. Specifically, a standard loop antenna is somewhat sensitive to electric fields parallel to the plane of loop [44], which is the only component of the electric field present at a PEC boundary. It is important that the probe used be sensitive to only magnetic fields since sensitivity to both introduces ambiguity between a given measurement and the pure magnetic field computed in an equivalent numerical model.

A solution to reducing the electric field sensitivity is a shielded (half-)loop with a top gap. In this implementation, the loop is coaxially shielded except for a small gap at the apex which exposes the center loop conductor [45]. As shown in [44], the shielding makes the probe sensitive to electric fields in the direction of the gap. Since the probe is mounted near a PEC plane, the only electric field component is perpendicular to the gap, and hence the electric field sensitivity of the probe is greatly reduced. Since the gap is centered, any currents introduced by the incident electric field will be common, and rejected by this balanced configuration.

Shielded half-loop probes have been successfully used in MWI systems designed for grain bin monitoring [16]. Prototype shielded half-loop probes have also been constructed

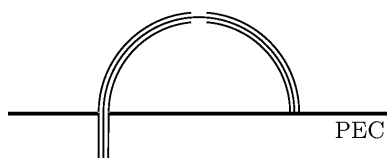


Figure 3.3: Shielded half-loop with a top gap.

from semi-rigid coaxial cable in the EIL for other applications, pictured in Figure 3.4. Note that this design features two ports, as opposed to the single port pictured in Figure 3.3. The two port version offers two distinct advantages: the second connector provides mechanical stability and makes mounting the antenna simple, and it allows for different loads to be attached to the second port. The antenna is fed from one of the ports, and a short-circuit, open-circuit, capacitive, or resistive load can be attached to the second one. The impact of different load conditions is discussed in greater detail in Section 4.2. While it is relatively simple to make a small number of shielded half-loops from coaxial cable, constructing a larger number of probes by hand is time consuming and prone to inaccurate placement of the top gap. Furthermore, cutting the gap in the outer shielding weakens the mechanical strength of the probe.

The clear alternative to coaxial construction is to realize the probes on a printed circuit board (PCB). Many types of PCB microwave transmission lines exist, such as microstrip, co-planar waveguide (CPW) and stripline. All of these can be cheaply mass produced with high precision and good mechanical stability. Furthermore, a PCB implementation also opens up the possibility of including small circuit components on the probe. More details on potentially useful circuits are given in Subsection 3.3.



Figure 3.4: Prototype shielded half-loop with a top gap constructed from semi-rigid coaxial cable.

3.2 Design of Four Prototype Printed Circuit H -Field Probes

The selection of a shielded half-loop with a top gap as a suitable probe satisfies the aforementioned goals; they are sensitive to H -fields, minimally perturbing to the fields, able to operate close to a PEC surface, and are simple to model. The next goals of bandwidth, operating medium (air) and physical size constraints are now addressed.

3.2.1 Design Geometry Considerations

The first constraint to consider is the maximum physical dimension that the probes can occupy. The center-point of each panel in the faceted chamber introduced in Section 2.1 is approximately 4 cm along an elliptical arc away from each of its neighbouring panel's center-points. Therefore, the distance between the two probe ports must be somewhat less than 4 cm so probes can fit on neighbouring panels. From a performance perspective, it is clear from Equation 3.1 that increasing the loop area increases the sensitivity of the antenna. However, when the probe becomes too large, it ceases to be electrically small and exhibit probe behaviour. Given these constraints, and noting the existence of the coaxial probes in the EIL with a port separation of 2.5 cm, the probes developed here were chosen to have a port separation of 2.5 cm.

Table 3.1: Transmission line parameters.

	H	T	W	S	ϵ_r
Microstrip	1.78mm	0.036mm	3.3mm	N/A	4.4
Stripline	1.78mm	0.036mm	1.5mm	N/A	4.4
CPW	1.78mm	0.036mm	1.27mm	0.2	4.4
Grounded CPW	1.78mm	0.036mm	1.37mm	0.2	4.4

Next, the design geometry was altered from a circular half-loop to a square half-loop. This change allows for future modification of loop area by varying the height of the loop (and therefore the area) without modifying the port separation. Preliminary study of the impact of height and length on the performance of a rectangular half-loop has been documented here [31].

3.2.2 Microwave Transmission Line Parameters & Simulation

As previously stated, there are many types of microwave transmission lines that can be implemented on a PCB. Four types were specifically examined in this work: microstrip, stripline, CPW, and grounded CPW. These topologies are pictured in Figure 3.5. The parameters noted in each of the figures (T, W, H, S) must be chosen, along with the substrate's permittivity, so that the transmission line has an impedance of 50Ω . The impedance of each type of transmission line is governed by a different equation, and several online calculators exist [46, 47, 48, 49] for determining the appropriate dimensions to obtain the desired impedance. Table 3.1 lists the parameters chosen for each transmission line type. Each transmission line type of square half-loop was simulated using ANSYS[®] HFSS, Release 15.0 without the top gap to ensure that the tabled calculations resulted in an effective transmission line. Two sample loops are pictured in Figure 3.6 and the simulated S_{11} parameter of each line is shown in Figure 3.7. The results show that the loop is acting like a well-matched transmission line.

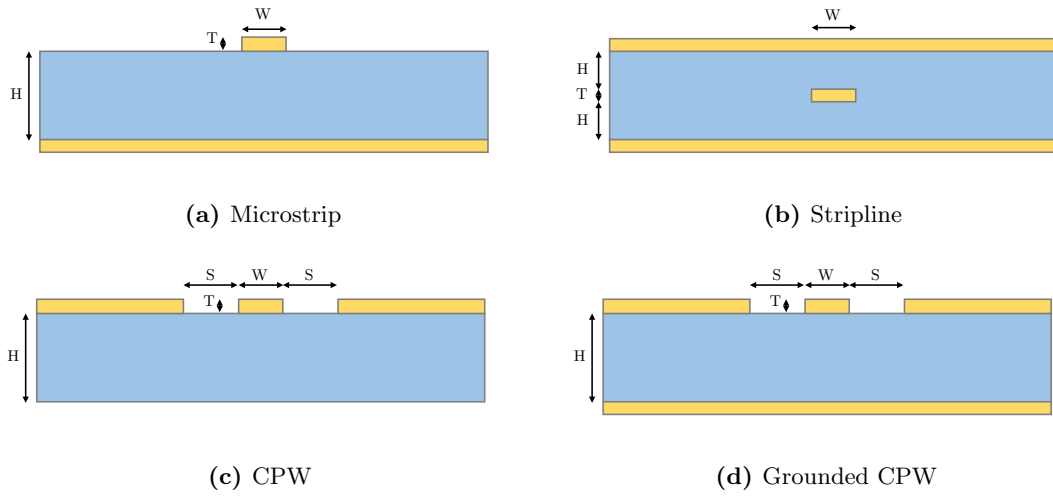


Figure 3.5: Microwave transmission line topologies.

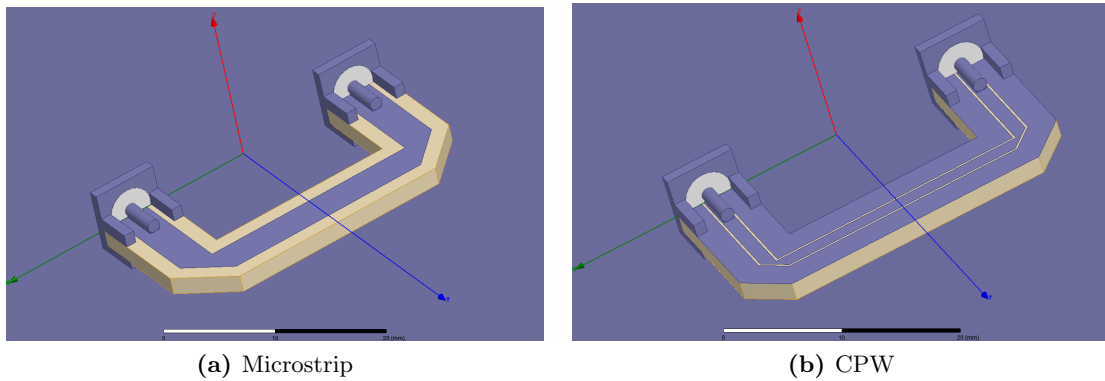


Figure 3.6: Half-loop transmission lines in HFSS.

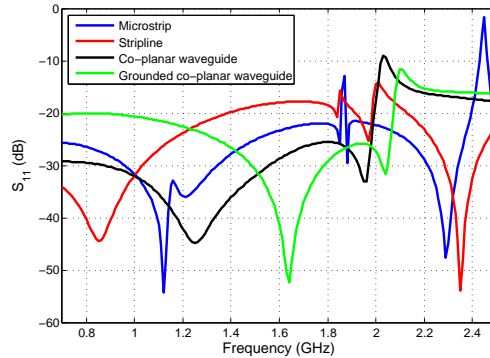


Figure 3.7: Performance of half-loop transmission lines in HFSS.

3.2.3 Testing of Prototypes in GTEM Cell

A key performance requirement of the H -field probe is the rejection of electric fields. In order to determine which type of transmission line featured the best electric field rejection, prototype half-loops (pictured in Figure 3.8) were fabricated with a 1 mm top gap cut in the ground traces for each respective topology.

A Gigahertz Transverse Electromagnetic (GTEM) cell was used to test the sensitivity of each probe to electric and magnetic fields. GTEM cells are a type of test chamber (often used in electromagnetic emissions testing) consisting of a pyramidal shielded chamber boundary, a center plate (septum), radiation absorbent material (RAM), a tray of resistors at the end of the septum, and a coaxial cable port at the pyramid apex. The septum is connected to the center conductor of the coaxial cable, the shielding of the coaxial cable is connected to the shielding walls of the cell, the RAM at the base of the cell act as a matched high frequency load termination, and finally the resistor tray acts as a low-frequency matched load. This geometry sets up a well characterized transverse electromagnetic (TEM) field into which devices and antennas can be introduced, shown in Figure 3.9.

The test setup involved mounting the probe under test on the floor of the GTEM cell and connecting one port of a VNA to the coaxial GTEM cell feed port and the other VNA

port to one of the probe terminals. In this setup, the floor of the GTEM cell acts as the ground plane for the half-loop, and the S_{21} measurement from the VNA is the probe's received signal from the TEM field in the cell. Two orthogonal loop orientations are used in the testing. When the half-loop is facing the apex of the cell, the magnetic field inside the cell is parallel to, and does not pass through, the plane of the loop. This orientation is minimally sensitive to the magnetic field since no component of the field is parallel with the loop plane normal. Therefore, any received signal in this orientation is due to undesired electric field sensitivity. In the orthogonal orientation, the normal of the the loop plane is completely parallel to the magnetic field, and therefore this orientation has maximum magnetic field sensitivity. It is important to note that this orientation has the same electric field sensitivity as the first orientation, so a measurement taken under this condition is related to the magnetic field and parasitic electric field sensitivity.

For each probe and orientation, two different loads were connected to the second port of the probe: and open circuit (OC) and short circuit (SC). Changing the load impedance at the second terminal alters the probe response, and it is of interest to determine if one loading condition yields better performance. The results of these tests are shown in Figure 3.10. As expected, for all the prototypes, the received field is greater in the maximum magnetic field orientation of most frequencies for both loading conditions. The OC load has flatter performance across the bandwidth while the SC introduces peak sensitivity between 1.3 GHz and 1.5 GHz. Conclusions on ideal loading conditions cannot be made at this time, since the resonant frequencies of the the faceted chamber will play a role in their final performance. The in-chamber load analysis is examined in Section 4.2.

It is clear from Figure 3.10d that the microstrip probe has the worst electric field rejections. This makes intuitive sense, since the microstrip transmission line is the least shielded by the ground trace. Electric field rejection is quite similar for the other three prototypes, with the stripline probe having the best performance across the entire frequency band of

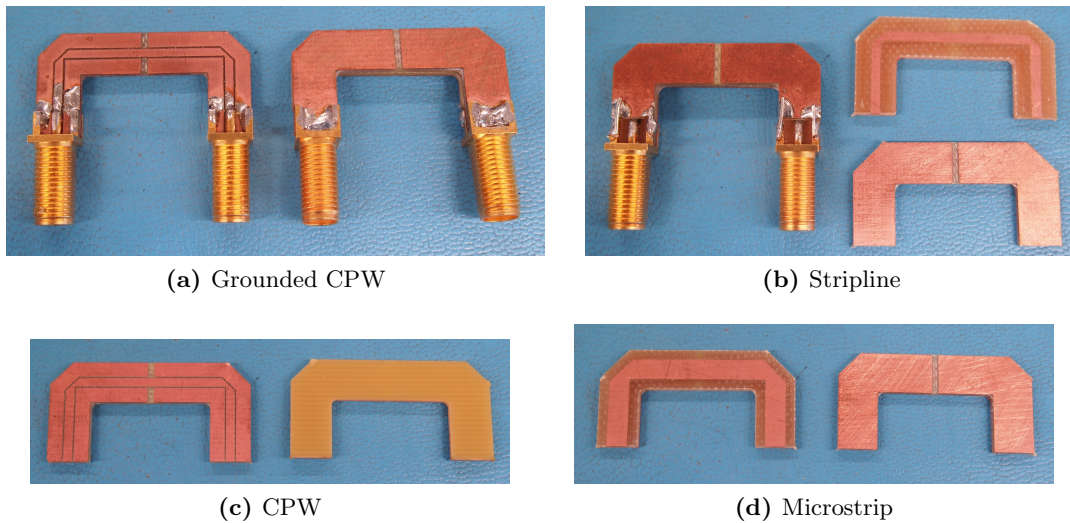


Figure 3.8: Prototype probes.

interest. However, the stripline probe has significant practical disadvantages. True stripline implementation requires expensive 3 layer PCBs, and the stripline SMA connectors are often bulky and prohibitively expensive. For this reason, as seen in Figure 3.8b, the prototype was realized by sandwiching two separate 2 layer PCBs and using a standard 2 layer SMA connector. While this change reduces cost, it is significantly more difficult to assemble precisely. Furthermore, the shielding of both the grounded CPW and stripline probes can be improved by adding vias between the top and bottom ground planes. However, the dual PCB implementation of the stripline topology cannot have connected vias without significant manual labour. For these reasons, despite its somewhat better performance, the stripline implementation is not pursued further.

This leaves CPW and grounded CPW as the two viable options for the final design. Figures 3.10a and 3.10c indicate that their performance is quite similar. However, since grounded CPW has a bottom layer ground plane, vias can be added to this design, further improving shielding. For this reason the grounded CPW probe was chosen as most ideal prototype.

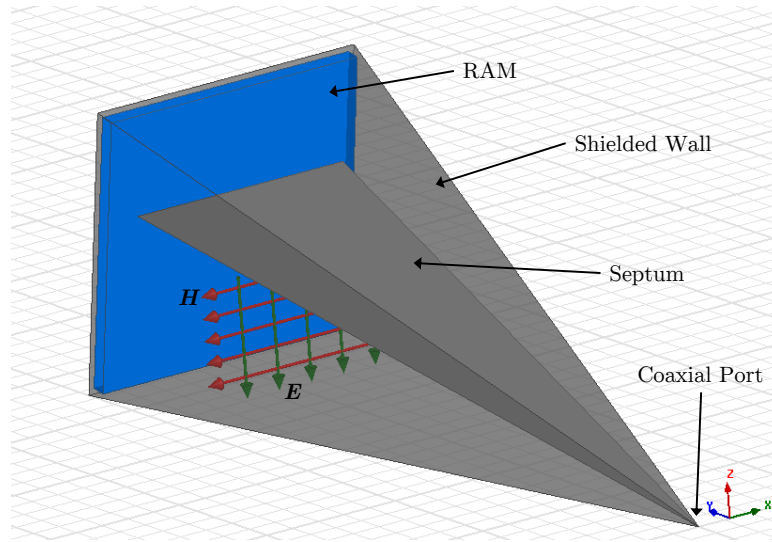


Figure 3.9: GTEM cell.

3.3 Refinement of a Grounded CPW H -Field Probe

The grounded CPW design was refined in order to improve performance. The first modification was the addition of vias between the top and bottom ground layers to ensure that both layers were at the same RF potential. As mentioned previously, using a PCB for the probe implementation allows the incorporation of circuit elements on the probes. As discussed in [31], such half loops can be made into reconfigurable probes, where the radiating properties can be changed by the inclusion of switching elements such as diodes.

In this application, an RF PIN diode soldered across the top gap with no bias voltage applied is effectively electrically invisible, and has minimal impact on the probe. However, applying a DC bias voltage across the diode allows RF currents to pass through the diode, providing a short circuit across the gap, fully shielding the inner conductor and preventing radiation. Any received fields in this state would be due to parasitic components not directly related to the magnetic field passing through the loop. Taking a measurement from the probe under both diode states (not biased and forward biased) and subtracting the

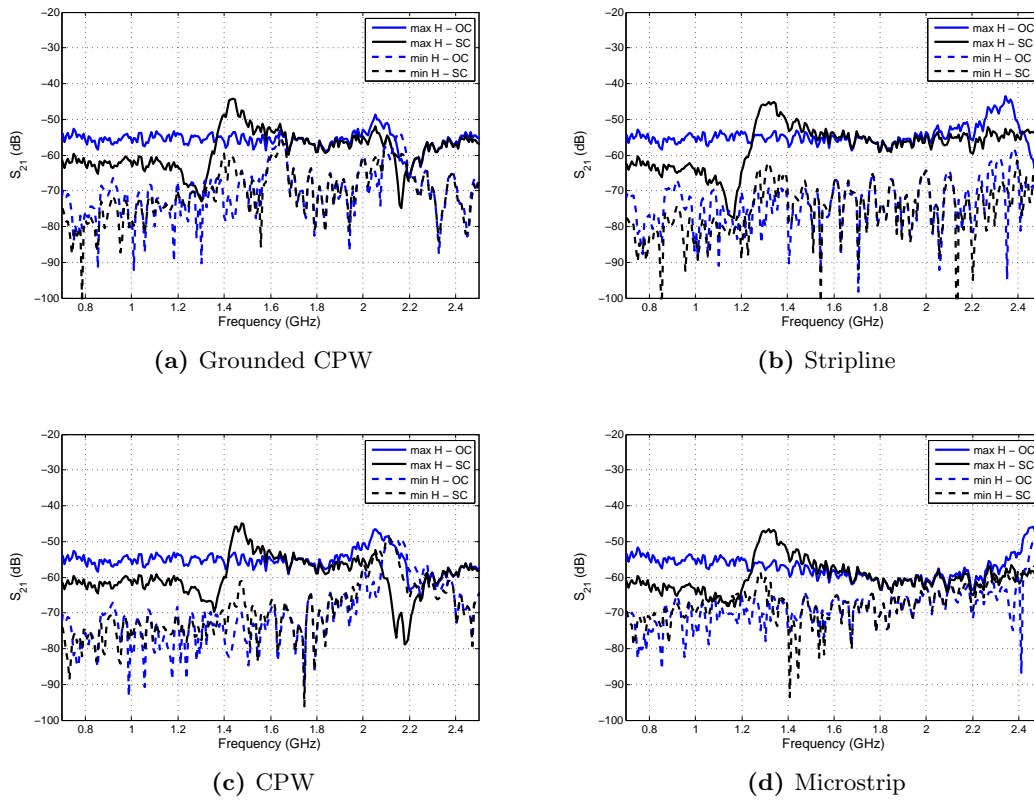


Figure 3.10: Probe performance in GTEM cell. Measurements were taken in both orientations and with OC and SC load conditions.

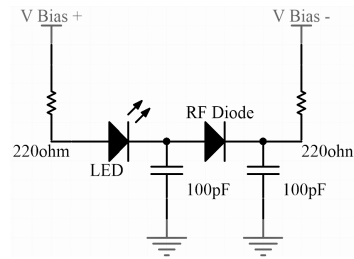


Figure 3.11: Diode biasing circuit.

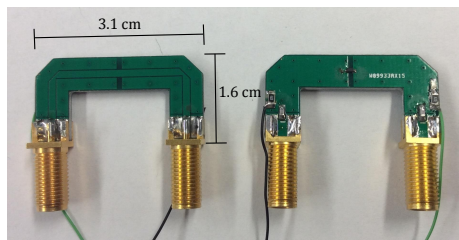


Figure 3.12: Final probe design with vias and diode circuitry.

forward biased state from the biased state could remove parasitic contributions from the not biased measurement, improving accuracy.

In order to test this theory, the probe design was modified to include a simple circuit consisting of resistors, capacitors, an LED, and a diode, pictured in Figure 3.11. The resistors limit the current passing through the diode, the LED is simply a visual indicator of the diode state, the RF PIN diode acts as the shorting element, and the capacitors short any RF signal picked up by the circuit traces to RF ground. The fabricated and assembled revised probes are pictured in Figure 3.12. The thin wire leads can pass through the metal surface the probe is mounted on alongside the SMA connectors allowing for control of diode state without having extra cabling inside the eventual imaging chamber.

The final probe design was tested inside a GTEM cell in a similar manner to the testing described in Section 3.2. A probe was placed in the cell in two different orientations (maximum and minimum magnetic field sensitivity) under the two (OC and SC) loading

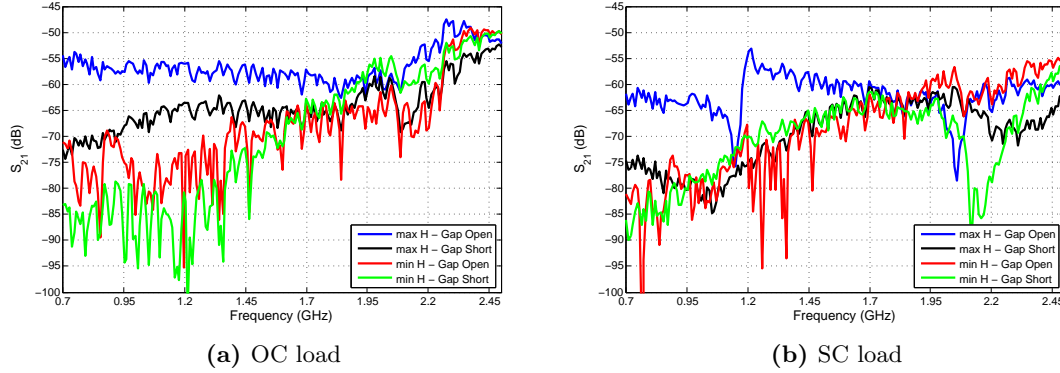


Figure 3.13: Probe performance in GTEM cell.

conditions. Additionally, for these probes, for each orientation and load, two measurements were taken, one with the gap open (diode not biased) and one with the gap shorted (diode forward biased). The resulting S_{21} measurements are displayed in 3.13. The new probe performance in the gap open states is quite similar to the old probe design (without the diode, see Figure 3.10a), with some improvement at the high end of the frequency range particularly for the OC load. As expected, shorting the top gap significantly reduces the received signal strength in the maximum magnetic field orientation at most frequencies. The shorting process is of most interest for the SC load between 1.2 GHz and 1.45 GHz. In this instance, the shorted gap results in a similar measurement in both orientations. Subtracting the shorted gap state from the open gap state has the greatest potential for parasitic field component removal in this instance. The impact of this delta measurement is examined in greater detail in Section 4.2.

It is also important that the presence of adjacent probes inside the chamber does not perturb the field received by the selected probe. To determine the impact of a nearby probe, two probes were placed side by side in the GTEM cell separated by 4.5 cm, as pictured in Figure 3.14. In this test setup, S_{21} was still measured between the GTEM apex and the port of a single probe (terminated with a SC load). The adjacent probe had a SC load on

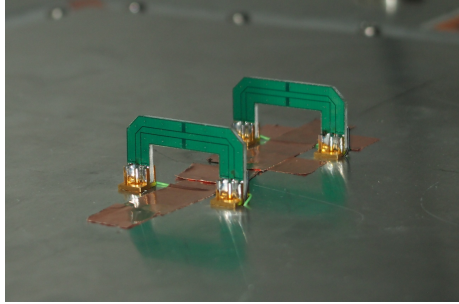


Figure 3.14: Two adjacent probes under test.

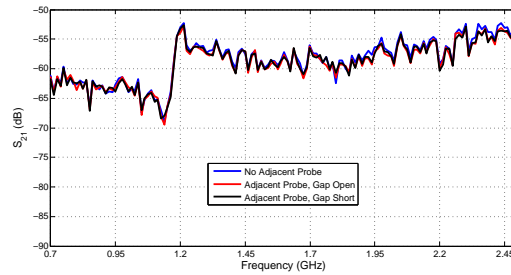


Figure 3.15: Impact on S_{21} between GTEM apex and probe of adjacent probe.

one terminal and a broadband 50Ω load on the other terminal which replicates the eventual in chamber situation where adjacent probes are connected to a matched load through the RF switch network. Figure 3.15 shows that the effect of the adjacent probe is very minimal. There is a negligible difference in the received field when the adjacent probe (in both gap states) is introduced, indicating that the probes minimally perturb the received field.

This concludes the development and the out of chamber testing of the magnetic field probes for use in the faceted imaging chamber. The selected grounded CPW shielded half-loop with a top gap meets the stated design goals: it is sensitive primarily to magnetic fields, minimally sensitive to adjacent probes, useable across the desired bandwidth and operates effectively in air at a PEC surface. The performance of this design in an imaging chamber is discussed in the next chapter.

Chapter 4

Modeling Error and Calibration Techniques in Fabricated Faceted Chamber

No matter how much care is taken in system and antenna/probe design, modeling error will always be present between the experimental system and the corresponding numerical model. Some form of calibration of the collected data is also necessary in order for the data to be inverted. This chapter introduces the fabricated faceted chamber with the probes developed in Chapter 3. In this chapter, analysis of modeling error for incident and scattered fields for simple objects is conducted for a variety of probe load conditions and calibration techniques. An optimal data collection and calibration scheme is selected and inversions of measured data for a simple cylindrical object are shown and analyzed. This work lays the foundation for imaging of more complicated targets.

4.1 Chamber Fabrication and Initial Testing

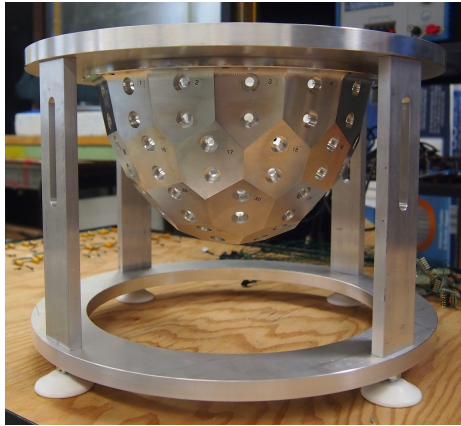
A full 3D computer model of the faceted chamber (introduced in Section 2.1) and supporting parts was created in software and was subsequently manufactured in the U of M's Electrical and Computer Engineering Machining Shop. The chamber was machined with a CNC milling machine out of aluminum, a metal chosen for its light weight and ease of machining. Two mounting holes were drilled in each facet to allow mounting of the probes, and two top plates (one made from plexiglass, the other aluminum) were fabricated to allow for simple and accurate positioning of breast phantoms. All the fabricated chamber components are pictured in Figure 4.1.

Upon assembly of the chamber, 24 magnetic field probes were mounted in the chamber on the 24 facets selected (out of 44 total) in Section 2.1. The remaining 20 sets of holes were covered in copper shielding tape to ensure a continuous metallic surface. As noted in Section 3.3, the diode biasing wires pass through the mounting holes to the chamber exterior, and therefore do not disturb fields inside the chamber, which is a distinct advantage over systems such as those described in [41]. The fully assembled system is pictured in Figure 4.2.

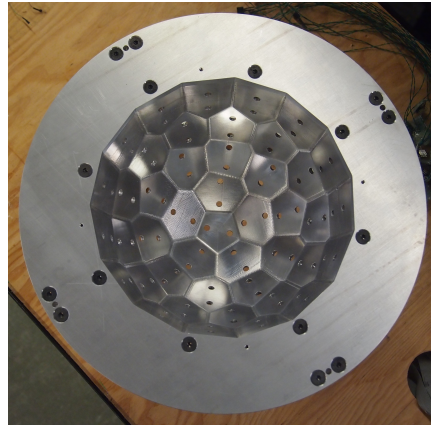
4.1.1 System Description

The assembled system was then connected to the EIL's data acquisition system as indicated in Figure 4.3. A PC running EIL-developed software controls the data acquisition process. Communication with the VNA and RF switch is done over GPIB (General Purpose Interface Bus), a standard communications bus for laboratory equipment. The RF switch is a 2-to-24 mechanical switch matrix, allowing for either VNA port to be connected to any of the 24 output ports. SMA cables connect each of the 24 ports to the input port of the probes.

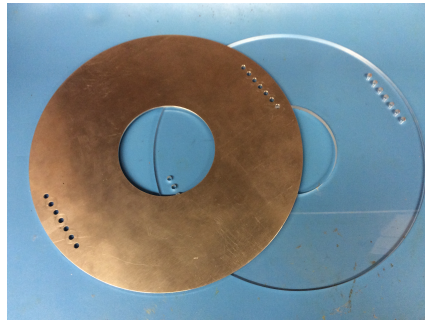
The probe driver circuit (PDC) is a custom designed mixed signal circuit that controls the bias voltage across the diodes on each of the 24 probes. The PC communicates over



(a) Chamber Side View

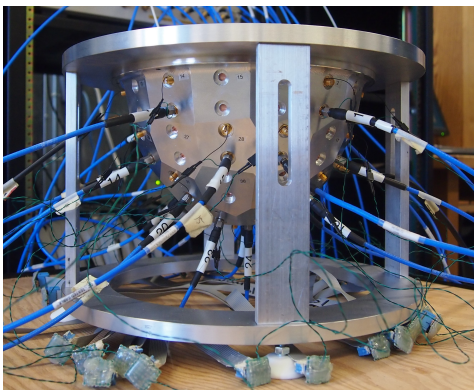


(b) Chamber Top View

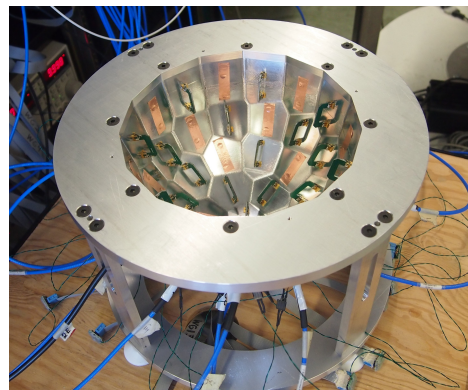


(c) Top Plates

Figure 4.1: Fabricated faceted chamber.



(a) Chamber Side View



(b) Chamber Top View

Figure 4.2: Fabricated faceted chamber with probes.

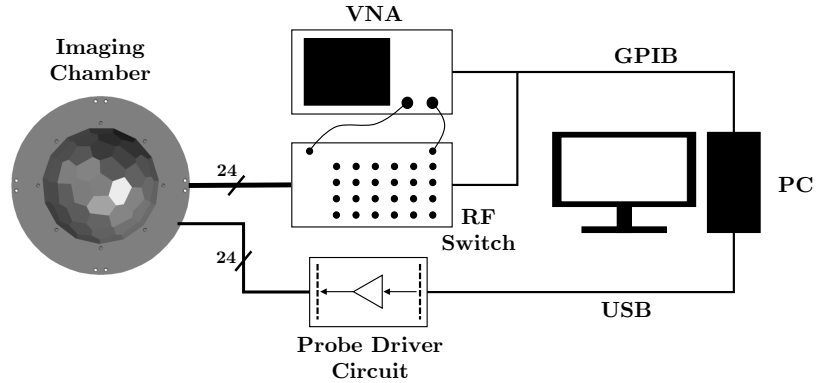


Figure 4.3: EIL MWI system block diagram.

USB with a National Instruments GPIO card that interfaces with the PDC. The PDC takes the input communication from the GPIO card, and through a reprogrammable logic circuit, sets the proper voltages on the diode control lines.

Data acquisition time is dependent on a number of factors including the number of antennas, number of frequencies, IF bandwidth, number of averaging points. A typical measurement takes less than 5 minutes. Using the PDC increases the acquisition time significantly (6 times longer), since the circuit was designed for use with the system described in [50] and the control software has not been optimized to take advantage of the less intensive requirements of the faceted chamber probes. Optimizing the control software would result measurements with the PDC incorporated taking twice as long as those without the PDC. This is because for every probe combination, a gap open and gap shorted measurement must be taken, as opposed to simply a gap open measurement. The PDC switching time is negligible.

4.1.2 Co-Resident Probe Introduction

As discussed in Section 3.3, probes that minimally perturb the fields in the chamber are desirable since they do not have to be incorporated in the numerical model. Though

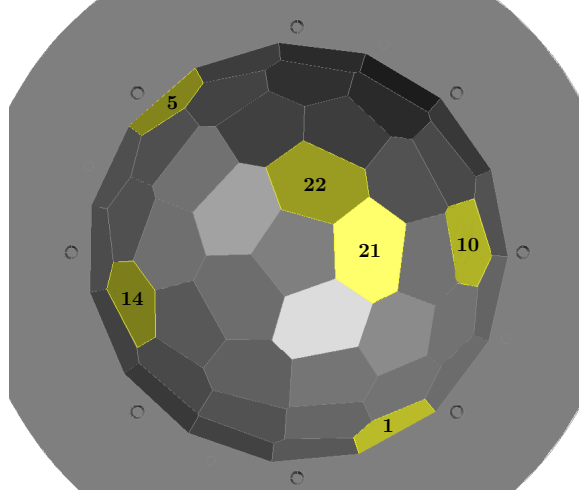


Figure 4.4: Probe locations and corresponding numbers for co-residence testing.

the probes designed for this system were already shown to be minimally perturbing in a GTEM cell, the following testing was done during chamber assembly in order to verify this result in the chamber.

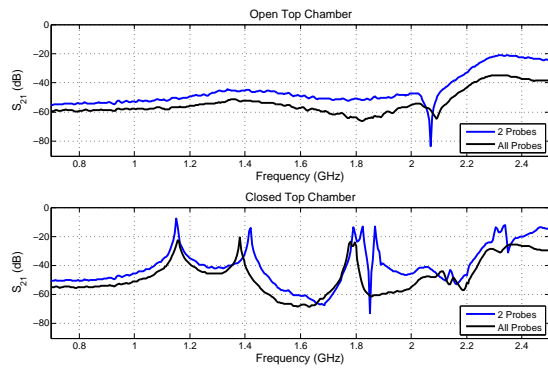
Prior to the installation of all the probes, two probes at a time were mounted in the chamber at selected facets, shown in Figure 4.4. The VNA (through the switch) was connected to the two mounted probes and two S_{21} measurements were taken for the pair, one measurement with an open chamber top and one with a metal sheet covering the chamber top (closed top). This process was repeated for several combinations of two probes. These measurements correspond to the ideal scenario wherein there are no other probes present in the chamber except for the current transmit/receive pair.

Once all the probes were mounted in the chamber, S_{21} measurements were taken for the same transmit/receive pairs to obtain data for the realistic scenario where all the probes are always present in the chamber. The resulting data is compared in Figure 4.5, where the transmit/receiver numbers correspond to the numbered panels highlighted in Figure 4.4. There are several patterns in the data of particular interest. Firstly, the change in measured S_{21} is similar for all of the transmit/receive pairs, indicating that the physical

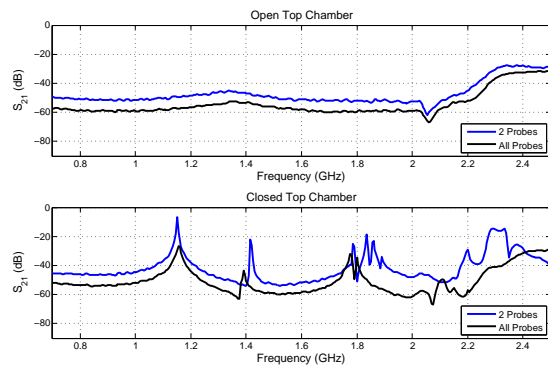
proximity of the two probes in a pair is not a factor. For example, the transmit 21/receive 22 probes are very near each other, while the transmit 1/receive 5 probes are on opposite sides of the chamber. Independent of proximity, in all cases the measured amplitude in the “all probes” case is 5-10 *dB* lower than “2 probes” case. This is explained by the fact that the 22 probes not selected in the transmit/receive pair are still connected to the RF switch and terminated in matched 50Ω loads. In the “2 probes” case, the power radiated by the transmit probe is reflected by the metal walls (save some ohmic loss), and the only sources of loss are the power dissipation in the load connected to the receive antenna and power escaping the top of the chamber in the open top scenario. Conversely, when all the probes are present, even when they are not selected as receivers, the radiated field still induces a current in the probe’s center conductor which travels down the attached RF cable to the resistive load inside the switch. This is an additional source of loss in, hence the lower received amplitude by the selected receiver.

Of particular interest in the open top measurement scenarios is the fact that for both the “2 probe” and “all probe” the trends in S_{21} over frequency are very similar. If the co-resident probes were perturbing the fields significantly, we would expect the measured fields for the two scenarios to have different trends over frequency. There is some variation in the trends, particularly in 4.5a between 1.7 and 2.1 GHz. However, the difference between the “2 probe” and “all probe” scenarios is primarily a shift in amplitude and not a different trend over frequency, indicating that the presence of the co-resident probes primarily introduces loss and any perturbation of the radiated fields is minimal.

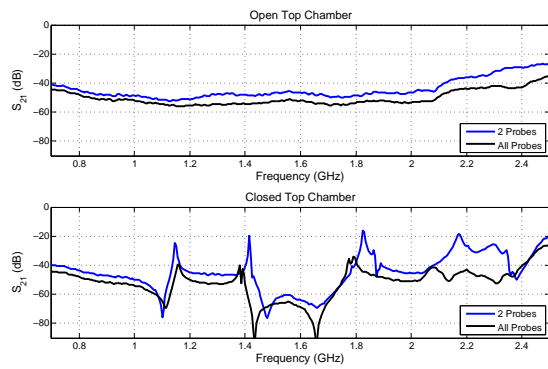
Similar conclusions can be drawn about the closed top (metal plate covering the chamber top) measurement scenario with some differences since the metal top makes the chamber highly resonant. This resonant behaviour is clearly identifiable by the many sharp peaks across the frequency spectrum. As in the open top scenario, at most frequencies, there is a decrease in amplitude of 5-10 *dB*. However, the resonant peaks do shift in frequency which



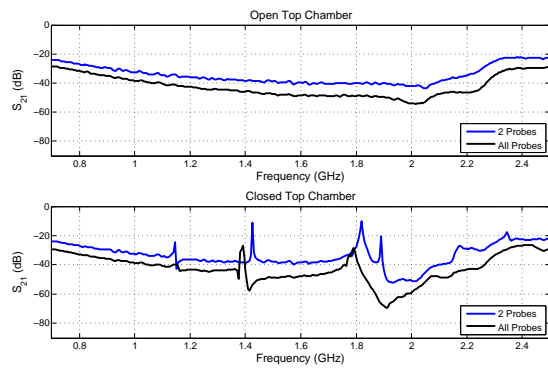
(a) Transmitter 1, Receiver 5



(b) Transmitter 1, Receiver 14



(c) Transmitter 10, Receiver 21



(d) Transmitter 21, Receiver 22

Figure 4.5: Comparison of measured S_{21} with 2 probes and with all probes in the chamber for 4 different probe pairs.

is characteristic of the perturbation of a resonant cavity [51]. This indicates that the losses and other probes are changing the resonant modes of the cavity. Additionally, for all the transmit/receive pairs, at frequencies around 2-2.5 GHz, there is a much more dramatic difference between the “2 probe” and “all probe” scenarios. This is expected since at higher frequencies, the probes are larger with respect to wavelength and therefore have more of a perturbing affect. All of these observations indicate that with the closed top, the chamber is highly resonant and the co-resident probes have a non-negligible impact on the modes excited in the chamber.

The perturbation of the resonant cavity by the co-resident probes increases modeling error for the closed top chamber. There are several ways to decrease modeling error when imaging in resonant cavities. From a system standpoint, intentionally introducing loss to the chamber dampens the resonant modes making the cavity less sensitive to further perturbation. In the EIL, this approach was taken during arm imaging studies by mixing salt into a water background [52]. In the faceted chamber, the background medium is air, so a distributed loss like salt in water is not realizable. Instead, loss could be added by placing some object such as a piece of radar absorber or a small container of salt water. These added lossy objects would need to be accurately modeled for this approach to be effective. Alternatively, from a modeling standpoint, small lossy elements could be added to the numerical model at the probe locations. These elements would need to be selected so that the loss they introduce is similar to the loss due to the power dissipation through the inactive probes. Currently, the EIL’s forward solver cannot incorporate lumped circuit elements. If the code was modified, 50Ω resistive elements could be placed in the model, which would reduce modeling error. These techniques are all viable, but are not addressed further in this work. For this reason, the metal top measurement scenario is not examined further, and is left for future work. All measurements presented from here on are taken with either an open air or plexiglass chamber top.

4.2 Modeling Error Analysis of Measured Data

As has been discussed already, reducing modeling error between the experimental system and the numerical model is very important if accurate reconstructions are to be expected. This section examines several different system configurations and data collection techniques, and the measurements are compared to synthetic data in order to determine the optimal data collection scheme. Calibration methods are also described and tested.

Loading the second port of the magnetic field probes with a SC or OC load was introduced in Section 3.2.3. In this section, another loading condition, a tuned capacitive (TC) load is examined. This condition is realized by attaching a variable capacitor to the second port of the probe (pictured in Figure 4.6) and adjusting it so that the probe is sensitive at particular frequency. In the following tests, all the antennas were tuned to have maximum sensitivity at 1 GHz. A plot of S_{11} for a single probe under the three loading conditions is shown in Figure 4.7.

The other measurement technique employed is the use of the RF diode on each probe. Here the “direct” measurement technique means that a single measurement is taken between a transmit/receive probe pair where the diodes on each probe are left unbiased, and therefore have negligible impact on the measurement. The “delta” measurement technique means that two measurements are taken for each transmit/receiver probe pair. In both measurements the transmit probe has an unbiased diode, while the receive diode is unbiased for one measurement and then forward biased for the second measurement. These two data values are then subtracted (diode off - diode on) to yield a single “delta” value.

The three load conditions and two measurement techniques make for six different possible datasets for any given OI in the chamber.

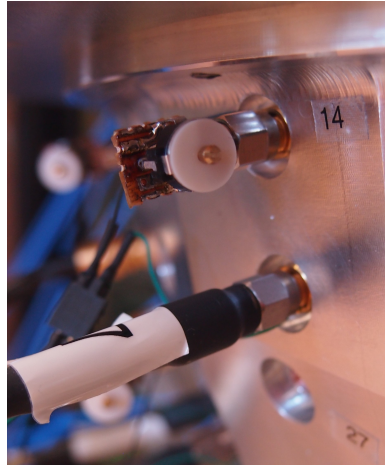


Figure 4.6: Variable capacitor attached to second port of a probe.

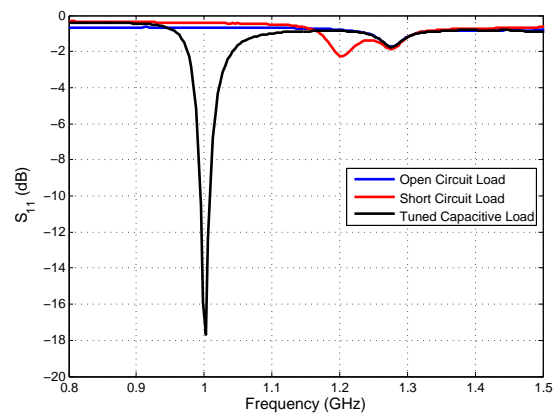


Figure 4.7: S_{11} for antenna under different loading conditions.

4.2.1 Incident Field Modeling Error

As a preliminary assessment of modeling error, an incident field dataset (empty chamber, open top) was collected under each of the 6 conditions over a frequency range of 0.7 to 1.5 GHz. Equivalent synthetic data was generated using the EIL's forward solver. All the datasets were normalized by their respective maximum magnitudes, and the resulting amplitudes were compared. Figure 4.8 shows this comparison for probe 2 transmitting and the remaining 23 probes receiving at two different frequencies. It is clear that the raw measured data for all 6 conditions measured data matches the synthetic data reasonably well, though clearly the match is much better at 0.8 GHz than 1.2 GHz. This examination of raw data is helpful since it indicates that without calibration the modeling error is reasonably low. However, this examination is of limited use, since calibration is always still required and can correct many of the deviations.

The field distributions plotted in Figure 4.8 are of magnitude only. The phases for the raw measured and synthetic datasets are a very poor match. This is expected due to the path length variation in the RF switch and cabling. In order to determine if the very poor phase match was primarily due to the switch and cabling, or if the error was from another source, a subset of the antenna pairs were manually calibrated at the probe port in order to remove the effect of the switch and cabling. This technique is obviously impractical for any real measurement scenario since it would require 552 (24×23) manual calibrations. The results for this manual calibration for 12 different transmit/receive pairs are shown in Figure 4.9. As is expected, the amplitude is still a good match, and now, the phases for the synthetic and measured data follow the same trend, with an easily calibrated phase shift of nearly 2π . These results indicate that the poor phase match observed previously is primarily due to the switch and cabling. Therefore, the calibration techniques discussed in the next section will take care of these variations, and we can proceed with confidence that there is good phase match between the raw data and numerical model.

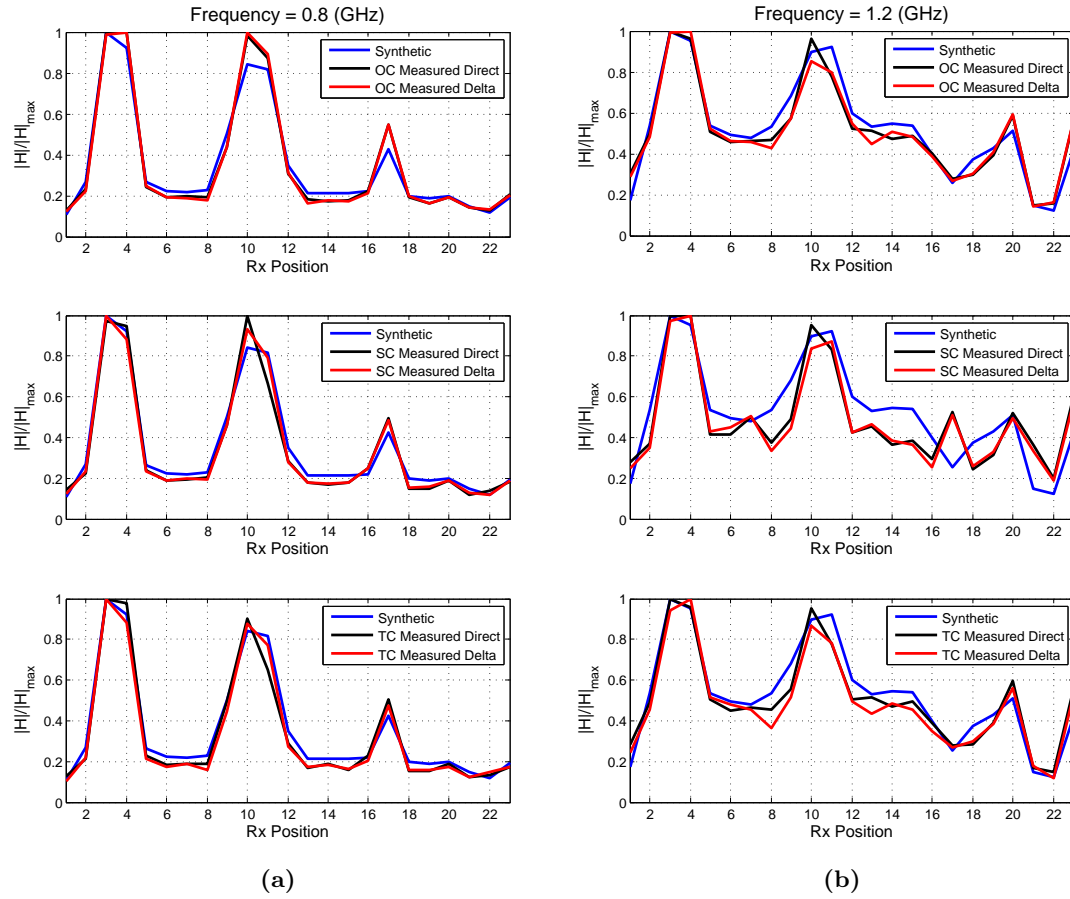


Figure 4.8: Comparison of synthetic incident field and raw measured data for a single transmitter at (a) 0.8 GHz and (b) 1.2 GHz. Measurements taken under different loading conditions and with direct and delta methods. All data normalized but not calibrated.

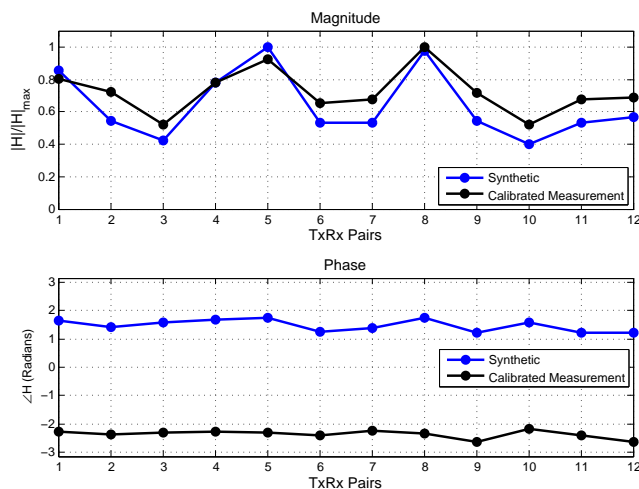


Figure 4.9: Magnitude and phase for manually calibrated probe pairs compared to synthetic equivalent. Data shown is collected at 0.9 GHz using the direct measurement technique and an OC load condition.

4.2.2 Data Calibration Techniques

Calibration of measured data is an important step in the process of obtaining images from an experimental system. Variations in cable length, probe/antenna manufacturing, and loading effects all must be compensated for. It is obviously impractical when dealing with an array of more than a few antennas to manually calibrate between every port pair. Furthermore, movement of RF cables after calibration can re-introduce phase errors, rendering a time consuming calibration immediately inaccurate. It is therefore important to have a calibration method that is not excessively time consuming and that does not require moving of cabling.

There are several approaches to calibrating MWI data, the ones employed in the EIL are summarized in: [53]. All of the EIL's calibration techniques involve collecting a dataset from the OI and one or two other datasets, an empty chamber and often some known reference object. These other datasets are used in conjunction with equivalent numerical data to form calibration coefficients that are used to scale the OI data prior to inversion.

In this work, 3 calibration techniques are used: incident, scattered, and total field calibration. These techniques are defined as below, where $U^{tot|obj}$ is the total field (U denotes measured S_{21} data) when a given object is in the chamber, U^{inc} is the field measurement for an empty chamber, H^{inc} is the calculated numerical incident field generated by the EIL's FEM forward solver, and $H^{tot|obj}$ is the numerical total field from the forward solver with a given object present. Also note that $H^{sct|obj} = H^{tot|obj} - H^{inc}$. For a given transmitter t and receiver r , the calibrated scattered field values are given by:

$$H_{r,t}^{sct|OI,ical} = \frac{H_{r,t}^{inc}}{U_{r,t}^{inc}}(U_{r,t}^{tot|OI} - U_{r,t}^{inc}) \quad (4.1)$$

$$H_{r,t}^{sct|OI,scal} = \frac{H_{r,t}^{sct|calobj}}{U_{r,t}^{tot|calobj} - U_{r,t}^{inc}}(U_{r,t}^{tot|OI} - U_{r,t}^{inc}) \quad (4.2)$$

$$H_{r,t}^{sct|OI,tcal} = \left(\frac{H_{r,t}^{tot|calobj}}{U_{r,t}^{tot|calobj}} U_{r,t}^{tot|OI} \right) - H_{r,t}^{inc} \quad (4.3)$$

where Equation 4.1 and the superscript *ical* indicate incident field calibration, Equation 4.2 and *scal* indicate scattered field calibration, and Equation 4.3 and *tcal* indicates total field calibration. We term the quantity in each calibration technique resulting from the division of numerical data by measured data a calibration coefficient C (e.g. $C_{r,t}^{inc} = H_{r,t}^{inc}/U_{r,t}^{inc}$). Note that for both scattered and total field calibration, a known calibration object, *calobj* is required to generate the numerical and experimental datasets. It is important that the shape, position, and electrical properties of the calibration object be well known and easy to model. For this reason, a metal target has been used in the EIL [23, 53] since analytic solutions exist for simple PEC scatterers. However, a PEC target may not always be the best choice for calibration object. Since any object placed in the chamber is in the near field region of the probes, there will be some loading effect on the antennas that ideally should be calibrated out. By choosing a calibration object that is similar to the OI, the

loading effect caused by the calibration object will be similar to that caused by the OI. Therefore, if possible, choosing a calibration object as similar as possible to the OI is desirable. Obviously, this may be very difficult for complicated targets with poorly known dielectric properties. In the next subsection, different calibration objects will be examined to further explore the impact of object selection on modeling error.

4.2.3 Targets Used for Calibration Assessment

In order to determine which calibration techniques and data collection schemes are most effective in the faceted chamber, a set of targets including an OI and two different calibration objects were required. Simple, easy to model targets were chosen so that a numerical equivalent could be accurately simulated. Two plastic cylinders ($r_{c1} = 22.08 \text{ mm}$, $h_{c1} = 75.48 \text{ mm}$ and $r_{c2} = 25.06 \text{ mm}$, $h_{c2} = 76.38 \text{ mm}$) were filled with canola oil ($\epsilon_r = 3.13 - j0.253$), and suspended with a thin line from a plexiglass support above the chamber. The third object was a metal sphere of radius $r_s = 25.42 \text{ mm}$. A cylinder and the metal sphere are pictured in Figure 4.10. The positions of each object were accurately measured so that a good numerical equivalent could be generated, as pictured in Figure 4.11.

Data was collected using the direct and delta technique under all three antenna loading conditions, and numerical data was generated for each of the three objects as well as an empty chamber.

4.2.4 Calibrated Scattered Field Modeling Error

To assess the modeling error for the system, cylinder #1 ($c1$) was selected as the OI, and cylinder #2 ($c2$) and the metal sphere (ms) were chosen as calibration objects. With these choices made, each of the 6 cylinder #1 data sets (3 antenna loading conditions \times 2 measurement techniques (direct and delta)) were calibrated in 5 different ways:



(a)



(b)

Figure 4.10: Targets suspended in chamber, (a) oil filled cylinder #2, (b) metal sphere.

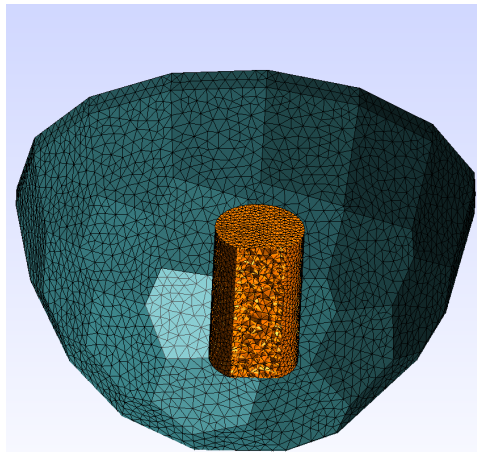


Figure 4.11: Cutaway view of numerical model for simple oil filled cylinder.

$$H^{sct|c1,ical} = \frac{H^{inc}}{U^{inc}}(U^{tot|c1} - U^{inc}) \quad (4.4)$$

$$H^{sct|c1,scal-c2} = \frac{H^{sct|c2}}{U^{tot|c2} - U^{inc}}(U^{tot|c1} - U^{inc}) \quad (4.5)$$

$$H^{sct|c1,scal-ms} = \frac{H^{sct|ms}}{U^{tot|ms} - U^{inc}}(U^{tot|c1} - U^{inc}) \quad (4.6)$$

$$H^{sct|c1,tcal-c2} = \left(\frac{H^{tot|c2}}{U^{tot|c2}} U^{tot|c1} \right) - H^{inc} \quad (4.7)$$

$$H^{sct|c1,tcal-ms} = \left(\frac{H^{tot|ms}}{U^{tot|ms}} U^{tot|c1} \right) - H^{inc} \quad (4.8)$$

yielding 30 different scattered magnetic field data sets for cylinder #1. To examine modeling error, the root-mean square error (*RMSE*) was calculated between each calibrated data set and the equivalent numerical scattered field data for cylinder #1. Prior to the error calculation, any calibrated field value having a magnitude greater than 2.5 standard deviations above the mean magnitude for the current data set was removed. This technique was employed to remove any particularly poor calibrated values. Note that the data removed during the error norm calculation is also removed when the data is inverted in Section 4.3.

$$RMSE = \sqrt{\frac{\sum_{n=1}^N |H_n^{sct|c1} - H_n^{sct|c1,cal}|^2}{N}} \quad (4.9)$$

The results of the error calculation are shown in Figure 4.12 for a selection of frequencies. Recall that the TC loads are adjusted to be most sensitive at 1 *GHz*, and that the SC loaded probes are most sensitive at 1.4 *GHz*.

Several conclusions can be drawn from the error calculations. First, as expected, scattered field and total field calibration using cylinder #2 as the calibration object yield the lowest error. The presence of an OI in the chamber has a loading effect on the antennas, and using a calibration object similar to the true OI causes a similar loading effect, and

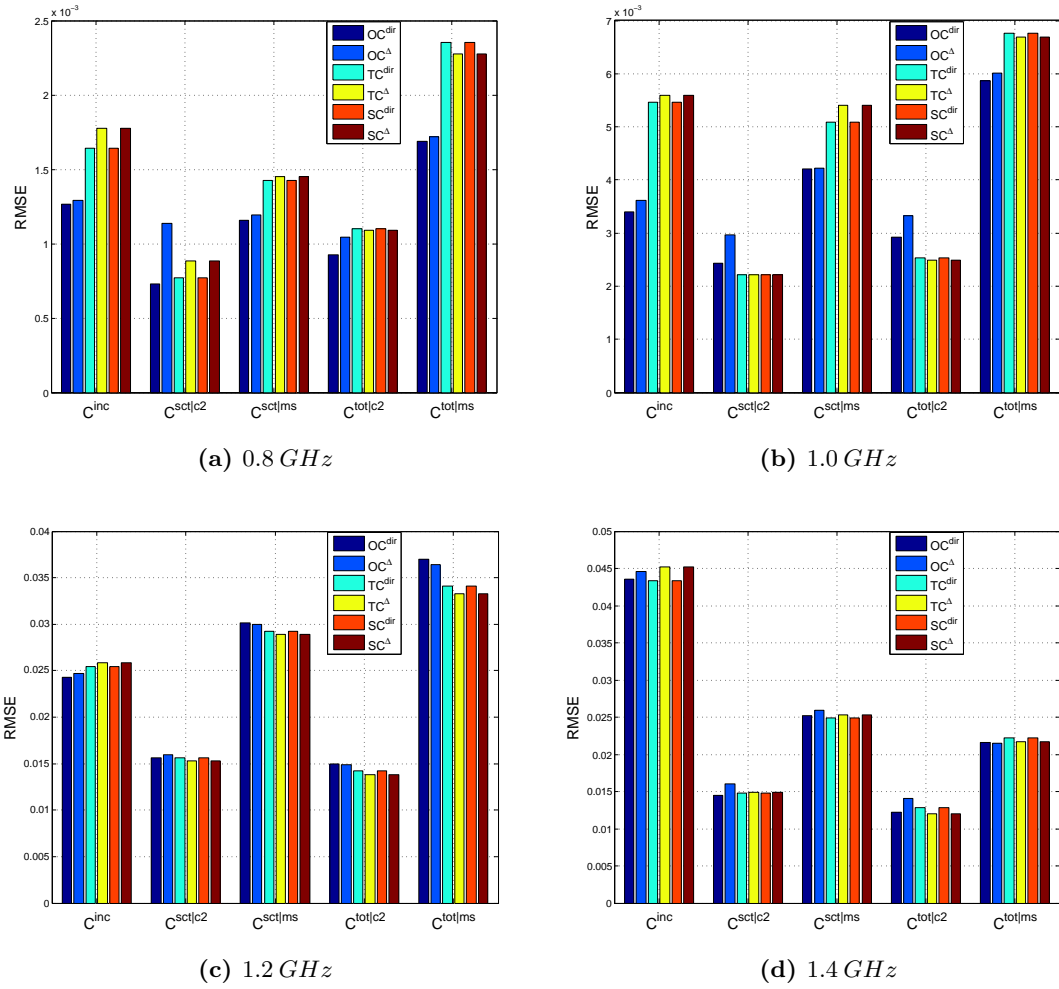


Figure 4.12: RMSE for all calibration types and measurement scenarios.

therefore good calibration is expected. Scattered and total field calibration using the metal sphere are an improvement over incident field calibration at 1.4 GHz , but not at the other frequencies. A second conclusion can be drawn with regards to the direct (*dir*) and delta (Δ) measurement techniques. The delta measurement does not result in consistent reduction in error across calibration types or loading conditions. This indicates that the electric field rejection due to the use of the shielded loop with a top gap is sufficient, and further removal of parasitic field components is not required. For this reason, and since the delta case requires twice as much data (and therefore twice the measurement time), the delta case is ignored for the rest of this work. The third and final conclusion drawn from the data here is that the loading condition does not have a dramatic affect on the error across the examined frequencies. At the lower frequencies, the OC case has the lowest error, but this difference is negligible at the higher frequencies.

It is of interest to note the difference between the two calibration objects at 1 GHz . The relative change in error between calibration objects is less for the OC load than for the TC and SC. This indicates that the OC load case is least sensitive to the calibration object, which is important as it is not always possible to obtain a calibration object that is very similar to the true OI.

Therefore, from this analysis, we conclude that for this faceted chamber and these antennas the best reduction in modeling error is achieved by using the OC load, direct S_{21} measurement, and scattered or total field calibration with an object that is similar in size and dielectric properties (if possible) to the OI.

4.3 Inversion of Simple Cylindrical Targets

The error analysis in the previous subsection exclusively examined calibrated forward data. In order to ensure that the error assessment of the forward data translated to improved reconstructions, this data was then inverted at 1.0 GHz and 1.4 GHz to examine the error

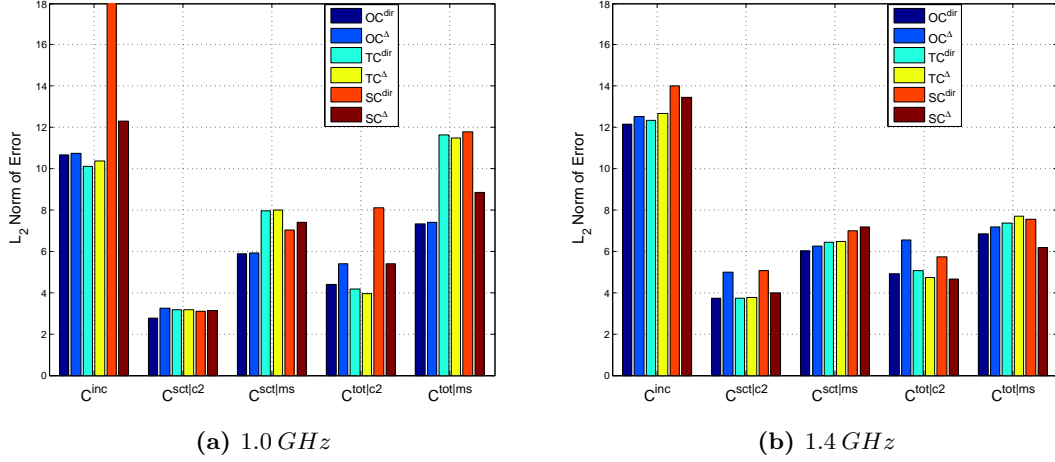


Figure 4.13: \mathcal{L}_2 norm of error between experimental inversions for all calibration types and measurement scenarios and the numerical reference.

trends in the reconstructions. The imaging domain was restricted to the interior chamber region (excluding the air dome), and the algorithm was terminated at 300 iterations. At every mesh location the reconstructed complex permittivity from each experimental data set was subtracted from the reconstructed complex permittivity from the equivalent numerical case. The \mathcal{L}_2 norm of this error vector was taken and is shown in Figure 4.13. When compared to the results presented in Figure 4.12, there is more variation in this result, but the same conclusions are drawn: that the best reduction in modeling error is achieved by using the OC load, direct S_{21} measurement, and scattered or total field calibration with an object as close as possible to the OI. The inversion results displayed in Figures 4.14, 4.15, 4.16, and 4.17 show the good match between the numerical and experimental results. The true permittivity of the object is underestimated and the imaginary part is poor, but this is expected when inverting a high contrast, low loss object with no prior information or regularization.

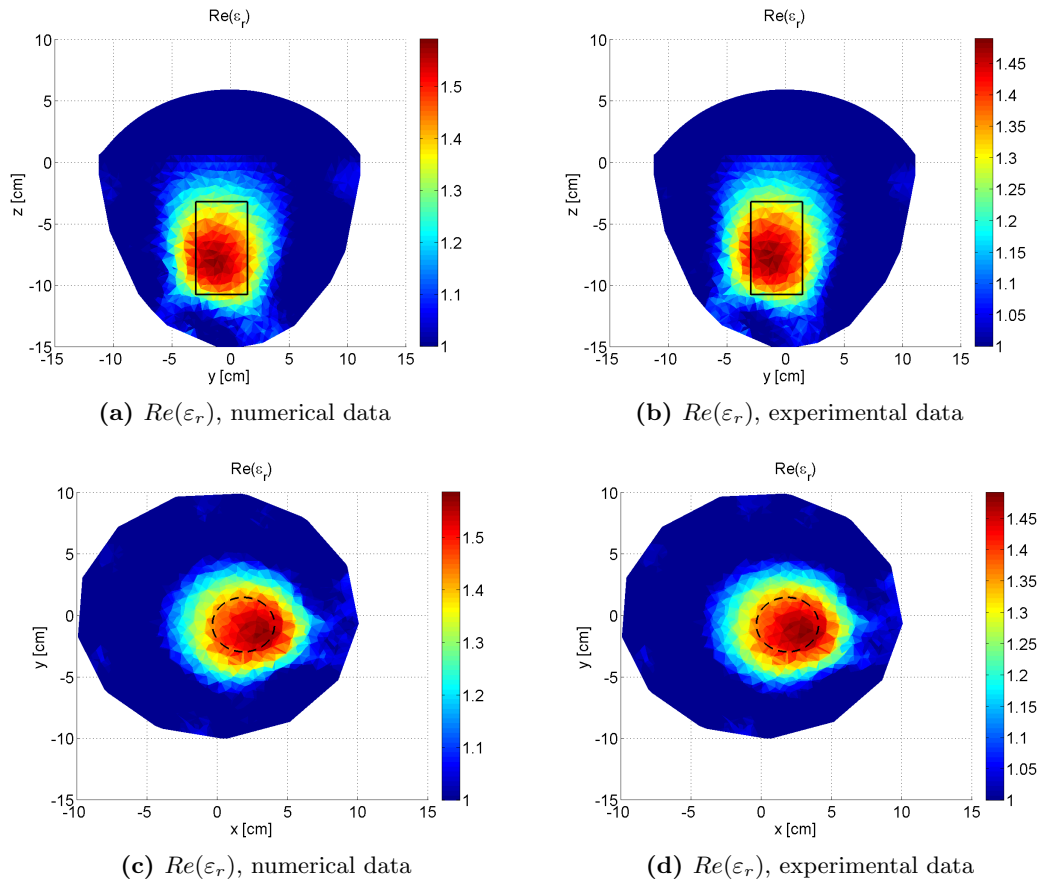


Figure 4.14: Real inversion results at 1.0 GHz. The left column is from the numerical data and the right column is from the OC loaded, $c2$ scattered field calibrated experimental data. The black circle and rectangle indicate the true position of the OI.

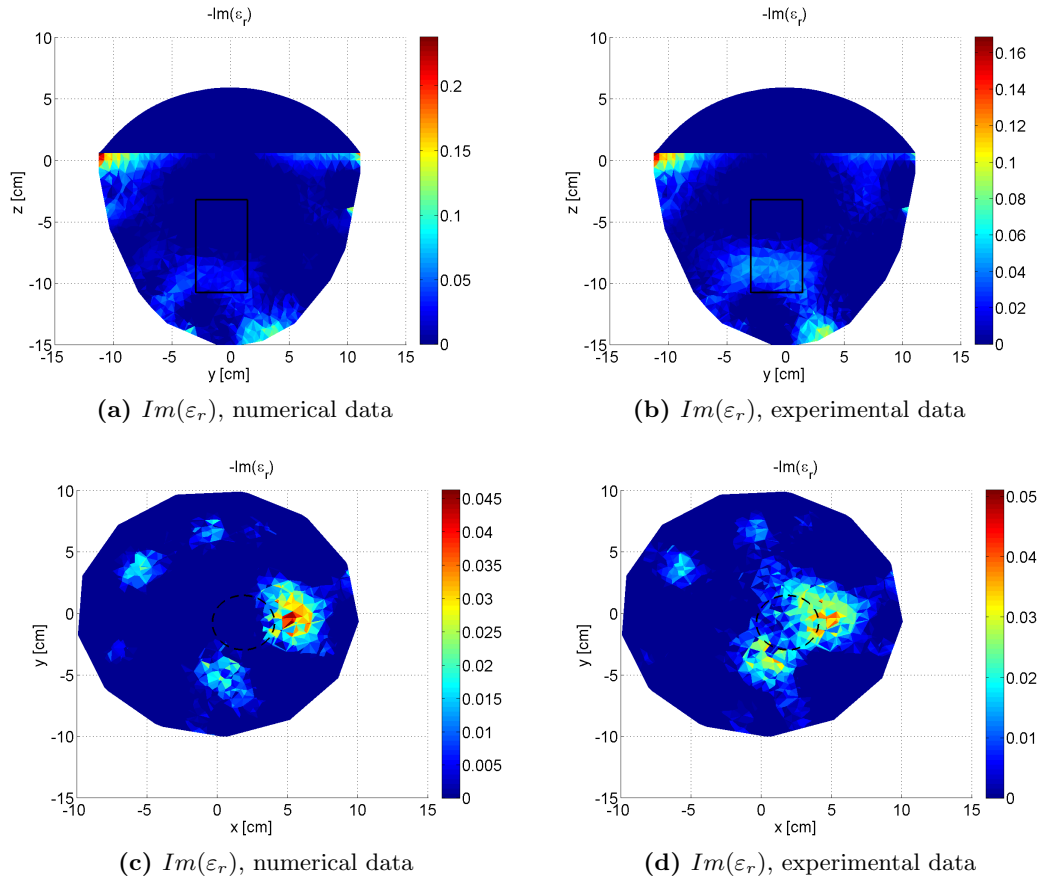


Figure 4.15: Imaginary inversion results at 1.0 GHz. The left column is from the numerical data and the right column is from the OC loaded, c_2 scattered field calibrated experimental data. The black circle and rectangle indicate the true position of the OI.

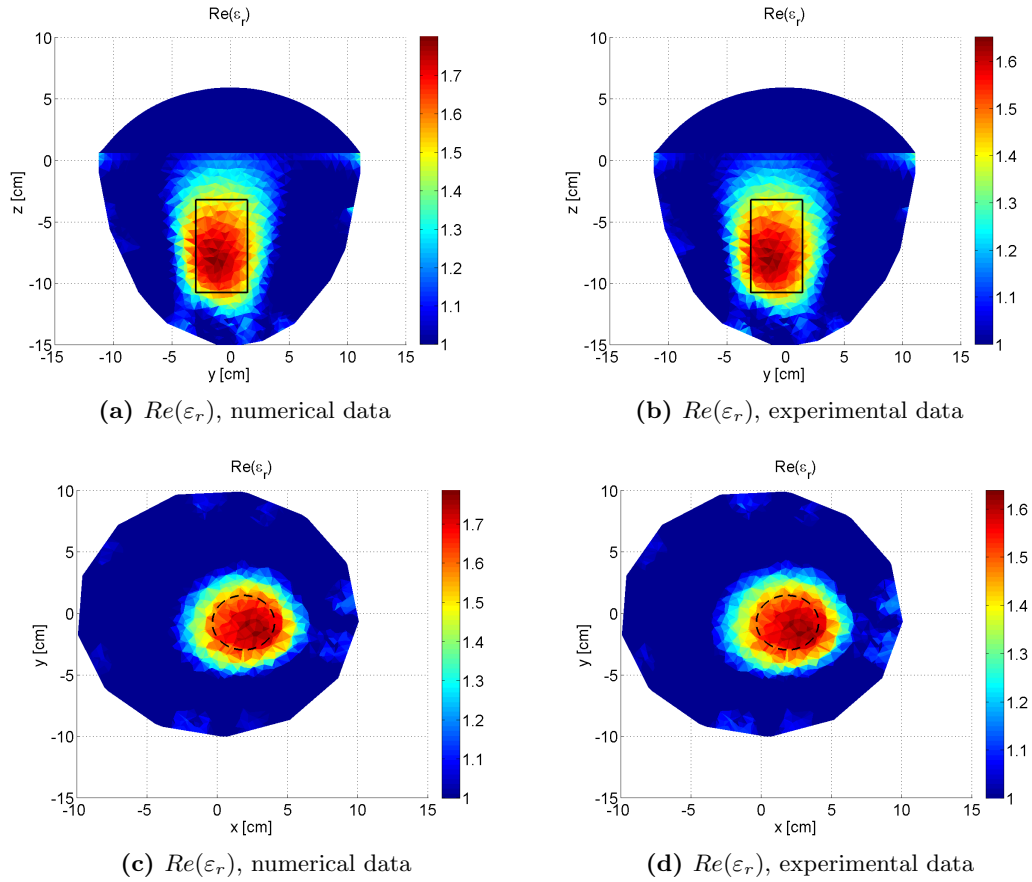


Figure 4.16: Real inversion results at 1.4 GHz. The left column is from the numerical data and the right column is from the OC loaded, $c2$ scattered field calibrated experimental data. The black circle and rectangle indicate the true position of the OI.

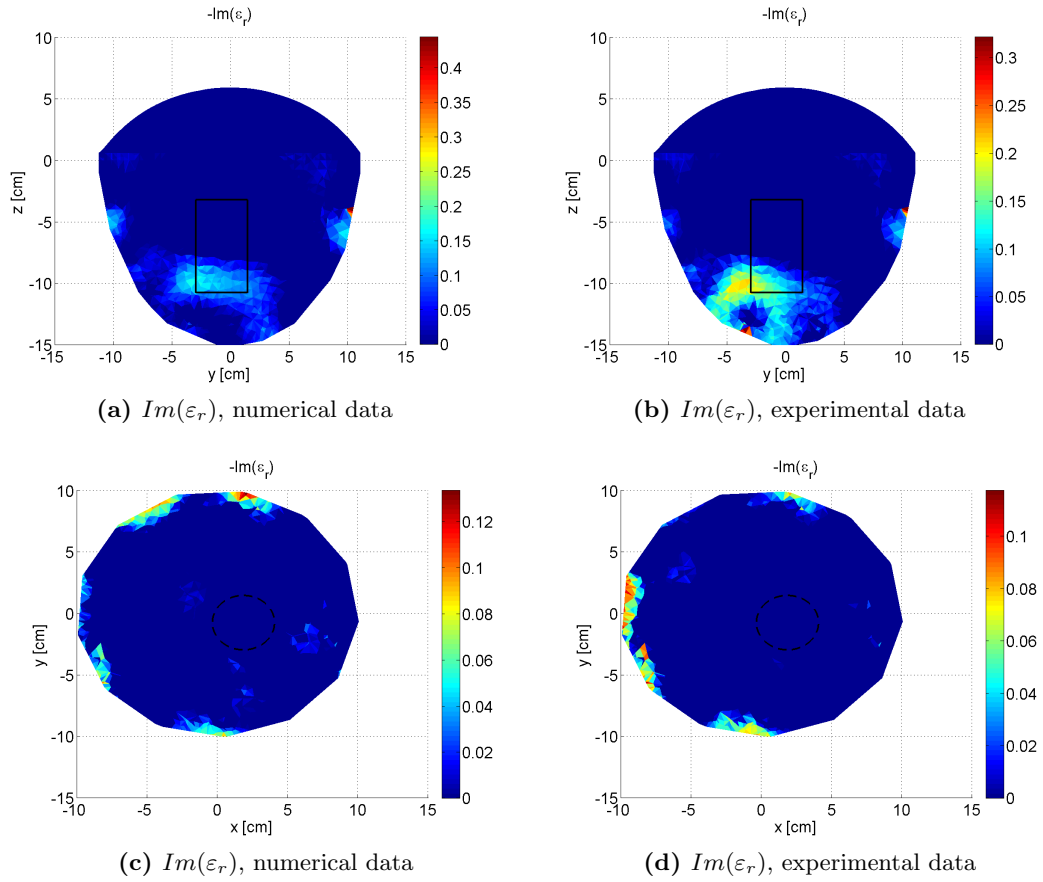


Figure 4.17: Imaginary inversion results at 1.4 GHz. The left column is from the numerical data and the right column is from the OC loaded, c_2 scattered field calibrated experimental data. The black circle and rectangle indicate the true position of the OI.

Chapter 5

Experimental Imaging of a Simple Breast Phantom

The ability to image simple targets in the novel faceted chamber was demonstrated in Chapter 4. The measurement and calibration techniques previously introduced are now applied in this chapter for imaging a more complicated object, namely a simple two region breast phantom. Experimental incorporation of prior is also introduced here, along with resultant reconstructions.

5.1 Simple Breast Phantom and Calibration Objects

Two plastic shells were created using a 3D printer at the U of M, one to act as the fat region of the simple breast target and the other for a calibration object. These objects are shown in Figure 5.1. The shells are less than 1 mm in thickness, and are therefore negligible from a modeling perspective ($\lambda/200$ at 1.5 GHz). Since the printed targets are porous, they were coated with a very thin silicone spray to seal the surface. The larger white shell is 113 mm in height and 97.5 mm in diameter, while the smaller black shell is 83 mm in height and 68 mm in diameter. A tumour target was created with a ping pong ball (3.8 cm diameter).

The wall of the ping pong ball and the supporting structure (also pictured in Figure 5.1) are also of negligible electrical size, and are also ignored.

The tumour was filled with a 10% water and 90% glycerin mixture and sealed. The calibration object and fat region were filled with canola oil. The dielectric properties of these materials are shown in Figure 5.2. Canola oil has very little variation across the frequency band of interest, averaging $\epsilon_r = 3.07 - j0.26$. This is relatively close to the true value of fat tissue, whose real relative permittivity is typically between 4 and 5, and with imaginary permittivity around -0.7 [8]. The water/glycerin mix in the tumour is much more dependent on frequency, and is also a less realistic analog of tumour tissue. The real permittivity of tumour tissue typically exceeds a $\epsilon_r = 40$ [8], though the phantom tumour's imaginary permittivity is in the correct range. As seen in previous inversion results in this work, the FEM-CSI algorithm often underestimates the true permittivity of a scatterer with very high contrast. A tumour of $\epsilon_r = 42 - j14$ embedded in canola oil has a contrast of $\chi = 12.97 - j3.38$. Since the reconstruction was not expected to reach this high contrast, so a somewhat lower contrast target was chosen ($\chi_{10:90} = 4.37 - 3.78$ at 1 GHz).

Though more biologically realistic targets could be constructed, for an initial test, and given the materials available in the EIL, the described targets were deemed appropriate to evaluate the performance of the chamber.

5.2 Data Collection & Inversions

A plexiglass plate ($\epsilon_r = 3 - j0.001$, 6 mm thick) was placed over the chamber in order to suspend and accurately position the objects. Field data was collected using the direct measurement technique and OC loaded probes with the following objects positioned in the chamber:

- Empty chamber (with plexiglass plate present)

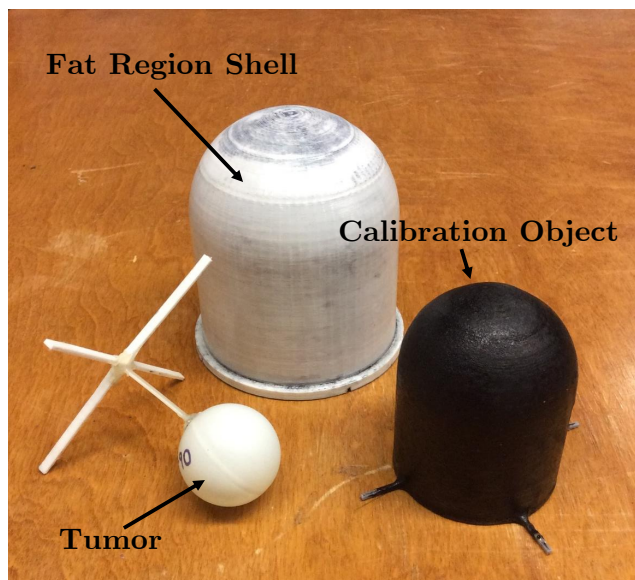


Figure 5.1: Simple breast targets and calibration object.

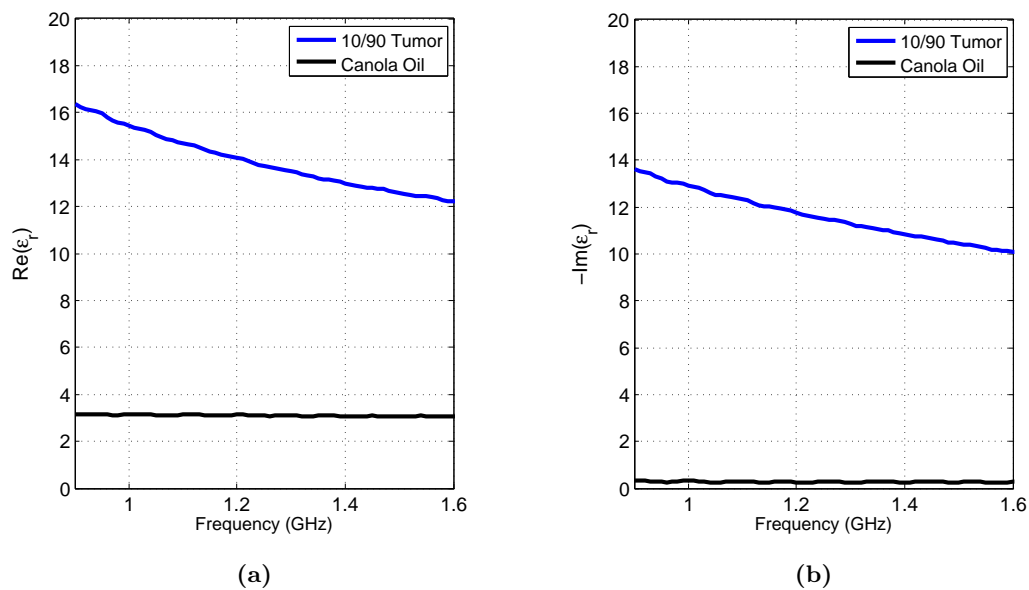


Figure 5.2: Electrical properties of canola oil and 10:90 water/glycerin tumour, (a) real part and (b) imaginary part.

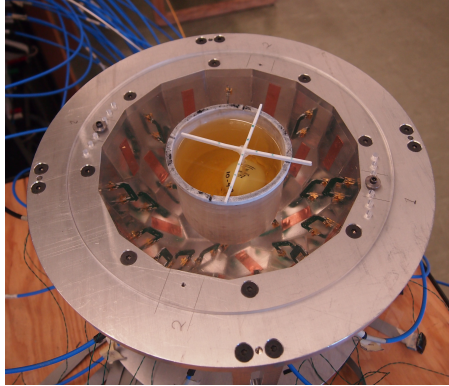


Figure 5.3: Simple breast targets in chamber.

- Canola oil filled “fat” shell, centered
- Canola oil filled “calibration” shell, centered
- Canola oil filled “fat” shell, tumour phantom offset from shell center (Figure 5.3)
- Canola oil filled “fat” shell, tumour phantom with different offset from shell center

All data was collected between 0.9 GHz and 1.5 GHz in 10 MHz steps. The IF Bandwidth of the VNA was set to 700 Hz and averaging was disabled.

5.2.1 Discarding Data

As mentioned in Section 4.2.4, and detailed in [31], discarding appropriately selected data is often beneficial for improving inversions results. Two criteria were used for removing data: proximity of antennas and magnitude of calibrated scattered field. Firstly, the chamber was examined and a list of antenna pairs that were in very close proximity to each other were noted. Though the assessment carried out in Section 4.1.2 shows that neighbouring antennas do not have a significant perturbing effect, there is another factor at play. Due to close proximity, for a noted Tx/Rx pair, the magnitude of any scattered field from a present target will be much lower than the incident field received by the Rx probe. Therefore, the

data from a total of 14 Tx/Rx pairs was removed for every inversion detailed in the following sections. Additionally, after calibration, as in Section 4.2.4, any scattered field value having a magnitude greater than 2.5 standard deviations above the mean magnitude for the current data set was removed. This was done to remove the effect of any outstandingly poor calibration. The specific calibration methods used for these targets are detailed in Section 5.2.3. For all the datasets inverted in this Chapter, no more than 10% of the scattered field data was discarded.

5.2.2 Blind Inversions

To demonstrate the importance of prior information when inverting larger multi-layered targets, calibrated scattered field data was initially inverted without prior information (blind). The scattered field data set was obtained from the fat region with the tumour in the first offset position, and total field calibration (using the calibration shell) was used:

$$H^{sct|fat+tum,tcal} = \left(\frac{H^{tot|calobj}}{U^{tot|calobj}} U^{tot|fat+tum} \right) - H^{inc} \quad (5.1)$$

Note that all specified fields (including the incident fields) also include the presence of the plexiglass plate. It is used as prior information in the inversions.

For the blind inversions, the imaging domain was restricted to a cylinder of radius 5.375 cm and height 12.475 cm, which surrounds and is slightly larger than the known location of the fat shell. Scattered field data was inverted at frequencies between 0.95 GHz and 1.5 GHz in steps of 50 MHz, with each inversion terminated after 150 iterations. A selection of results are displayed in Figure 5.4 at several frequencies. Only the real part of the reconstructed permittivity is displayed, as the imaginary part of the reconstructions are very poor at all frequencies. As indicated by the accompanying convergence plots, the algorithm is indeed converging, but to a poor solution. As seen in the vertical cross section images, large permittivity small size artifacts appear at the edges of the imaging domain.

The horizontal cross section at 1.2 GHz and 1.50 GHz actually do show the tumour being reconstructed in the correct position (indicated by the black circle), however the fat region is very irregular and poorly reconstructed. From these results, it is clear that if useful images are desired, blind inversion will not suffice.

5.2.3 Experimental Incorporation of Prior

Incorporating prior information in synthetic problems was introduced in Section 1.1.3 and used in Section 2.2. The process is similar for experimental data, though it is complicated by the calibration process. For synthetic problems, the scattered field with respect to some prior information background (PI) is given by:

$$H^{sct|OI} = H^{tot|OI} - H^{inc|PI} \quad (5.2)$$

and the incident field in the corresponding inversion step is computed with the prior information present in the background. For the simple breast target, the ideal prior information is shown in Figure 5.5. Position and permittivity for the fat and plexiglass regions are known, but there is now knowledge of the tumour's properties.

The most obvious, and realistic method for incorporating prior information experimentally is given by:

$$H^{sct|tum} = CU^{tot|fat+tumour} - H^{tot|fat} \quad (5.3)$$

where C is some calibration coefficient. The measured OI data is scaled and then the FEM-generated numerical field in the presence of the prior is subtracted to generate the calibrated scattered field. An alternative to this method exists for the simple breast target under examination in this section since we have access to a measurement of the fat region with no tumour present:

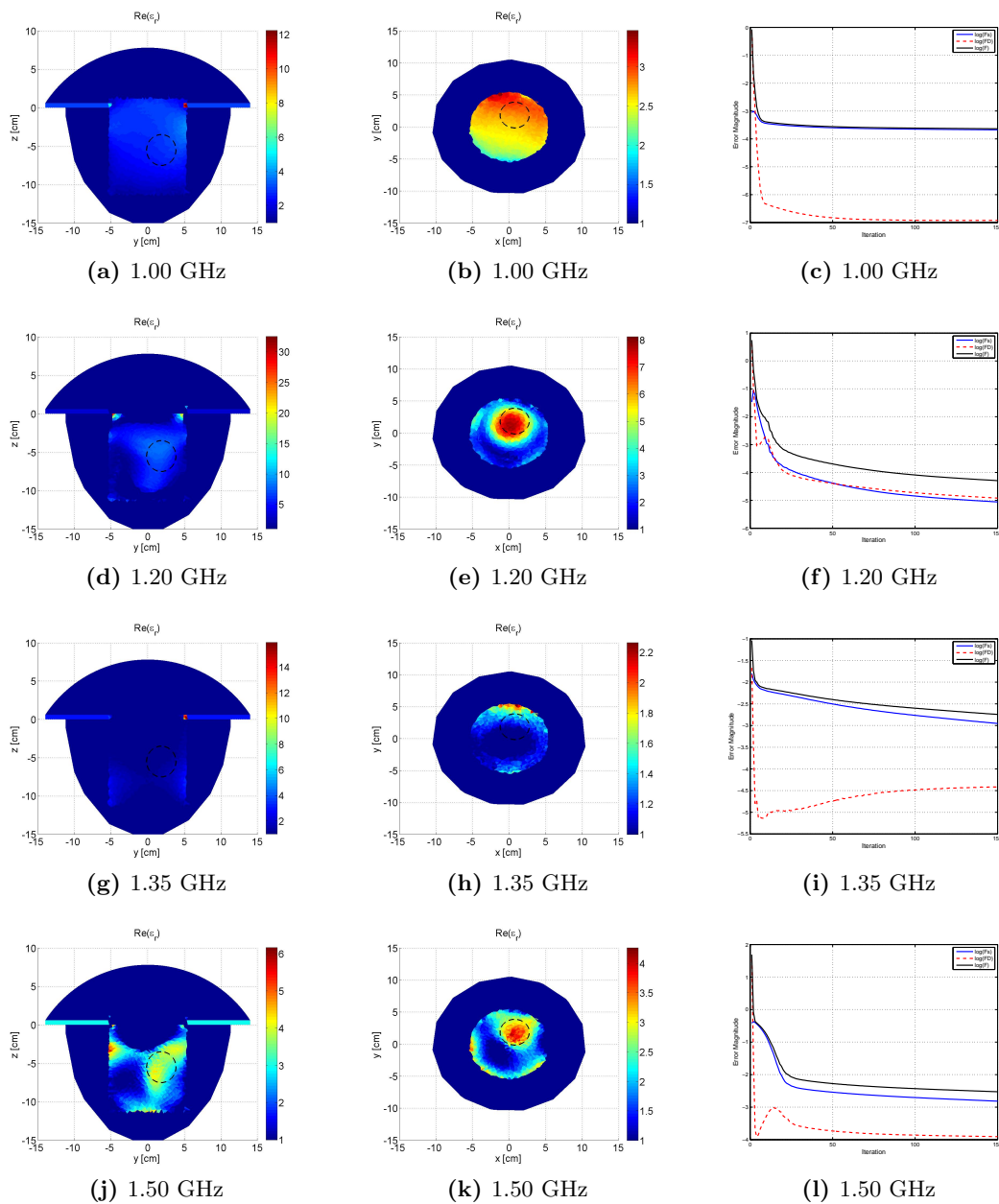


Figure 5.4: Blind inversion results for simple breast phantom at several frequencies. The 2 left columns show $Re(\epsilon_r)$ and the right columns shows the algorithm's error convergence.

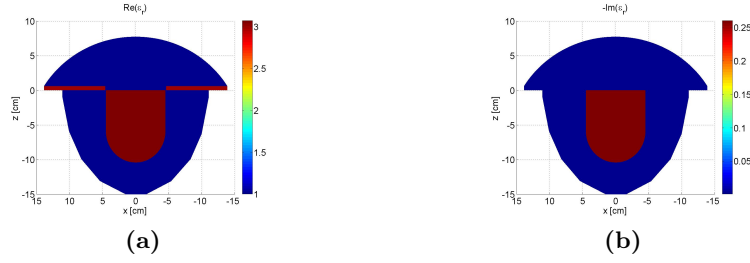


Figure 5.5: Prior information, (a) $Re(\varepsilon_r)$ and (b) $-Im(\varepsilon_r)$.

$$H^{sct|tum} = C(U^{tot|fat+tumour} - U^{tot|fat}) \quad (5.4)$$

In this instance, the total field due to the prior information comes from an experimental measurement as opposed to a numerical solution. The inversion algorithm still requires an accurate model of the breast without a tumour. Obviously, in practical clinical applications, obtaining experimental prior is quite difficult, since there is no access to an identical tumour-free patient, necessitating a suitable substitute object¹. Though the use of experimental prior is of limited applicability, it is examined here in order to determine if there are substantial differences in the results obtained compared to the realistic use of numerical prior.

5.2.4 Inversions Using Prior Information

In order to assess the incorporation of prior, all three calibration techniques (incident, scattered, and total field calibration) were used when appropriate. These were applied to both the numerical FEM prior (FP) and the experimentally measured prior (MP) techniques. Therefore, for a total field dataset $U^{tot|fat+tumour}$ at each given frequency, the scattered field used for inversion was calculated in four different ways:

¹Solutions to this problem are actively being researched in the EIL.

$$H_{FP}^{sct|ical} = \frac{H^{inc}}{U^{inc}} U^{tot|fat+tum} - H^{tot|fat} \quad (5.5)$$

$$H_{FP}^{sct|tcal} = \frac{H^{tot|calobj}}{U^{tot|calobj}} U^{tot|fat+tum} - H^{tot|fat} \quad (5.6)$$

$$H_{MP}^{sct|ical} = \frac{H^{inc}}{U^{inc}} \left(U^{tot|fat+tum} - U^{tot|fat} \right) \quad (5.7)$$

$$H_{MP}^{sct|scal} = \frac{H^{sct|calobj}}{U^{tot|calobj} - U^{inc}} \left(U^{tot|fat+tum} - U^{tot|fat} \right) \quad (5.8)$$

In addition to these experimental datasets, an equivalent fully numerical problem was set up. The approximate location of the tumour in the first offset position was used, and the following scattered field data was also calculated:

$$H_{FEM}^{sct} = H^{tot|tum+fat} - H^{tot|fat} \quad (5.9)$$

As in Section 5.2.2, the imaging domain was restricted to a cylinder of radius 5.375 cm and height 12.475 cm, which surrounds and is slightly larger than the known location of the fat shell. Scattered field data was inverted at frequencies between 0.95 GHz and 1.5 GHz in steps of 50 MHz, with each inversion terminated after 150 iterations. Both the real and imaginary permittivity results are shown in the following figures in two cross sectional planes for each of the five scattered field datasets. Figure 5.6 shows the results at 0.95 GHz, Figure 5.7 at 1.15 GHz, Figure 5.8 at 1.30 GHz, Figure 5.9 at 1.45 GHz, and Figure 5.10 at 1.50 GHz. In all the figures, the dotted black circle indicates the true location of the tumour target.

As can be seen in Figure 5.6, all the results at 0.95 GHz are quite poor. There is a discernible “hot spot” that encompasses approximately half of the fat region. Though this is the correct half of the region that has the tumour, the localization is extremely poor. All of the experimental results match the FEM result reasonably well, save the $H_{FP}^{sct|tcal}$ dataset.

In the imaginary part of the $H_{FP}^{sct|tcal}$ results there is an observable hot spot near where the tumour is located. However since the corresponding real part is very poor, and no other datasets have a similar hot spot, this is almost certainly an artifact and not a detection of the tumour.

Examining the results in Figure 5.7, at 1.15 GHz, the tumour becomes visible for some datasets, most notably in the real part of the FEM result. A more localized hot spot shows up in the corresponding imaginary part, but the image is still considered quite poor. Both measured prior results also begin to detect the tumour in the real part, but have nothing of use in the imaginary. There is undesirable non-uniformity in the fat region, particularly in the incident field calibrated measured prior result. Both results using FEM prior are quite poor. It is difficult to determine if the hot spot in the imaginary part is a hot spot or an artifact.

At 1.30 GHz (Figure 5.8), the pure FEM and measured prior results begin to improve dramatically. In both the real and imaginary parts the tumour becomes much more localized and the fat background is somewhat more uniform. The tumour permittivity actually meets (and exceeds) its true value of $Re(\epsilon_r) = 13$ in the experimental results. At this frequency, both FEM prior results are extremely poor.

The results continue to improve at 1.45 GHz, shown in Figure 5.9 in all but the $H_{FP}^{sct|ical}$ case, which remains quite poor. Good tumour localization is achieved in the real and imaginary parts of the measured prior and pure FEM cases. The peak tumour permittivity is however now undershot from the true value, and the highest contrast portion of the tumour region is smaller. The FEM prior total field calibration case now shows a discernible tumour hot spot in the real part. However, the fat region is more irregular in this case compared to the measured prior results, and the imaginary part is still poor.

As seen in Figure 5.10, the results at 1.50 GHz are very similar to those at 1.45 GHz. The main notable difference is that the tumour hot spot becomes extremely localized and smaller

than the true object. However this degradation in quality comes with an improvement in the fat region.

In order to verify that changes in the physical tumour position could be tracked in the inversion results, the measured data with the tumour in a second offset position was also calibrated and inverted. This was performed at 1.45 GHz for total field calibrated FEM prior and incident field calibrated measured prior. The inversion results shown in Figure 5.11 confirm that the change in tumour position is detected. These results are very similar to the first position equivalents shown in Figure 5.9.

In summary, these results show a marked improvement over the blind inversions in Section 5.2.2. The tumour target is apparent at several frequencies, sometimes both in the real and imaginary part. It is also clear from these results that using experimentally acquired measured prior is superior to FEM generated prior. The measured prior results match quite well with the pure FEM reference case. Determining methods for improving the FEM prior technique is of great importance since, as previously mentioned, this technique is clinically realistic, whereas the measured prior technique is not.

5.2.5 Inversions Using Multiple Frequencies

Image quality is impacted by the amount of scattered field data used in the inversion process, and within some limits, increasing the amount of data leads to improved results [31]. The most obvious way to increase the amount of data is to increase the number of Tx/Rx pairs, though the test equipment in the EIL is limited by the 2 to 24 port RF switch. An alternate method to increase the amount of received data is to use the modulated scatterer technique (MST) [41, 54]. Though effective, implementing an MST system is beyond the scope of this work. A third method of increasing the amount of data is by inverting at multiple frequencies simultaneously. This effectively doubles the amount of data available. In the EIL's FEM-CSI code, simultaneous frequency inversion yields a single result, and

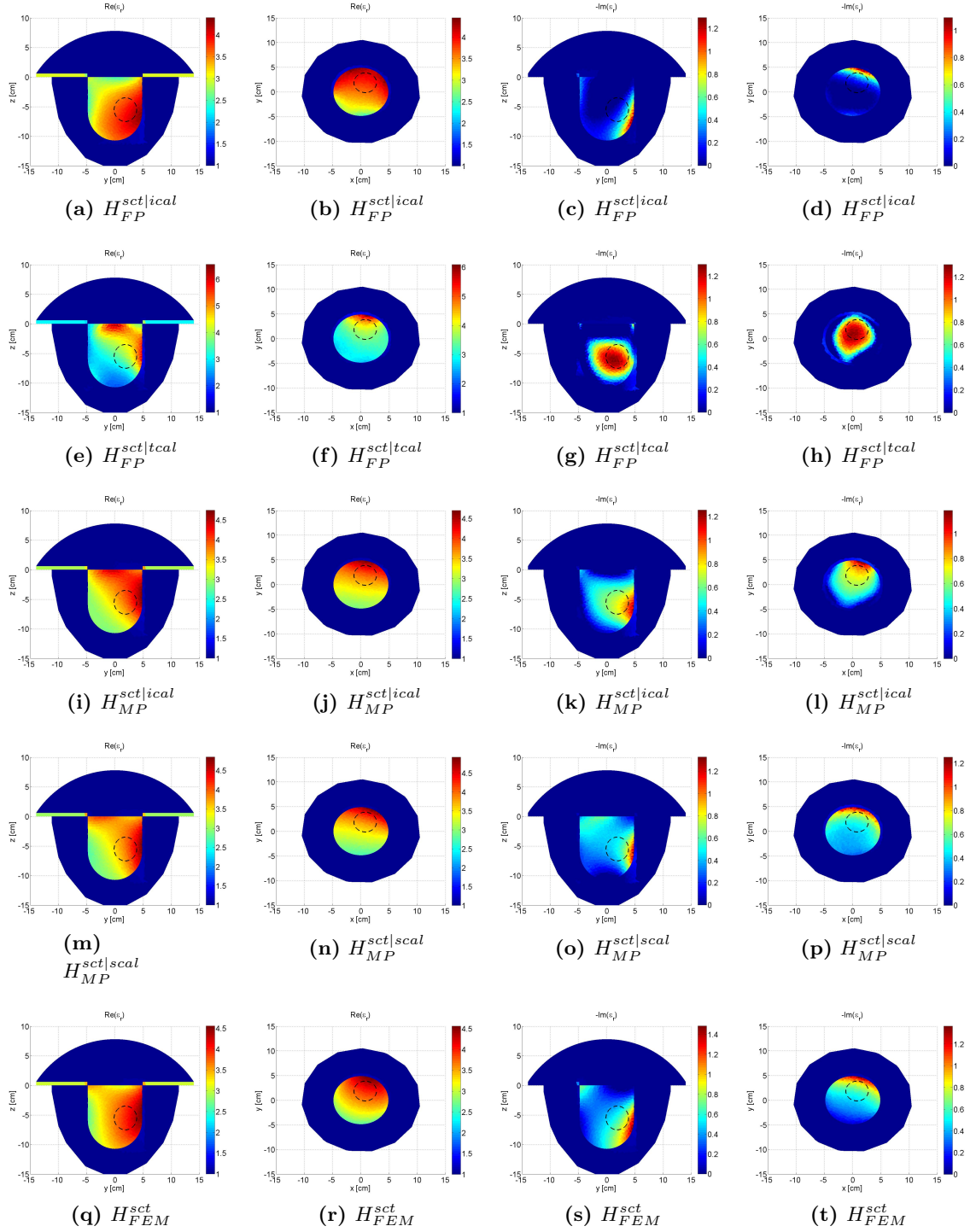


Figure 5.6: Inversion results for simple breast phantom at 0.95 GHz. The 2 left columns show $Re(\epsilon_r)$ and the 2 right columns show $-Im(\epsilon_r)$.

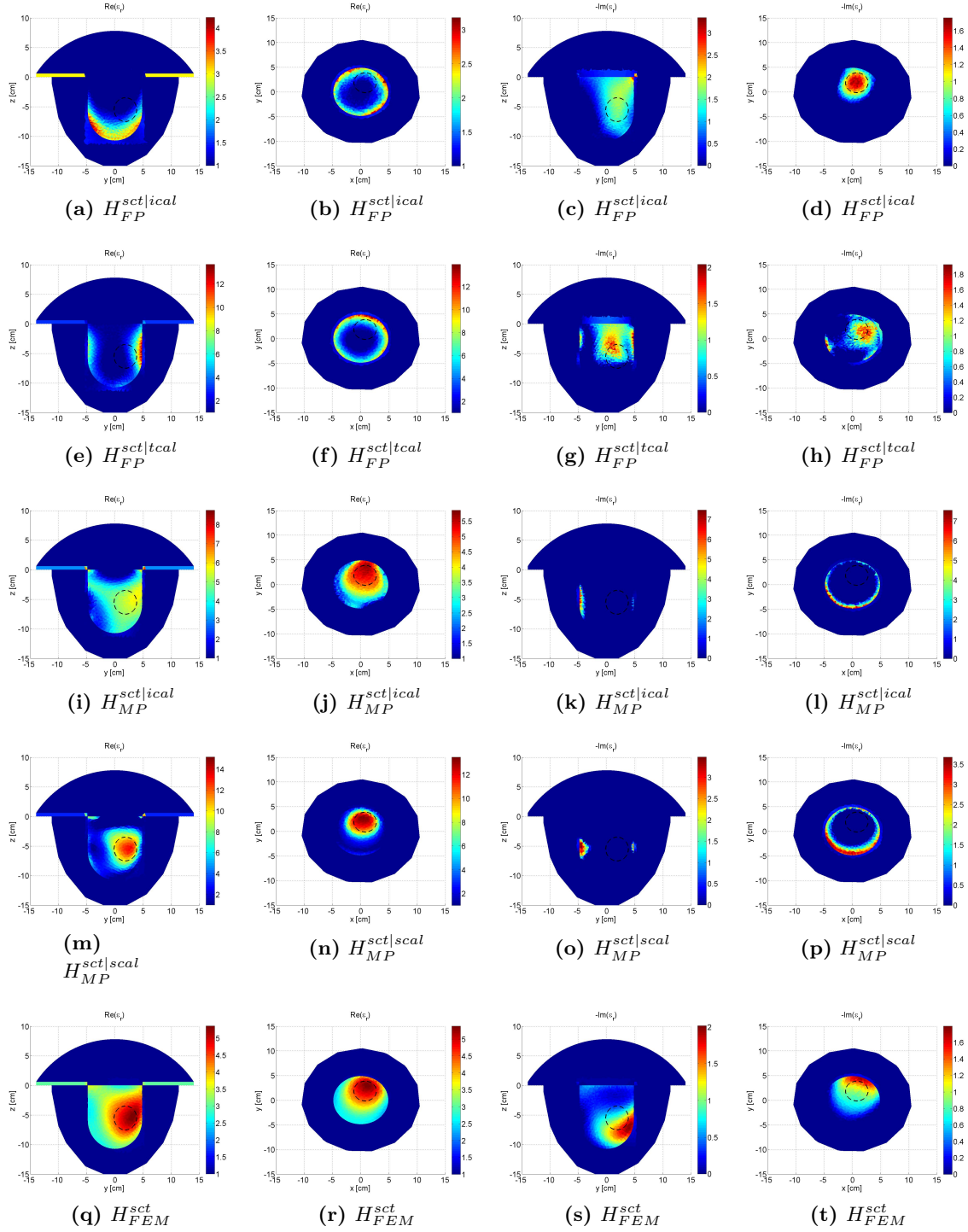


Figure 5.7: Inversion results for simple breast phantom at 1.15 GHz. The 2 left columns show $Re(\epsilon_r)$ and the 2 right columns show $-Im(\epsilon_r)$.

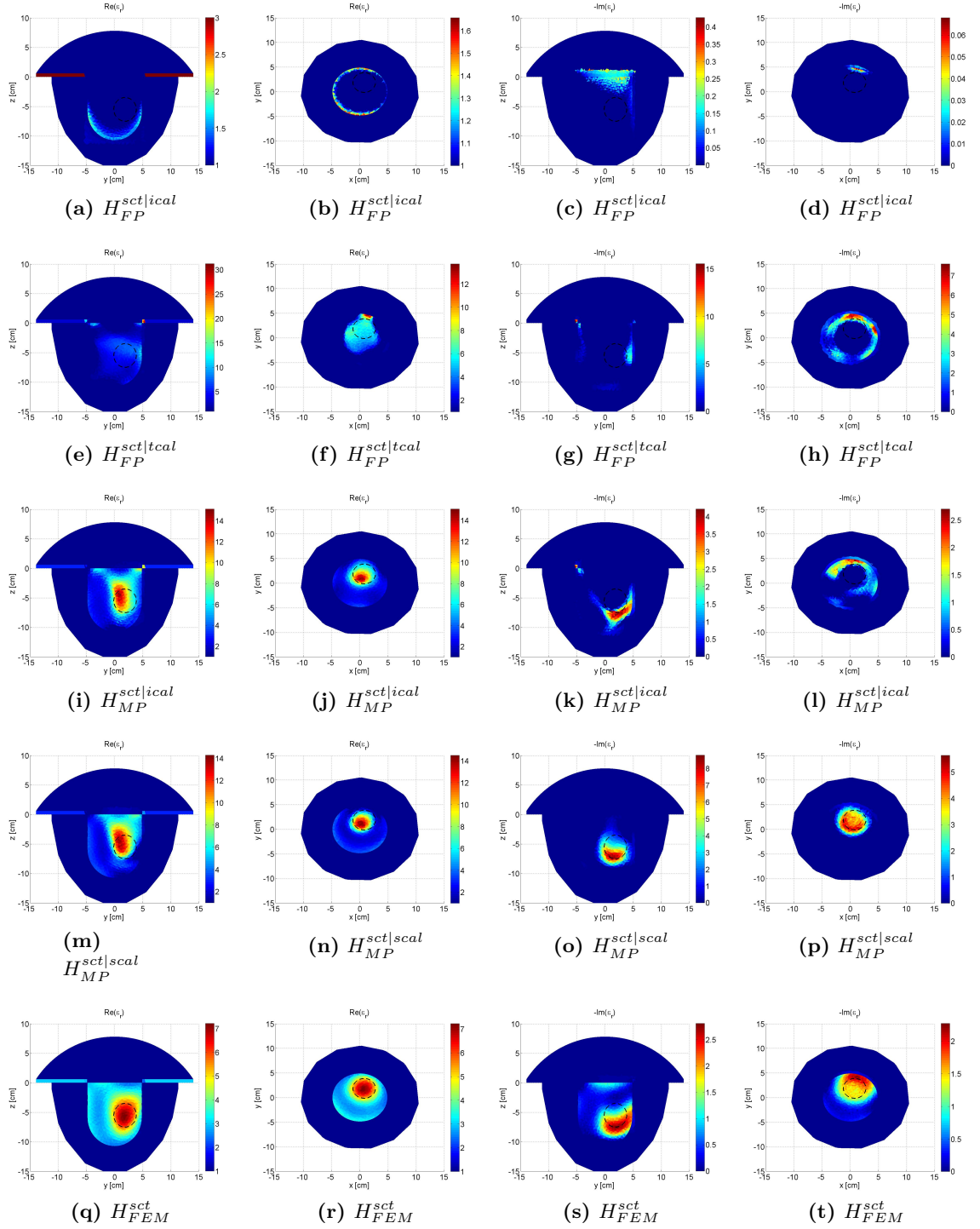


Figure 5.8: Inversion results for simple breast phantom at 1.30 GHz. The 2 left columns show $Re(\epsilon_r)$ and the 2 right columns show $-Im(\epsilon_r)$.

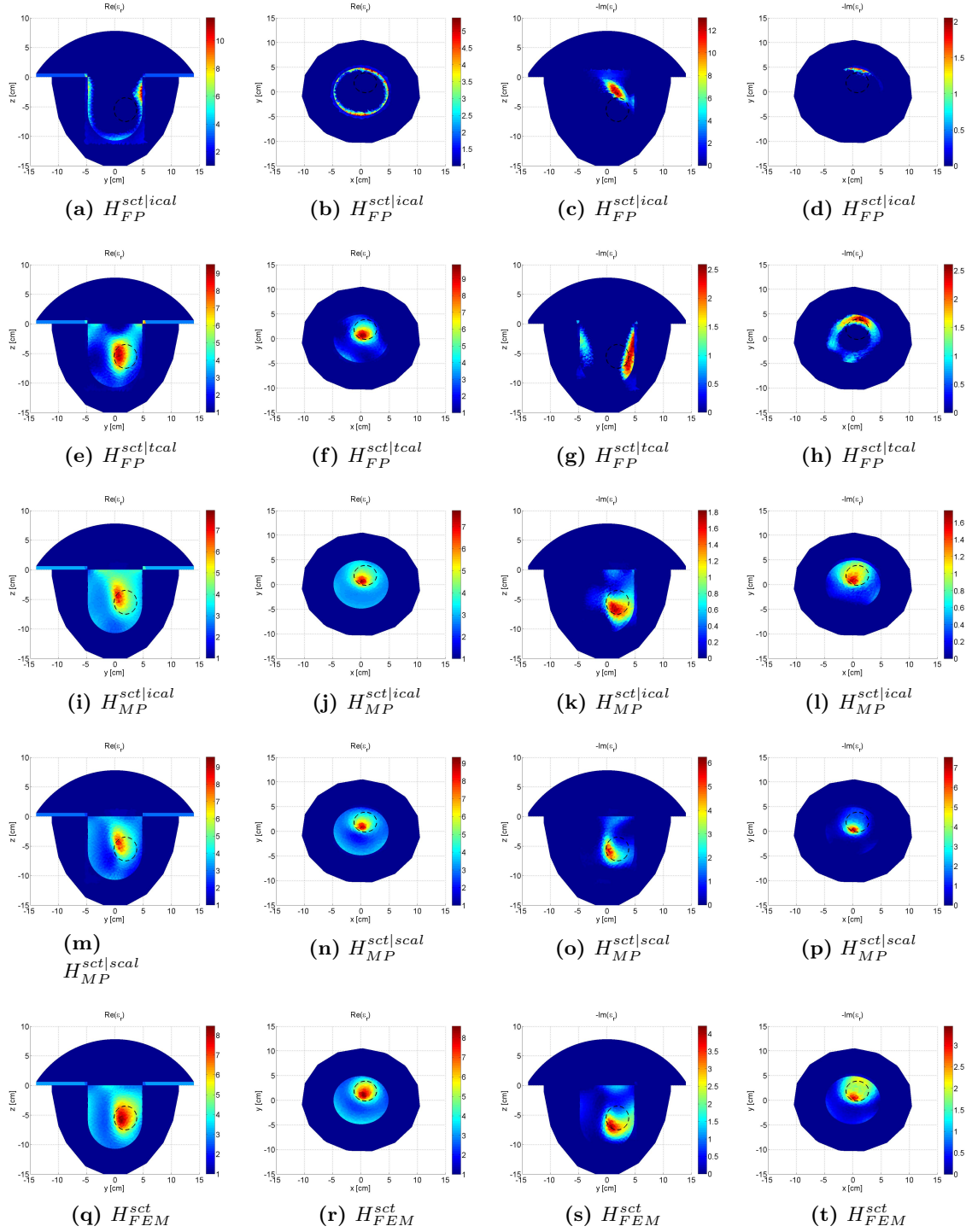


Figure 5.9: Inversion results for simple breast phantom at 1.45 GHz. The 2 left columns show $Re(\epsilon_r)$ and the 2 right columns show $-Im(\epsilon_r)$.

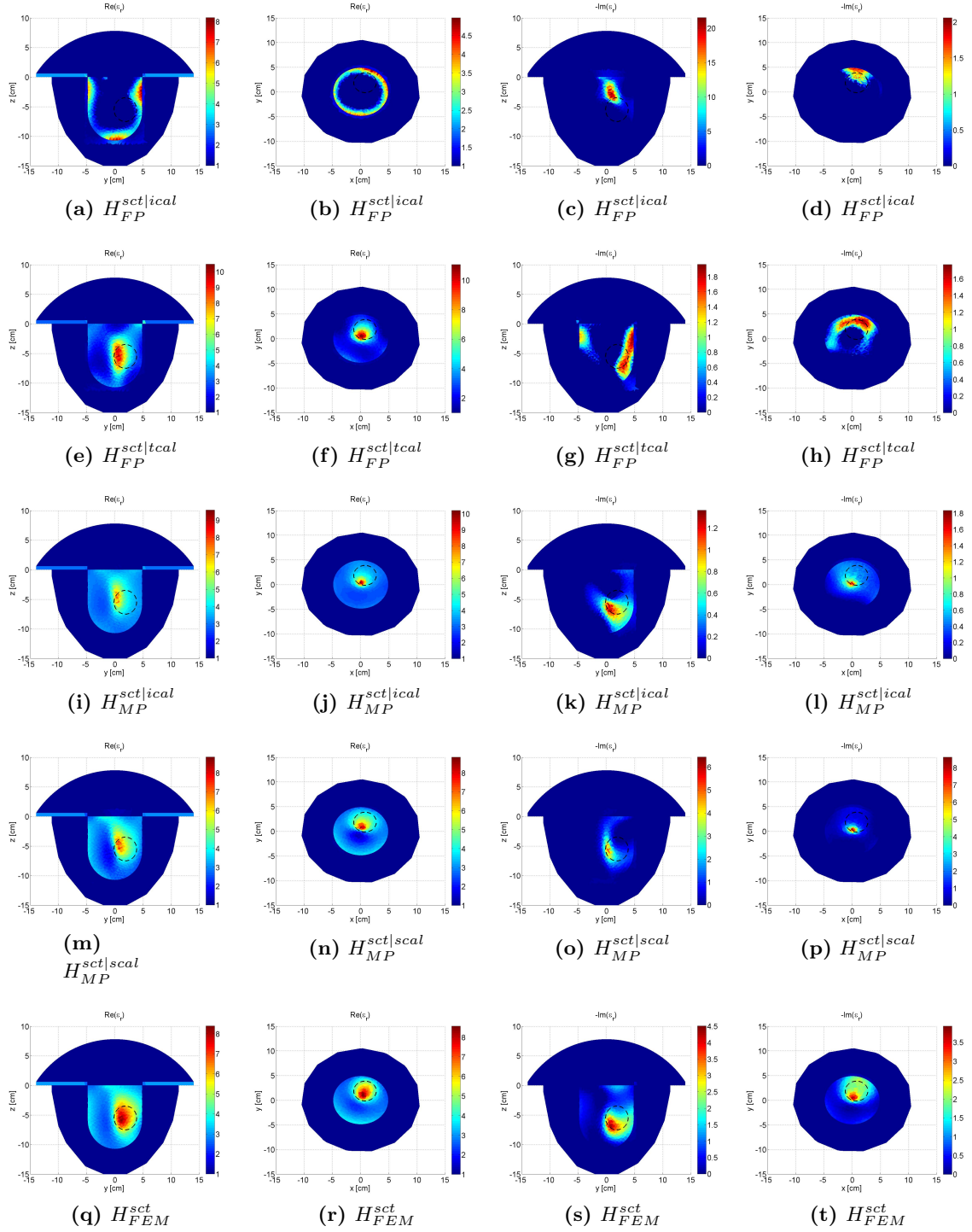


Figure 5.10: Inversion results for simple breast phantom at 1.50 GHz. The 2 left columns show $Re(\epsilon_r)$ and the 2 right columns show $-Im(\epsilon_r)$.

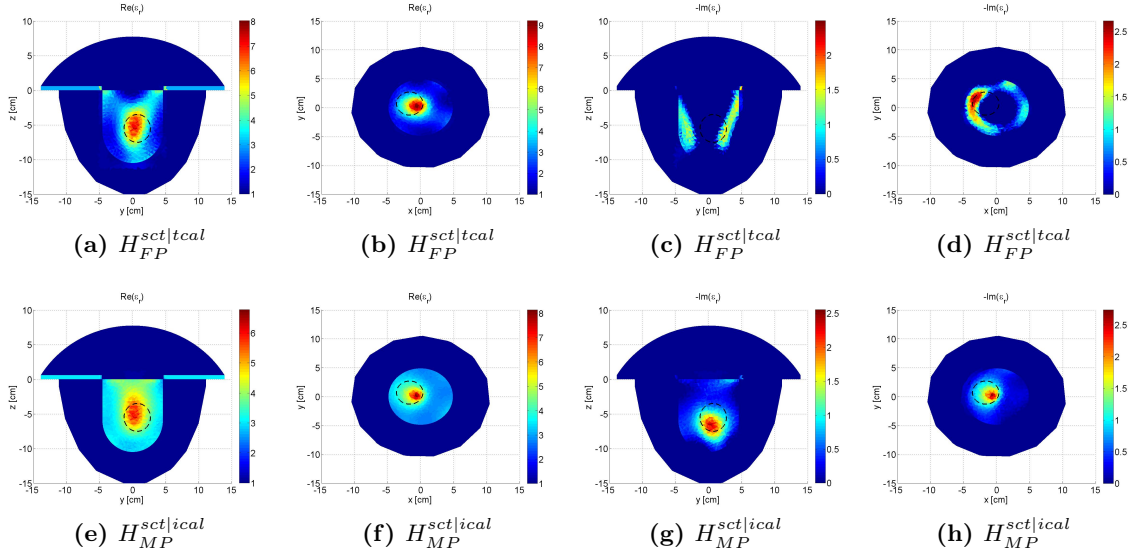


Figure 5.11: Inversion results for breast phantom with tumour in position two at 1.45 GHz. The 2 left columns show $Re(\epsilon_r)$ and the 2 right columns show $-Im(\epsilon_r)$.

therefore is not good for objects whose electrical properties vary significantly with frequency.

The efficacy of simultaneous frequency inversion was examined for the total field calibrated FEM prior case detailed in Section 5.2.4. The same imaging domain was used as in the previous subsections. Two different frequency combinations were chosen: 1 GHz with 1.4 GHz and 1.3 GHz with 1.4 GHz. More than 2 frequencies can be combined in the EIL FEM-CSI code, though these are the only combinations examined here. The results for the two combinations are shown in Figures 5.12 and 5.13. These results show the tumour hot spot readily apparent in the real part but not the imaginary. There is some improvement in fat region artifacts, though these improvements still result in images that are worse than the measured prior scenarios described in Section 5.2.4. It is notable that even though the single frequency results at 1 GHz were extremely poor, combining the 1 GHz data with 1.4 GHz data yields an image that is better than 1.4 GHz alone. Though beneficial, this fact makes choosing several frequencies for simultaneous inversion difficult, since even poor single frequency results can yield improvements when used with good single frequency data.

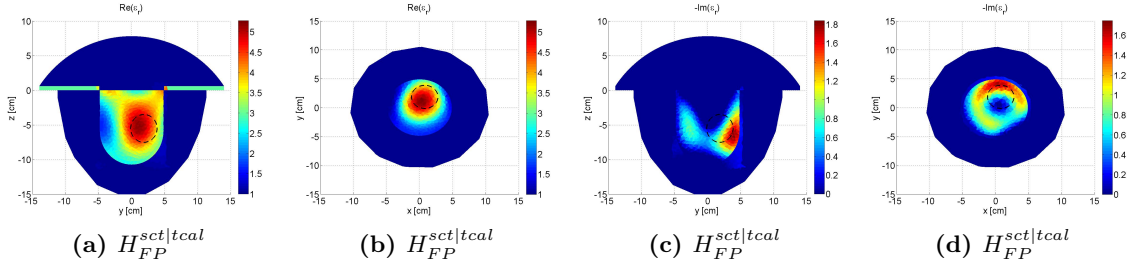


Figure 5.12: Simultaneous frequency inversion results for simple breast phantom at 1 GHz and 1.4 GHz. (a) and (b) show $Re(\epsilon_r)$ and (c) and (d) show $-Im(\epsilon_r)$.

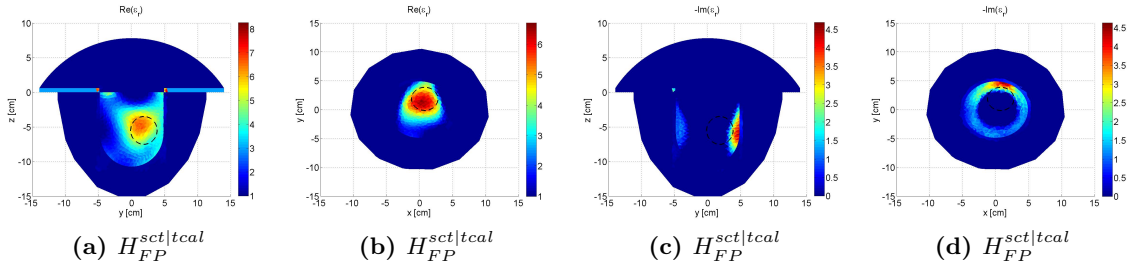


Figure 5.13: Simultaneous frequency inversion results for simple breast phantom at 1.3 GHz and 1.4 GHz. (a) and (b) show $Re(\epsilon_r)$ and (c) and (d) show $-Im(\epsilon_r)$.

The examination of multiple frequency inversions was ended here. There are many future possibilities for exploring the use of simultaneous frequency data, but these are beyond the scope of this work.

Chapter 6

Conclusions and Future Work

This thesis detailed the successful development, implementation, and testing of a novel MWI system for breast imaging, utilizing a faceted metallic chamber, an air background, and magnetic field data. In summary:

- A novel faceted chamber geometry was conceived in order to address current drawbacks in chamber design. Several synthetic studies were conducted to assess the performance of the novel design. It showed improvements over a cylindrical chamber in both modeling error and of reconstructing simple targets across a selected frequency band. Next, two different simple breast phantoms were imaged in the faceted chamber, and $\hat{\phi}$ polarized magnetic field data was shown to produce the best reconstructions.
- Magnetic field probes were designed and tested for use in an experimental breast imaging system. Several prototype designs were simulated and tested, and a grounded CPW PCB implementation of a shielded half-loop probe with a top gap was selected. This design was refined and made reconfigurable with the addition of passive circuitry and a shorting diode. The probe was tested in a GTEM cell to verify sensitivity to magnetic fields and rejection of electric fields.

- The novel faceted chamber geometry was constructed and assembled. The magnetic field probes were mounted in the chamber and very good incident field modeling was observed. Imaging trials were carried out with simple cylindrical targets in order to assess the behaviour under different probe loading conditions and with different data calibration techniques. Experimental images were obtained that compared favorably with synthetic equivalents with proper selection of loading condition and calibration technique.
- A simple breast phantom was placed in the novel chamber and data was collected, calibrated and inverted with the use prior information. The reconstructions clearly show that tumour detection inside the simple phantom is possible in an air background with this novel chamber.

6.1 Future Work

This thesis presents a first step toward imaging high contrast breast tissue targets in a metallic air based MWI chamber. There are many possibilities for future work based on this system, including:

- Imaging studies with more complicated multilayered breast phantoms with realistic tissue properties.
- Using a combination of magnetic field polarizations (*i.e.* H_ϕ and H_z) to determine if hybrid polarized data leads to improved reconstruction quality.
- Incorporating magnetic or electric field MST probes on the unused facets in order to acquire more data and take advantage of the benefits of the MST.
- Refine the magnetic field probe by removing the circuitry and possibly using alternate PCB substrates to reduce the thickness and trace size of the grounded CPW trans-

mission line. This would likely reduce field perturbation by the probes and therefore modeling error.

- Thoroughly examine inverting data at multiple frequencies.
- Construction of an experimental system to experimentally acquire prior information about an OI placed in the chamber. This would expand the possible targets that could be imaged using this system, and lay the groundwork for future clinical trials.

In addition to the work that can be done with the faceted chamber, several possibilities exist for improving the FEM-CSI algorithm, and therefore imaging results, including:

- Balancing the real and imaginary variables in order to improve the imaginary part of the reconstruction.
- Implement an inverse solver with higher order basis functions, which would increase accuracy and enable the modeling of more complicated MRI derived breast phantoms without adding unmanageable computational burden.
- Terminating CSI iterations with some criteria (*e.g.* percent change between iterations below some threshold) instead of a fixed iteration count.

Appendix A

Further Synthetic Analysis of Faceted Chamber

This appendix details further analysis of the faceted chamber that is tangential to the main thrust of this thesis. The first section of this appendix mirrors Section 2.2.3, but uses imperfect prior information. The second section examines the impact of using both H_ϕ and H_z data instead of a single H -field polarization.

A.1 Inversion Results for Two tumour Phantom with Imperfect Prior

This section contains preliminary analysis of the faceted chamber's performance when imperfect prior information is used in order to verify that tumour targets are still detectable. More detailed analysis of the impact of accuracy in prior information is conducted in [34], but is beyond the scope of this work.

The phantom used in this section is identical to the two tumour phantom introduced in Section 2.2.1. To reiterate, the fat/fibroglandular region was assigned a permittivity of

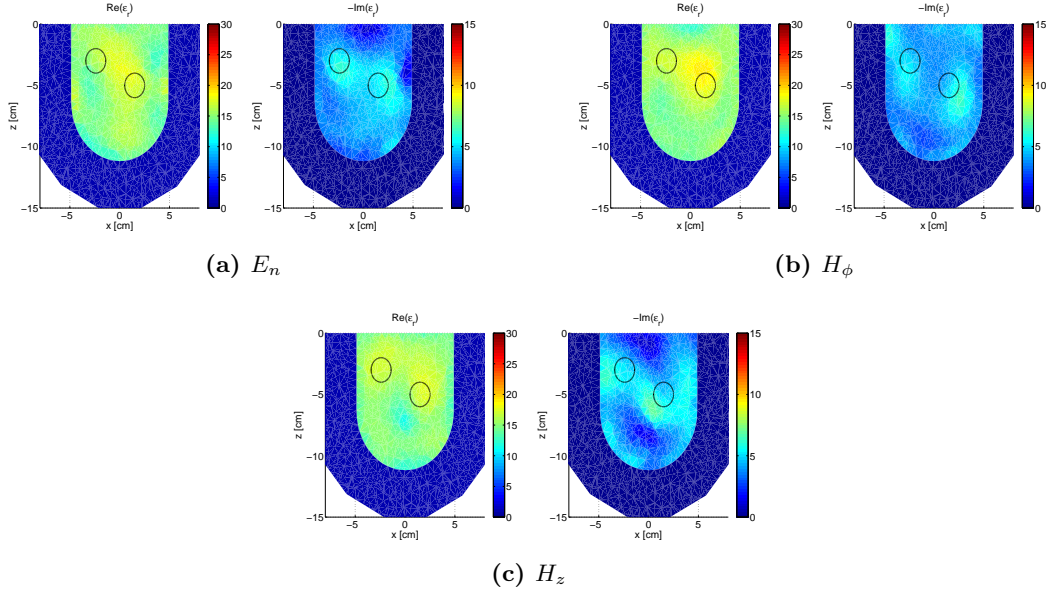


Figure A.1: Reconstructed ε_r at 0.9 GHz for a PEC chamber top.

$\varepsilon_{r-ft/fib} = 15.21 - j4.08$ which is between the permittivity of pure fat and pure fibroglandular tissue, and the tumours were assigned values of $\varepsilon_{r-t1} = 42 - j14$ and $\varepsilon_{r-t2} = 58 - j16$ [8]. However, this time, instead of using the true value of $\varepsilon_{r-ft/fib} = 15.21 - j4.08$ as prior information, the fat/fibroglandular region was assumed to be 25% undershot, having $\varepsilon_r = 12.168 - j3.264$.

As in Section 2.2.3, the collected forward data was inverted on a different mesh with 5% noise added to the data. This was done at fewer frequencies (0.9 GHz to 1.5 GHz, steps of 100 MHz), and only for the PEC top chamber model. Each inversion was terminated at 250 iterations, and the imaging domain was restricted to a cylinder slightly larger than the breast region (radius 5.375 cm and height 12.475 cm). Results for each polarization at 0.9 GHz, 1.2 GHz, and 1.5 GHz are shown in Figures A.1, A.2, and A.3 respectively. As can be seen, tumours are still visible, but the localization is poorer than the perfect prior case (compare to Figures 2.14 and 2.16).

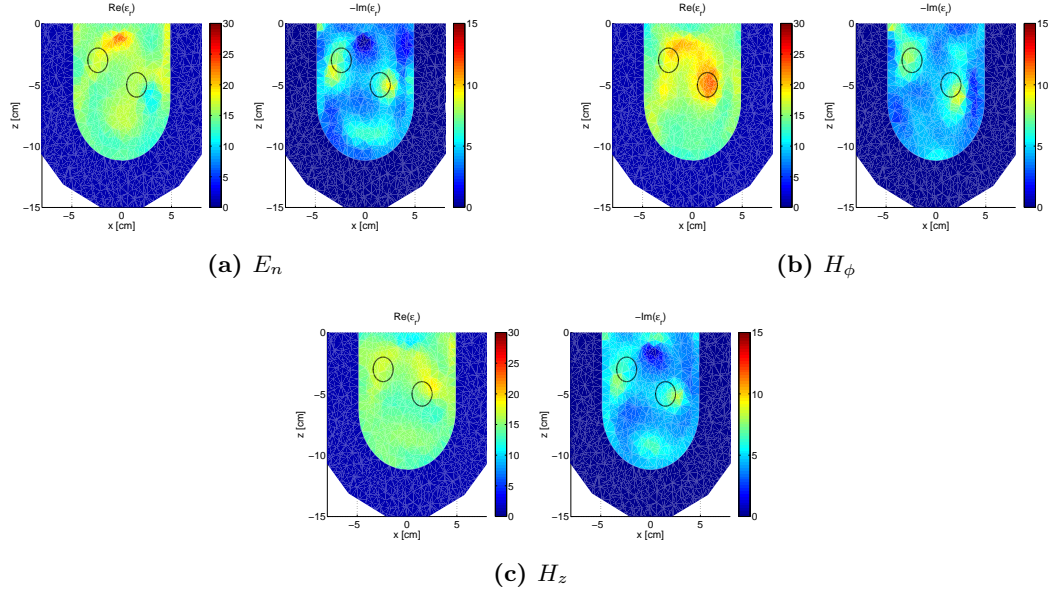


Figure A.2: Reconstructed ε_r at 1.2 GHz for a PEC chamber top.

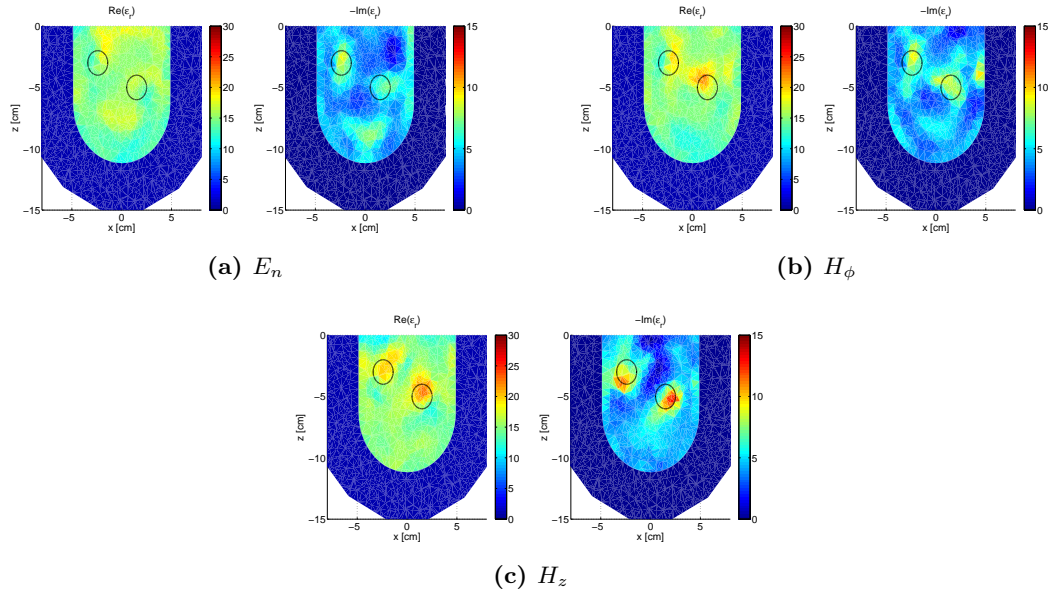


Figure A.3: Reconstructed ε_r at 1.5 GHz for a PEC chamber top.

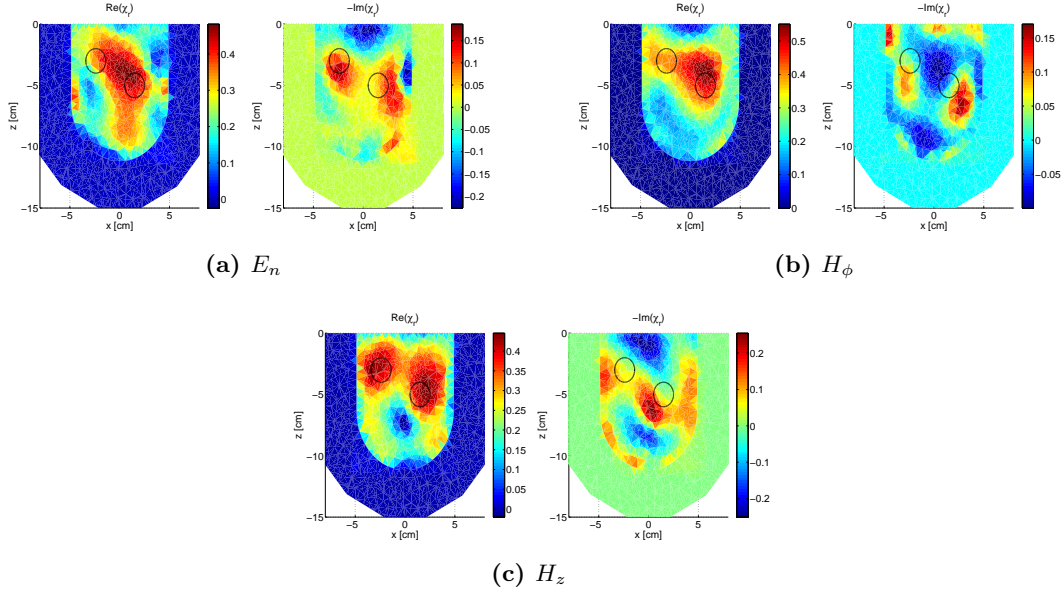


Figure A.4: Reconstructed χ at 0.9 GHz for a PEC chamber top.

As the prior information assumes a lower permittivity of the fat/fibroglandular region than the true value, it is also expected that increases in the permittivity of the fat/fibroglandular region will be visible in the reconstruction. This is difficult to see in the permittivity images due to the colour bar scale. Therefore, Figures A.4, A.5, and A.6 show the reconstructed contrast as opposed to the permittivity in Figures A.1, A.2, and A.3 respectively. From these results, it is clear that the contrast in the fat/fibroglandular region is greater than zero in many locations, indicating the algorithm’s sensitivity to the improper prior information. However, the increase in contrast is not uniform. This result is consistent with other results obtained in the EIL. The algorithm has trouble uniformly changing the contrast in a large homogeneous region. Furthermore, though this gives some sense of the impact of imperfect prior, human breasts do not have such uniform homogeneous regions and further analysis with anatomically realistic phantoms must be carried out.

The same reconstruction metrics detailed in Section 2.2.3 were applied to the imperfect

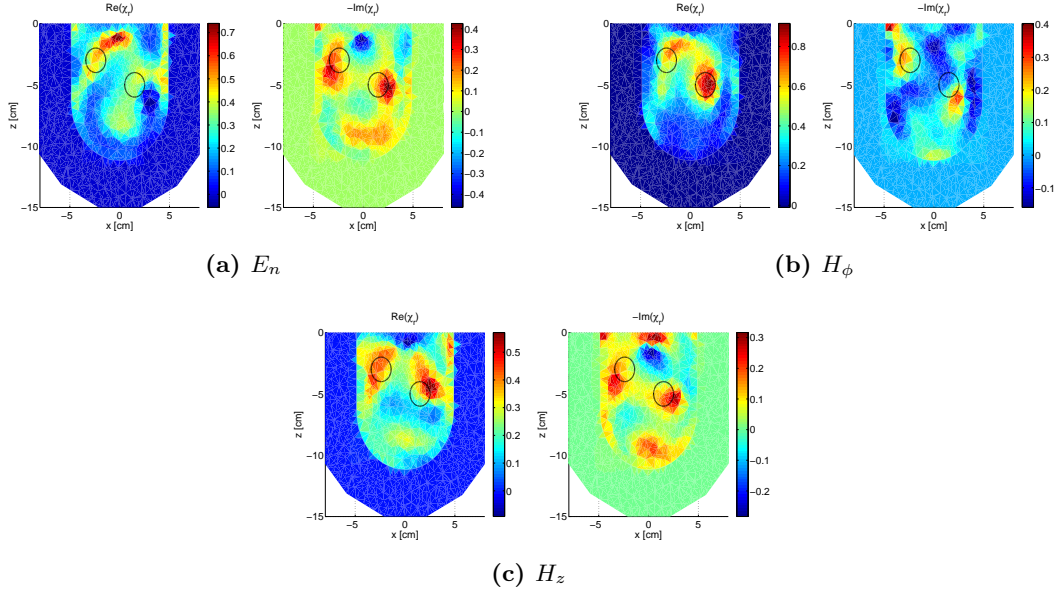


Figure A.5: Reconstructed χ at 1.2 GHz for a PEC chamber top.

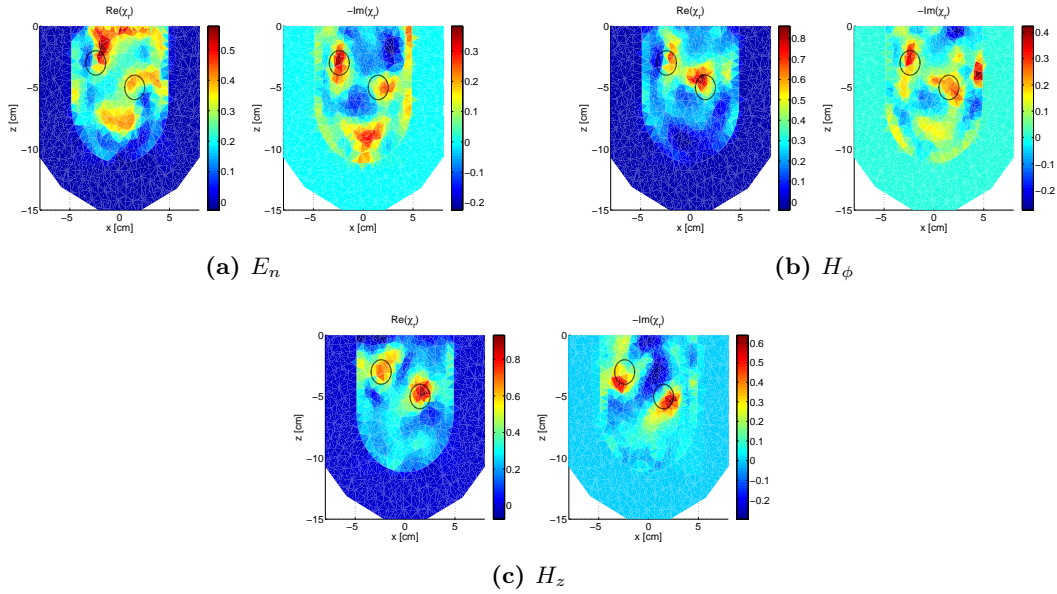


Figure A.6: Reconstructed χ at 1.5 GHz for a PEC chamber top.

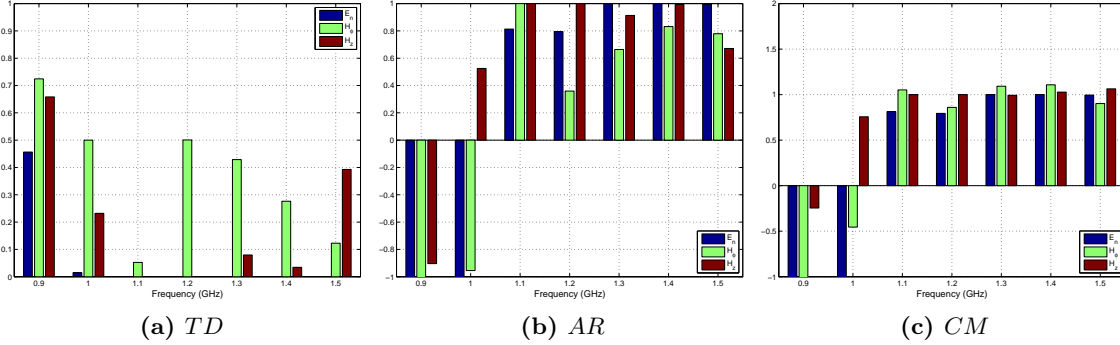


Figure A.7: Metrics for $Re(\varepsilon_r)$, PEC chamber top.

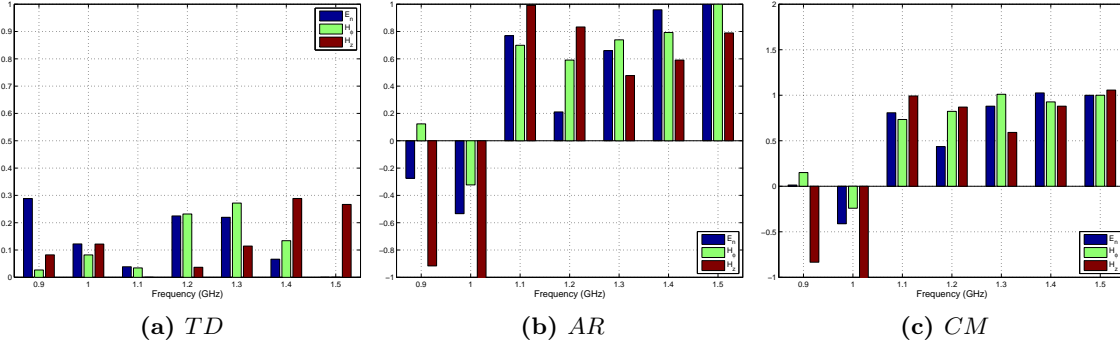


Figure A.8: Metrics for $Im(\varepsilon_r)$, PEC chamber top.

prior results and are shown in Figures A.7 and A.8. As before, the H_ϕ polarized data is superior for tumour detection in the real part. As expected, there is much more variation in the imperfect prior case with respect to artifact rejection (compare to Figures 2.19 and 2.20). Furthermore, it is hard to clearly distinguish between polarizations with the imaginary part metrics. However, based on the tumour detection in the real part and the eye test, H_ϕ is still considered to be the best choice for single polarized data in the faceted chamber.

A.2 Inversion Results for Two tumour Phantom with Dual Polarized H-Field Data

As stated, the work in Section 2.2 and A.1 focuses on comparing E_n , H_ϕ , and H_z polarized data. Single polarizations were compared since multi-polarized antennas did not exist in the EIL and designing such probes was beyond the scope of this work. Since the completion of that work, Dr. Mohammad Asefi in the EIL has developed preliminary designs for a magnetic field probe capable of switching between collecting H_ϕ and H_z field data. This section examines the impact of using both magnetic field polarizations as data on the reconstructions.

As before, the two tumour phantom is used in this study. 48 transceivers are used, 24 H_ϕ transceivers, and 24 co-located H_z transceivers. Again, the collected forward data was inverted on a different mesh with 5% noise added to the data. This was done at 0.9 GHz to 1.5 GHz in steps of 100 MHz, and only for the PEC top chamber model. Each inversion was terminated at 250 iterations, and the imaging domain was restricted to a cylinder slightly larger than the breast region (radius 5.375 cm and height 12.475 cm). As shown in Figure A.9, the dual polarized data yields very good results.

The metrics from [34] are also applied here, comparing each pure polarization with the dual polarized result. Figure A.10 and A.11 show the results for the real and imaginary parts respectively. The dual polarized results (termed H_{mix} in the figures) are clearly substantially superior to the single polarized counterparts in both real and imaginary tumour detection. Though it appears that the single polarized results are superior in artifact rejection, as in Section 2.2.3, the apparent excellent artifact rejection is due to the threshold exceeding all reconstructed values, and therefore no artifacts or tumours are detected. Therefore, it can be concluded that a system employing dual-polarized probes should feature improved reconstructions.

A.2 Inversion Results for Two tumour Phantom with Dual Polarized H-Field Data

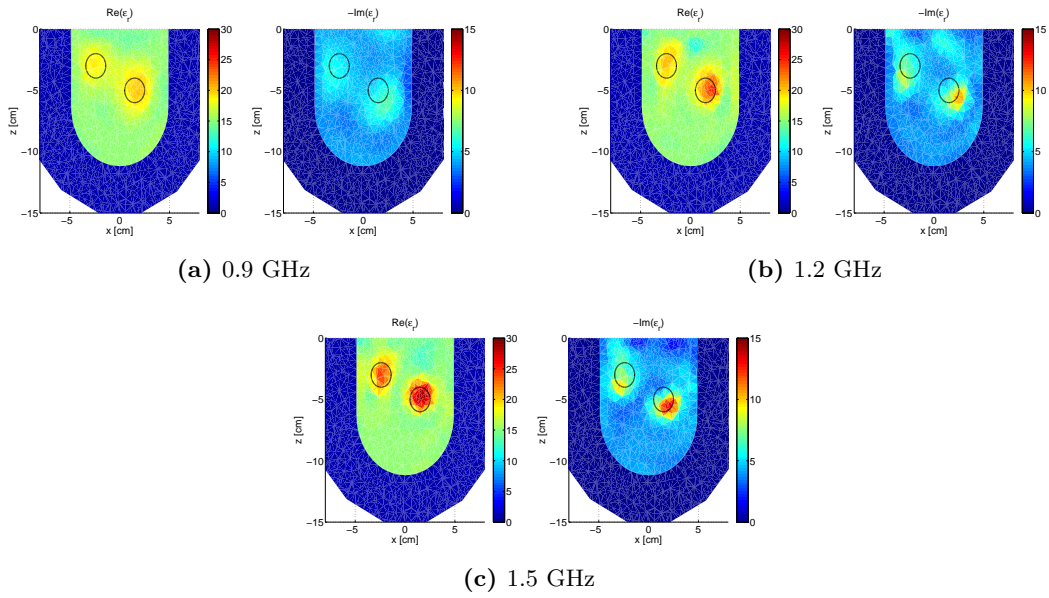


Figure A.9: Reconstructed ε_r for mixed H_ϕ and H_z and a PEC chamber top.

It is difficult to determine if these improvements are simply due to the increase in data given to the FEM-CSI algorithm, or if the fact that the added data incorporates a second polarization is a key factor. More analysis must be done to delineate these factors, and is left to future work.

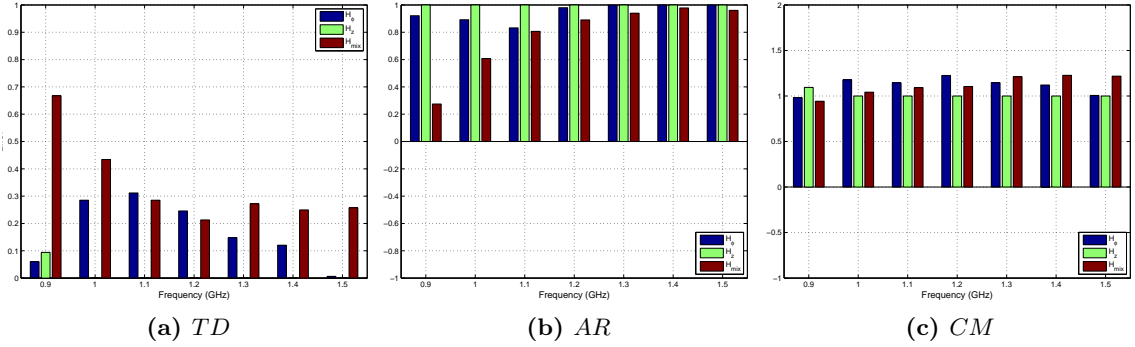


Figure A.10: Metrics for $Re(\epsilon_r)$, PEC chamber top.

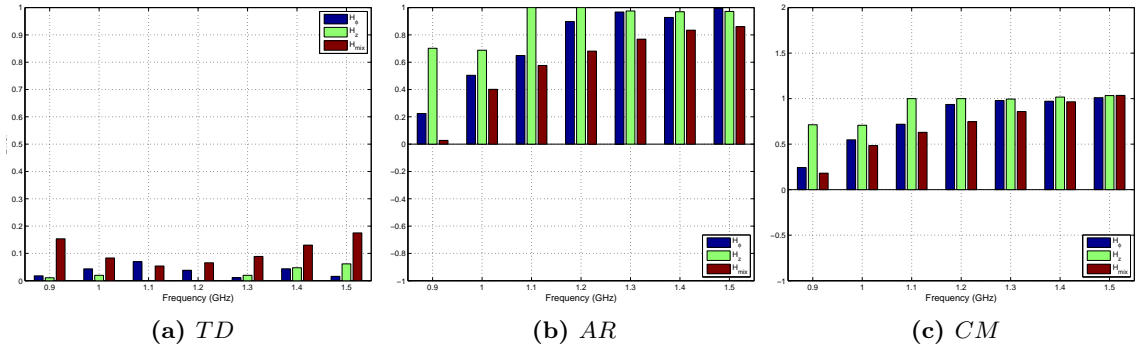


Figure A.11: Metrics for $Im(\epsilon_r)$, PEC chamber top.

References

- [1] N. K. Nikolova, "Microwave imaging for breast cancer," *IEEE Microwave Magazine*, vol. 12, no. 7, pp. 78–94, Dec 2011.
- [2] E. C. Fear, X. Li, S. C. Hagness, and M. A. Stuchly, "Confocal microwave imaging for breast cancer detection: localization of tumors in three dimensions," *IEEE Transactions on Biomedical Engineering*, vol. 49, no. 8, pp. 812–822, Aug 2002.
- [3] P. M. Meaney, F. W. Fanning, D. Li, S. P. Poplack, and K. D. Paulsen, "A clinical prototype for active microwave imaging of the breast," *IEEE Trans. Microw. Theory Techn.*, vol. 48, no. 11, pp. 1841–1853, Nov. 2000.
- [4] M. Persson, A. Fhager, H. D. Trefna, Y. Yu, T. McKelvey, G. Pegenius, J. E. Karlsson, and M. Elam, "Microwave-based stroke diagnosis making global prehospital thrombolytic treatment possible," *IEEE Transactions on Biomedical Engineering*, vol. 61, no. 11, pp. 2806–2817, November 2014.
- [5] D. Ireland, K. Bialkowski, and A. Abbosh, "Microwave imaging for brain stroke detection using born iterative method," *IET Microwaves, Antennas Propagation*, vol. 7, no. 11, pp. 909–915, August 2013.
- [6] S. Egot-Lemaire, J. Pijanka, J. Sule-Soso, and S. Semenov, "Dielectric spectroscopy of normal and malignant human lung cells at ultra-high frequencies," *Physics in medicine and biology*, vol. 54, no. 8, p. 2341, 2009.
- [7] J. D. Shea, P. Kosmas, S. C. Hagness, and B. D. V. Veen, "Three-dimensional microwave imaging of realistic numerical breast phantoms via a multiple-frequency inverse scattering technique," *Medical Physics*, vol. 37, p. 4210, 2010.
- [8] M. Lazebnik, D. Popovic, L. McCartney, C. B. Watkins, M. J. Lindstrom, J. Harter, S. Sewall, T. Ogilvie, A. Magliocco, T. M. Breslin *et al.*, "A large-scale study of the ultrawideband microwave dielectric properties of normal, benign and malignant breast tissues obtained from cancer surgeries," *Physics in Medicine and Biology*, vol. 52, no. 20, p. 6093, 2007.

-
- [9] A. Abubakar, T. Habashy, G. Pan, and M. Li, "Application of the multiplicative regularized gauss-newton algorithm for three-dimensional microwave imaging," *IEEE Transactions on Antennas and Propagation*, vol. 60, no. 5, pp. 2431–2441, May 2012.
- [10] P. M. van den Berg and R. E. Kleinman, "A contrast source inversion method," *Inverse Problems*, vol. 13, no. 6, p. 1607, 1997.
- [11] A. Zakaria, "The finite-element contrast source inversion method for microwave imaging applications," Ph.D. Thesis, University of Manitoba, 2012.
- [12] A. Zakaria, C. Gilmore, and J. LoVetri, "Finite-element contrast source inversion method for microwave imaging," *Inverse Problems*, vol. 26, no. 11, p. 115010, 2010.
- [13] A. Zakaria, I. Jeffrey, and J. LoVetri, "Full-vectorial parallel finite-element contrast source inversion method," *Progress In Electromagnetics Research*, vol. 142, pp. 463–483, 2013.
- [14] C. Geuzaine and J.-F. Remacle, "Gmsh: A 3-d finite element mesh generator with built-in pre- and post-processing facilities," *International Journal for Numerical Methods in Engineering*, vol. 79, p. 13091331, 2009.
- [15] A. Zakaria and J. LoVetri, *IEEE Transactions on Antennas and Propagation*, vol. 59, no. 9, pp. 3495–3498, September 2011.
- [16] M. Asefi, G. Faucher, and J. LoVetri, "Surface-current measurements as data for electromagnetic imaging within metallic enclosures," *IEEE Trans. Microw. Theory Techn.*, vol. PP, no. 99, pp. 1–9, 2016.
- [17] A. Zakaria, "The finite-element contrast source inversion method for microwave imaging applications," Ph.D. Thesis, University of Manitoba, 2012.
- [18] C. Gilmore, A. Zakaria, S. Pistorius, and J. LoVetri, "Microwave imaging of human forearms: pilot study and image enhancement," *Journal of Biomedical Imaging*, vol. 2013, p. 19, 2013.
- [19] A. Baran, A. Z. D. J. Kurrant, E. C. Fear, and J. LoVetri, "Breast imaging using microwave tomography with radar-based tissue-regions estimation," *Progress In Electromagnetics Research*, vol. 149, pp. 161–171, 2014.
- [20] D. Kurrant and E. Fear, "Defining regions of interest for microwave imaging using near-field reflection data," *IEEE Transactions on Microwave Theory and Techniques*, vol. 61, no. 5, pp. 2137–2145, May 2013.
- [21] A. Baran, "Microwave breast imaging techniques in two and three dimensions," Ph.D. Thesis, University of Manitoba, 2016.
-

-
- [22] A. Santorelli, E. Porter, E. Kang, T. Piske, M. Popovic, and J. D. Schwartz, "A time-domain microwave system for breast cancer detection using a flexible circuit board," *IEEE Transactions on Instrumentation and Measurement*, vol. 64, no. 11, pp. 2986–2994, November 2015.
- [23] M. Ostadrahimi, A. Zakaria, J. LoVetri, and L. Shafai, "A near-field dual polarized (te-tm) microwave imaging system," *IEEE Transactions on Microwave Theory and Techniques*, vol. 61, no. 3, pp. 1376–1384, March 2013.
- [24] M. J. Burfeindt, N. Behdad, B. D. Van Veen, and S. C. Hagness, "Quantitative microwave imaging of realistic numerical breast phantoms using an enclosed array of multiband, minituarized patch antennas," *IEEE Ant. Wireless Propag. Lett.*, vol. 11, pp. 1626–1629, 2012.
- [25] P. M. Meaney, M. W. Fanning, T. Raynolds, C. J. Fox, Q. Fang, C. A. Kogel, S. P. Poplack, and K. D. Paulsen, "Initial clinical experience with microwave breast imaging in women with normal mammography," *Academic Radiology*, vol. 14, no. 2, pp. 207–218, 2007.
- [26] E. C. Fear, J. Bourqui, C. Curtis, D. Mew, B. Docktor, and C. Romano, "Microwave breast imaging with a monostatic radar-based system: A study of application to patients," *IEEE Transactions on Microwave Theory and Techniques*, vol. 61, no. 5, pp. 2119–2128, May 2013.
- [27] M. Ostadrahimi, P. Mojabi, A. Zakaria, J. LoVetri, and L. Shafai, "Enhancement of gauss newton inversion method for biological tissue imaging," *IEEE Transactions on Microwave Theory and Techniques*, vol. 61, no. 9, pp. 3424–3434, Sept 2013.
- [28] M. Asefi, M. Ostadrahimi, A. Zakaria, and J. LoVetri, "A 3-d dual-polarized near-field microwave imaging system," *IEEE Transactions on Microwave Theory and Techniques*, vol. 62, no. 8, pp. 1790–1797, August 2014.
- [29] B. J. Mohammed, A. M. Abbosh, S. Mustafa, and D. Ireland, "Microwave system for head imaging," *IEEE Transactions on Instrumentation and Measurement*, vol. 63, no. 1, pp. 117–123, Jan 2014.
- [30] E. Porter, H. Bahrami, A. Santorelli, B. Gosselin, L. A. Rusch, and M. Popovi, "A wearable microwave antenna array for time-domain breast tumor screening," *IEEE Transactions on Medical Imaging*, vol. 35, no. 6, pp. 1501–1509, June 2016.
- [31] M. Asefi, "Stored-grain monitoring utilizing radio wave imaging," Ph.D. Thesis, University of Manitoba, 2016.
- [32] M. Asefi, A. Zakaria, and J. LoVetri, "Microwave imaging using normal electric field components inside metallic resonant chambers," *IEEE Transactions on Microwave Theory and Techniques*, (submitted).
-

-
- [33] M. Ostadrahimi, A. Baran, M. Asefi, C. Kaye, K. Nemez, J. LoVetri, and S. Pistorius, "On the development of a clinical full-vectorial 3d microwave breast imaging system," in *Radio Science Meeting (Joint with AP-S Symposium), 2015 USNC-URSI*, July 2015, pp. 300–300.
- [34] D. Kurrant, A. Baran, J. LoVetri, and E. Fear, "Impact of errors in prior information on microwave tomography image quality," *Inverse Problems*, (submitted).
- [35] A. Wirgin, "The inverse crime," *Arxiv preprint math-ph/0401050*, 2004.
- [36] A. Sabouni and A. A. Kishk, "Dual-polarized, broadside, thin dielectric resonator antenna for microwave imaging," *IEEE Antennas and Wireless Propagation Letters*, vol. 12, pp. 380–383, 2013.
- [37] S. Rashid, Y. Wu, X. Wang, Y. Wang, and Y. Ding, "Design of a corrugated tapered slot antenna for microwave imaging," in *2016 IEEE International Conference on Computational Electromagnetics (ICCEM)*, Feb 2016, pp. 356–357.
- [38] N. Ojaroudi, M. Ojaroudi, and N. Ghadimi, "Uwb omnidirectional square monopole antenna for use in circular cylindrical microwave imaging systems," *IEEE Antennas and Wireless Propagation Letters*, vol. 11, pp. 1350–1353, 2012.
- [39] C. A. Balanis, *Antenna Theory: Analysis and Design 3rd Edition*. Hoboken, NJ: Wiley, 2005.
- [40] A. F. Sheta, I. Elshafiey, A. Mohra, Z. Siddiqui, and A. R. Sebak, "A compact antenna for microwave imaging and hyperthermia treatment of brain tumor," in *Antenna Technology and Applied Electromagnetics (ANTEM), 2012 15th International Symposium on*. IEEE, 2012, pp. 1–4.
- [41] M. Ostadrahimi, P. Mojabi, S. Noghianian, L. Shafai, S. Pistorius, and J. LoVetri, "A novel microwave tomography system based on the scattering probe technique," *IEEE Transactions on Instrumentation and Measurement*, vol. 61, no. 2, pp. 379–390, February 2012.
- [42] M. Kanda, "Standard probes for electromagnetic field measurements," *IEEE Transactions on Antennas and Propagations*, vol. 41, no. 10, pp. 1349–1364, October 1993.
- [43] R. F. Harrington, *Time-Harmonic Electromagnetic Fields*. Piscataway, NJ: IEEE Press, 2001.
- [44] R. J. Spiegel, C. A. Booth, and B. E. L., "A radiation measuring system with potential automotive under-hood application," *IEEE Transactions on Electromagnetic Compatibility*, vol. EMC-25, no. 2, pp. 61–69, May 1983.
- [45] G. S. Smith, "Loop antennas," *Antenna Engineering Handbook*, pp. 5–20, 1984.

-
- [46] “Microstrip impedance calculator,” visited on Oct. 19, 2016. [Online]. Available: <https://www.eeweb.com/toolbox/microstrip-impedance/>
- [47] “Symmetric stripline impedance,” visited on Oct. 19, 2016. [Online]. Available: <https://www.eeweb.com/toolbox/symmetric-stripline-impedance/>
- [48] “Coplanar waveguide calculator,” visited on Oct. 19, 2016. [Online]. Available: <https://www.microwaves101.com/encyclopedias/coplanar-waveguide-calculator>
- [49] “Coplanar waveguide with ground characteristic impedance calculator,” visited on Oct. 19, 2016. [Online]. Available: <http://chemandy.com/calculators/coplanar-waveguide-with-ground-calculator.htm>
- [50] M. OstadRahimi, K. Nemez, A. Zakaria, J. LoVetri, L. Shafai, and S. Pistorius, “A novel microwave tomography system for breast imaging based on the modulated scattering technique,” in *Radio Science Meeting (Joint with AP-S Symposium), 2014 USNC-URSI*, July 2014, pp. 54–54.
- [51] D. M. Pozar, *Microwave Engineering*. Hoboken, NJ: Wiley, 2012.
- [52] A. Zakaria, A. Baran, and J. LoVetri, “Estimation and use of prior information in femcsi for biomedical microwave tomography,” *IEEE Antennas and Wireless Propagation Letters*, vol. 11, pp. 1606–1609, 2012.
- [53] M. Ostadrahimi, P. Mojabi, C. Gilmore, A. Zakaria, S. Noghianian, S. Pistorius, and J. LoVetri, “Analysis of incident field modeling and incident/scattered field calibration techniques in microwave tomography,” *IEEE Antennas and Wireless Propagation Letters*, vol. 10, pp. 900–903, 2011.
- [54] J. Bolomey and F. Gariol, *Engineering Applications of the Modulated Scatterer Technique*. Norwood, MA: Artech House, 2001.